DESIGN AND IMPLEMENTATION OF SENSOR FUSION FOR THE TOWED SYNTHETIC APERTURE SONAR

Rui Daniel Meng

A thesis submitted in partial fulfilment
of the requirements for the degree of
Master of Engineering
in
Electrical and Computer Engineering
at the
University of Canterbury,
Christchurch, New Zealand.

December 2006

ABSTRACT

For synthetic aperture imaging, position and orientation deviation is of great concern. Unknown motions of a Synthetic Aperture Sonar (SAS) can blur the reconstructed images and degrade image quality considerably. Considering the high sensitivity of synthetic aperture imaging technique to sonar deviation, this research aims at providing a thorough navigation solution for a free-towed synthetic aperture sonar (SAS) comprising aspects from the design and construction of the navigation card through to data postprocessing to produce position, velocity, and attitude information of the sonar.

The sensor configuration of the designed navigation card is low-cost Micro-Electro-Mechanical-Systems (MEMS) Magnetic, Angular Rate, and Gravity (MARG) sensors including three angular rate gyroscopes, three dual-axial accelerometers, and a triaxial magnetic hybrid. These MARG sensors are mounted orthogonally on a standard 180 mm Eurocard PCB to monitor the motions of the sonar in six degrees of freedom. Sensor calibration algorithms are presented for each individual sensor according to its characteristics to precisely determine sensor parameters. The nonlinear least square method and two-step estimator are particularly used for the calibration of accelerometers and magnetometers.

A quaternion-based extended Kalman filter is developed based on a total state space model to fuse the calibrated navigation data. In the model, the frame trans-

formations are described using quaternions instead of other attitude representations. The simulations and experimental results are demonstrated in this thesis to verify the capability of the sensor fusion strategy.

ACKNOWLEDGMENTS

I would like to give my sincerest thanks to my supervisor, Dr Michael Hayes, for his patience and tolerance in guiding me in scientific research, his greatest help and encouragement, and his assistance in writing up. From his supervision, I have been well benefited in many aspects including the method and attitude of scientific research and invaluable life lessons in adopting a new culture from totally different background.

Many thank you to Mike Cusdin for his assistance in PCB drawing and contacting manufacturers and distributors. You are the important person behind everything. Without you, the navigation card could have not been in my hands on time. Also, I greatly appreciate the help from Edward Pilbrow, Alan Hunter, and Mark Noonchester in research, writing, and so much more. I also like to express my appreciation to Prof Peter Gough for his help in correcting my thesis.

Finally, appreciation to my family, the people I love the most. Your support and encouragement have always driven me through the years of study overseas, and your love and sacrifice are the eternal treasure and debt I own. I always feel inadequate for all these you have given to me, which motivate me to be a better son, husband and father in my everyday life.

TABLE OF CONTENTS

LIST OF FIGURES

LIST OF TABLES

LIST OF SYMBOLS

$\mathbf{i}$, $\mathbf{j}$, $\mathbf{k}$	Unit vectors in a Cartesian coordinate system
$\mathbf{q}$	Quaternion
$\mathbf{R}_{b2a}$	Transformation matrix from reference frame b to a
$\mathbf{C}_{b2a}$	Initial alignment transformation matrix from reference frame b to a
$\boldsymbol{\omega}_{ba}^{a}$	Angular rate vector of frame a relative to frame b in the coordinate system of frame a
$\boldsymbol{\Omega}$	The skew-symmetric form of the angular rate vector
ω_x, ω_y, ω_z	Angular rates of x, y, and z axis in the body frame [rad/s]
θ_x, θ_y, θ_z	Euler angles of x, y, and z axis in the body frame with respect to the tangent plane [rad]
θ_{dec}	The Earth's magnetic field declination angle
θ_{inc}	The Earth's magnetic field inclination angle
Ψ	Quaternion derivative matrix
V	Sensor's voltage output
$\mathbf{s}$, $\mathbf{b}$	Sensor's scale factor and bias vectors

τ	Correlation time constant
$\mathbf{P}$	Nonorthogonal correction matrix for correcting the nonorthogonal realistic sensor frame into an orthogonal sensor frame.
$\mathbf{T}$	Direction cosine matrix for transformations from the body frame to the orthogonal sensor frame
$\mathbf{B}$	Magnetic field intensity vector
$\mathbf{B}_e$	The Earth's magnetic field intensity vector
$\mathbf{a}_{\text{acc}}$	Total acceleration caused by the force impacting on an accelerometer triad
$\mathbf{a}^b$	The acceleration vector measured by the accelerometers in the body frame
g	The Earth's positive gravitational constant
$\mathbf{v}^b$	The velocity vector with reference to the body frame
$\mathbf{r}^t$	The position vector with reference to the tangent plane
$\mathbf{A}$, $\mathbf{H}$	Jacobian matrices of the process and measurement model of the Kalman filter
$\mathbf{P}_0$	Initial state error covariance matrix
$\mathbf{Q}$	Process noise covariance matrix
$\mathbf{R}$	Measurement noise covariance matrix

CHAPTER 1

INTRODUCTION

1.1 Overview

The Acoustics Research Group at the University of Canterbury has designed and built a Synthetic Aperture Sonar (SAS) for high resolution underwater imagery. The towfish is nose towed and slightly positively buoyant [1]. A towboat pulls the towfish through a tow cable. A chain is attached to the tow cable to depress the towfish. However, the towfish's movement of rotation and drift is not constrained, and it has six degrees of freedom. Since SAS has high sensitivity to the position and orientation deviation, the unknown motion is a great concern for aperture synthesis imaging [2]. The basic operational principle of a SAS is the determination of the time delay between the transmission of a ping signal and subsequent detection of the echoes from a target [1]. Unknown towfish motion varies the detected time delay and consequently degrades the process image quality. However, if the towfish motion could be monitored, the blurring caused by the position and orientation deviation could be eliminated by postprocessing the signal data before image reconstruction [2].

For position and orientation tracking of the towfish, an integrated dead-reckoning navigation system is desirable. Dead reckoning navigation is a process of estimating position by advancing a known position using time, speed, and heading measurements. An Inertial Navigation System (INS) is a dead reckoning technique which obtains position estimation by double integrating the signal from accelerometers and orientation determined by integration of the angular rates of gyros. This navigation technology has become more popular because the new developed Micro-Electro-Magnetic-Systems (MEMS) inertial sensors provide significantly decreasing cost and size as well as improved performance.

Meanwhile, other sensors such as inclinometers and magnetometers can also be used for underwater navigation. An inclinometer is a device for measuring the angles of elevation and inclination of an object with respect to the Earth's gravity, and a magnetometer is a device for measuring the angle of yaw relative to the Earth's magnetic field. Furthermore, there are various speed sensors available for measuring the velocity, such as flow sensors, which are designed for sensing the rate of fluid flowing through them, and Doppler Velocity Logs (DVL), which adopt Doppler effects to measure vehicle speed over ground. Position information obtained from Global Positioning Systems (GPS) can also be applied to underwater navigation for position fixing purposes when the underwater vehicles periodically swim to the surface [3].

Different types of sensors are designed according to different physical principles, which lead to characteristic strength and weakness. Ideally, the strength of one type of sensors should be able to cope with the weakness of another type of sensors through proper selection, and thus sensor data sources can be combined to produce more accurate information. The hybridization of sensors is known as sensor fusion. The Kalman filter is one of the commonly used sensor fusion technologies. The linear Kalman filter is an optimal observer that estimates the states of a linear dynamic system from noise-corrupted sensor measurements [4]. There are some variations of the linear Kalman filter, which can be used for state estimation of a nonlinear dynamic system, such as the extended Kalman filter. The Kalman filter is often used to estimate position, velocity, and orientation states from multi-sensor measurements [5, 6, 7].

A previous work on the construction of the navigation card was reported in [8].

The old navigation card contains a 3DM module, which uses three accelerometers and three magnetometers to provide orientation estimation, and a dual-axis fluid inclinometer to obtain the angles of pitch and roll. An absolute pressure sensor as well as a leakage sensor were also installed for monitoring the depth of the towfish and detecting the leakage status. The accelerometers in 3DM was utilized to measure the translational motion of the towfish by double integration of the acceleration measurements. Based on the navigation data of this INS, the effects of towfish pitch and roll were able to be substantially reduced [8]. However, the correction for yaw and translational movements gave less satisfactory results [8]. Unfortunately, this card was damaged by an accident.

1.2 Thesis Objective

The objective of this thesis is to develop a thorough navigation solution for monitoring the unknown movements of the towfish with emphasis on orientation prediction using off-the-shelf and low-cost sensor clusters. The complete solution needs to cover sensor calibration, sensor fusion, as well as Position, Velocity, and Attitude (PVA) estimation algorithm to provide a study reference and navigation design infrastructure for further expansion.

Low-cost Magnetic, Angular Rate, and Gravity (MARG) sensors were chosen to provide data sources for the new navigation card. Sensor configuration, hardware construction and software architecture are given in detail in this thesis. The motivation of the sensor hybridization is to combine the complementary aspects of each sensor. The angular velocities obtained from rate gyroscopes are contaminated by errors. Through integration, the resulting orientation estimates drift because of fluctuations of the gyroscope offset and measurement noise. In contrast, gravity and magnetic sensors provide drift-free measurement of orientation with reference to the Earth's gravity and magnetic field [9]. Therefore, orientation estimates with higher accuracy are expected to be achieved through the sensor fusion of MARG sensors.

In practice, all sensors are prone to errors. A few common errors exist such as bias and scale factor uncertainty. Manufacturing and assembly errors also result in axis misalignment. For the rate gyroscopes, temperature variation can cause

output drift correlated with time. Magnetic disturbances corrupt the measurements of the magnetometers. These errors are of great concern. In order to obtain correct navigation information, initial sensor calibration is essential. Part of this thesis also focus on providing efficient and accurate calibration methods for sensors without the aid of specialized equipment.

A sensor fusion algorithm is required to hybridize these calibrated navigation data. The Kalman filter has been widely used in the area of autonomous or assisted navigation [10], which can be involved in the post processing to provide an optimal filter for optimizing the whole sensing system performance. With the focus on orientation estimation, a quaternion-based extended Kalman filter is studied. Since the accelerometers measure absolute acceleration including translational acceleration and gravitational acceleration. The gravity sensing ability of the accelerometers is manipulated to provide orientation information. The orientation estimates from the sensor fusion is used to decouple translational acceleration from the total acceleration measurements, and consequently velocity and position can be estimated through the first and double integration of the translational acceleration. The satisfaction of the strategy is thoroughly tested and discussed in this thesis.

1.3 Thesis Outline

Chapter 2 gives a background review of the thesis and introduces some general concepts used in the towfish navigation. First, the fundamentals of the towfish design and mechanism are described. A few commonly used frames of reference are introduced in order to provide background for the towfish motion description. For coordinate transformation between the frames of reference, a variety of attitude parameterization methods, including direction cosine matrix, Euler angles, and quaternions, are given in detail. In this chapter, a brief review of the Kalman filter is also provided to give perspective on the extended Kalman filtering technique implemented in Chapter 5.

Chapter 3 unveils the details of the navigation card in term of hardware and software design. The integrated MARG sensors are of the essence among the design and introduced firstly. In order to convert these valuable analog navigation data

in requirement of this work, associated electronics are required. The functionality of the associated electronics includes sensor control, data acquisition, and data communication. Embedded software programming configuration is also covered in this chapter.

Because considerable errors contaminate the outputs of these low-cost navigation sensors, initial calibration is of the importance of higher accuracy of the sensors. Chapter 4 presents the calibration procedures and techniques. For each individual sensor, the calibration focus is on scale factor, bias, and misalignment. The bias can be determined first and calibrated simply using static measurements or on-board electronic control interface, such as the set/reset circuit interfacing with the magnetometers. For scale factor and misalignment errors of the accelerometers and magnetometers, a nonlinear least squares routine is adopted. An algorithm called the two-step estimator is implemented specifically for the magnetic disturbance compensation of the magnetometers and is also discussed in this chapter.

In Chapter 5, a quaternion-based extended Kalman filter is derived. It is a total state space model that has position, velocity, and attitude vectors as well as the gyro bias vector as the state variables. The total state estimation starts with initial alignment process to determine the initial values of each state. The initial alignment is categorized into stationary alignment and in-motion alignment, which deal with the initial value determination process while the towfish is stationary and in-motion. A quaternion is implemented for parameterizing the orientation and rotation transformation within the filter. The accelerometers and magnetometers are used to correct for the effective orientation estimation based on the rate gyroscopes. The simulations and experimental results are also demonstrated.

CHAPTER 2

NAVIGATION SYSTEM FUNDAMENTALS

In order to design and implement a navigation system, some navigation system fundamentals are provided in this chapter. Firstly, the navigation-related basics of the towfish are introduced. Then, various frames of reference that are commonly used in navigation system applications are presented in Section 2.2. The motion of the towfish is included in the following section according to the frames of reference defined previously. In Section 2.4, the transformation of quantities between the various frames of reference is described. Details of the linear and extended Kalman filters are given in the last section of this chapter.

2.1 Towfish Introduction

The KiwiSAS IV towfish is a 1.7 m long PVC tube containing two pressure housings. The front pressure housing, named the transmitter can, contains the embedded computer and power amplifiers with projector arrays attached to its rear end

cap; the rear pressure housing, named the receiver can, contains preamplifiers and navigation sensors with hydrophone arrays interfaced to it. Before the sonar is submerged in the water, vacuums are created in both the transmitter and receiver cans. Pressure and leakage sensors in both cans monitor the vacuum status and detect water leaks. Also, a temperature-compensated absolute pressure sensor is installed in the receiver can and connected externally through a tapped hole for measuring the depth of the towfish.

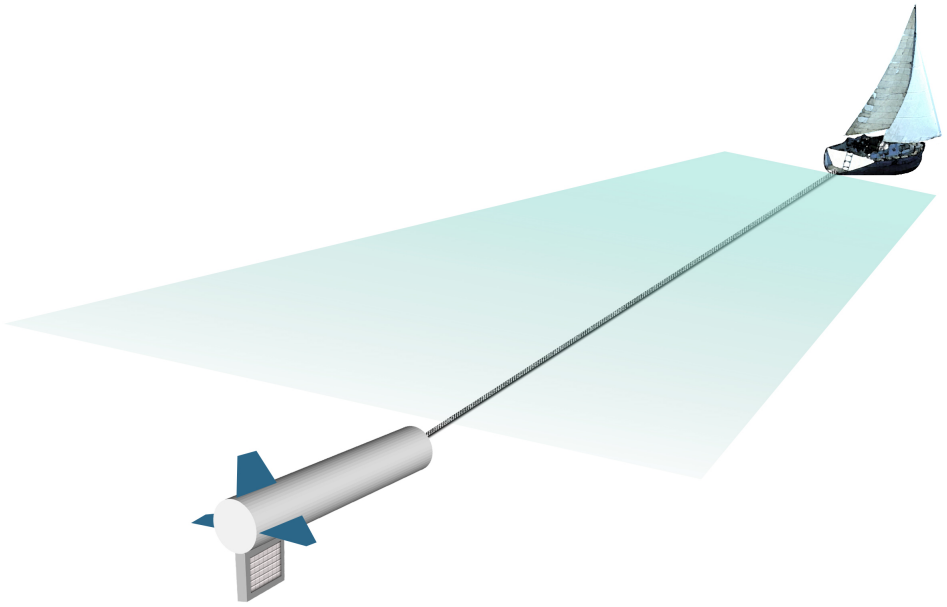

Figure 2.1. Illustration of the boat and the towed sonar.

The sonar is towed from its blunt nose and connected via a tow cable to the towboat interface. An illustration is shown in Figure 2.1. The tow cable provides an Ethernet connection between the towfish and towboat computers and power supply for the towfish. Because the towfish is slightly positively buoyant, a chain is attached to the cable via galvanic releases. In case of a problem, the galvanic releases corrode allowing the sonar to float to the surface. The operating depth of the towfish depends on the length of cable and the tow speed.

2.2 Frames of Reference

Many navigation systems are designed to fulfill accurate navigation over trajectories, especially for military purposes and long distance tracking applications. However, not every quantity in a navigation system is referenced to the Earth's geoid. For instance, the measurements of inertial sensors are relative to the inertial frame of reference. In this section, various frames of reference that are commonly used in navigation applications are introduced.

2.2.1 The Inertial Frame (i-frame)

The coordinate system in which Newton's first and second laws of motion are valid is called an inertial frame. In practice, one can often effectively assume that an inertial frame of reference is one at rest with respect to the Earth [11]. This frame can be called the pseudo-inertial frame. It has its origin at the centre of the Earth. The x axis points toward the vernal equinox, the z axis extends through the true north pole, and the y axis points to the east in the equatorial plane. The measurements of inertial sensors are relative to the inertial reference frame but resolved along the individual instrument-sensitive axis.

2.2.2 The Earth Frame (e-frame)

The Earth frame is a Cartesian reference system that follows the rotation of the Earth. There are two commonly used coordinate systems for the Earth frame, the rectangular coordinate system and the geodetic coordinate system [12].

The rectangular coordinate system, also named the Earth Centred Earth Fixed (ECEF) coordinate system, has its origin fixed to the centre of the Earth. Different to the pseudo-inertial frame, the x axis of the ECEF frame points towards the intersection of the Greenwich meridian with the equator [12]. The z axis is still along the Earth's spin axis, and the y axis is changed correspondingly to complete a right-handed orthogonal frame.

The other coordinate system is called the geodetic coordinate expressed in terms of the geodetic latitude, longitude, and altitude. The world geodetic system 1984 (WGS-84) ellipsoid parameters can be used for the transformation between

these two coordinate systems [12].

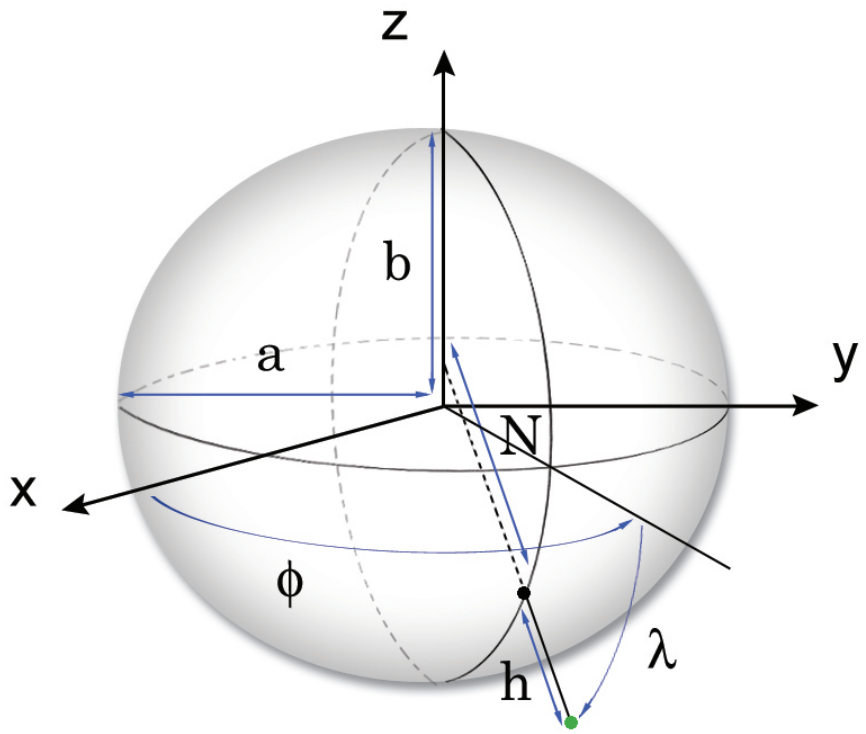

Figure 2.2. The Earth frame coordinate systems.

In Figure 2.2, both coordinate systems of the Earth frame are illustrated. According to the WGS-84, the Earth geoid is expressed as an ellipsoid with major axis length a and minor axis length b [12]

$$\begin{aligned} a &= 6378137.0\,\mathrm{m} \\ b &= 6356752.3142\,\mathrm{m} \end{aligned}$$

The flatness and eccentricity of the ellipsoid can be calculated as [12]

$$f = \frac{a-b}{a} = 0.0034 \tag{2.1}$$

and

$$e = \sqrt{f(2-f)} = 0.0818 \tag{2.2}$$

The length of the orthogonal line from the Earth surface to the intersection with the z axis of the rectangular coordinate is [12]

$$N(\lambda) = \frac{a}{\sqrt{1 - e^2 \sin(\lambda)^2}} \tag{2.3}$$

Altitude h is determined by the distance between the point of interest and the intersection between the Earth surface and the orthogonal line. Latitude λ is the angle between the orthogonal line and the Earth equatorial plane, and longitude ϕ is the angle between the prime meridian and the plane containing both the z axis and the point of interest. By using the three parameters in the geodetic coordinate, the point of interest can be expressed as

$$x = (N + h)\cos(\lambda)\cos(\phi) \tag{2.4}$$

$$y = (N + h)\cos(\lambda)\sin(\phi) \tag{2.5}$$

$$z = (N(1 - e^2) + h)\sin(\lambda) \tag{2.6}$$

2.2.3 The Tangent Plane (t-frame)

The tangent (local level) plane is also called the local geodetic frame, since it is defined locally relative to the geodetic reference ellipsoid [12]. The origin of the tangent plane may be arbitrarily chosen at a point of interest for local measurements. For the convenience of this application, the x axis heads towards the east and the y axis points to the true north. The z axis points up perpendicular to the Earth's reference ellipsoid to complete the right-handed coordinate system. The tangent plane is often used for local navigation [12].

2.2.4 The Body Frame (b-frame)

In order to describe the motion of the body of interest, the body frame is defined as a Cartesian coordinate system rigidly attached to the body platform. The origin of the body frame can be chosen at the centre of mass of the body. The selection of the coordinate axes is not restricted and mainly determined by the navigation applications. The definition of the coordinate axes of the towfish in this thesis is introduced in the following section.

2.2.5 The Sensor Frame (s-frame)

The sensor frame specifies the orientations of the sensing axes of a sensor system with respect to a reference system, for example, the tangent plane or the body frame [12]. The configuration of the sensor frame is dependent on applications. For many inertial navigation applications, the same type of sensors are configured in an orthogonal triad configuration. Ideally, the resulting sensor frame is a Cartesian coordinate system and can be attached to the body frame to provide a reference for sensing the motion of the body of interest. However, because of misalignment, these two frames are not perfectly coincide with each other [12]. The transformation between these two frames is discussed in Chapter 4. There are two sensor frames used in the thesis, the orthogonal sensor frame and the realistic sensor frame. The realistic sensor frame specifies the true sensing axes of the sensor system, whereas the orthogonal sensor frame is an orthogonal Cartesian coordinate system transformed from the nonorthogonal realistic sensor frame located at the same origin.

2.3 Towfish Motion Description

The body of interest in this application is the towfish. A Cartesian coordinate system is attached to the towfish with the origin placed at the centre of gravity of the towfish (see Figure 2.3). The y axis is aligned with the towfish pointing forward. Since the y axis is along the image signal sampling track, it is also called the along-track axis. The x axis, named the cross-track axis, is orthogonal to the receiver keel hung below the fins at the rear of the towfish. The z axis points up to complete the right-handed coordinate system of the towfish. The rotation about the z axis is referred to as direction.

Although the towfish is driven externally, it is not constrained to shift and rotate. It has six degrees of freedom for three translational motions and three rotational motions as shown in Figure 2.3.

The definitions of the translational motions are:

Sway is the translational motion along the x axis. A positive sway motion is defined as a translational movement along the x axis towards the positive

direction of the x axis.

Surge is the translational motion along the y axis. A positive surge motion is defined as a translational movement along the y axis towards the positive direction of the y axis.

Heave is the translational motion along the z axis. A positive heave motion is defined as a translational movement along the z axis towards the positive direction of the z axis.

The definitions of the rotational motions are listed below.

Pitch is the rotational motion around the x axis. Zero pitch is achieved when the y axis aligns horizontally with the local level frame. A positive pitch motion is defined as a clockwise rotation around the x axis. For example, lifting the nose of the towfish up is a positive pitch.

Roll is the rotational motion around the y axis. Zero roll is achieved when the x axis aligns horizontally with the local level frame. A positive roll motion is

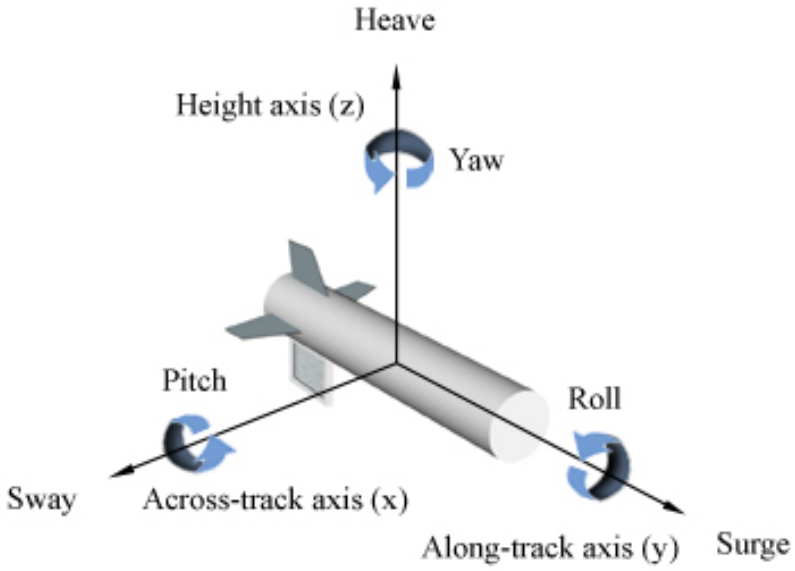

Figure 2.3. The towfish body coordinate and motions including rotational motion (pitch, roll, and yaw) and translational motion (sway, surge, and heave).

defined as a clockwise rotation around the y axis. For example, rolling the receiver keel away from the positive direction of the x axis of the towfish is a positive roll.

Yaw is the rotational motion around the z axis. Zero yaw is achieved when the y axis aligns horizontally with the true north. A positive yaw motion is defined as a clockwise rotation around the z axis. For example, swinging the nose of the towfish away from the positive direction of the x axis of the towfish is a positive yaw.

2.4 Coordinate Transformations and Attitude Parameterizations

The frames of reference were introduced in the last section. In order to transform vectors in one frame of reference to another, or express rotation or attitude in a coordinate system, the techniques of transformations are needed. There are a few commonly used techniques for parameterizing the transformations, which are the direction cosine matrix, Euler angles, and quaternions. Each method has its own advantages and disadvantages. In this section, the basics of the coordinate transformation are presented in detail. Numerous parameterization techniques and the relationships among these methods are also given. At the end of this section, the coordinate transformation from the Earth frame to the tangent plane is described.

2.4.1 Direction Cosine Matrix

The Direction Cosine Matrix (DCM) is the rotation matrix that rotates a vector from one coordinate frame to the other. Taking $\mathbf{i}$, $\mathbf{j}$, and $\mathbf{k}$ as the orthogonal unit vectors, the DCM from frame b to frame a equals [12]

$$\mathbf{R}_{b2a} = \begin{bmatrix} \mathbf{i}^a \cdot \mathbf{i}^b & \mathbf{i}^a \cdot \mathbf{j}^b & \mathbf{i}^a \cdot \mathbf{k}^b \\ \mathbf{j}^a \cdot \mathbf{i}^b & \mathbf{j}^a \cdot \mathbf{j}^b & \mathbf{j}^a \cdot \mathbf{k}^b \\ \mathbf{k}^a \cdot \mathbf{i}^b & \mathbf{k}^a \cdot \mathbf{j}^b & \mathbf{k}^a \cdot \mathbf{k}^b \end{bmatrix}$$

$$= \begin{bmatrix} \cos(\alpha_1) & \cos(\beta_1) & \cos(\gamma_1) \\ \cos(\alpha_2) & \cos(\beta_2) & \cos(\gamma_2) \\ \cos(\alpha_3) & \cos(\beta_3) & \cos(\gamma_3) \end{bmatrix} \tag{2.7}$$

where the symbol $\cdot$ is used to denote the dot product of two vectors. The DCM is an orthonormal 3×3 matrix consisting of the cosine of the angles between the axes of the two coordinate frames. Because of the orthonormality of the DCM, only three of the nine numbers are independent and the other six are constrained correspondingly.

For estimating coordinate system relative rotations, the derivative of the DCM is required. Assume that, during the time interval of each relative rotation, the instantaneous angular velocity between two relative coordinate systems named frame a and frame b, is $\boldsymbol{\omega}_{ba}^{a}$. The notation $\boldsymbol{\omega}_{ba}^{a}$ denotes the rate of angular rotation of frame a relative to frame b in the coordinate system of frame a and its components are $(\omega_x, \omega_y, \omega_z)^T$. The derivative of the DCM can be calculated using [12]

$$\dot{\mathbf{R}}_{b2a}(t) = -\boldsymbol{\Omega}_{ba}^{a}\mathbf{R}_{b2a}(t) \tag{2.8}$$

where $\boldsymbol{\Omega}_{ba}^{a}$ is the skew-symmetric form of $\boldsymbol{\omega}_{ba}^{a}$

$$\boldsymbol{\Omega}_{ba}^{a} = \begin{bmatrix} 0 & \omega_z & -\omega_y \\ -\omega_z & 0 & \omega_x \\ \omega_y & -\omega_x & 0 \end{bmatrix} \tag{2.9}$$

2.4.2 Euler Angles

Another common way of parameterizing the transformation matrix is by the use of Euler angles. They consist of pitch θ_x, roll θ_y, and yaw θ_z with the subscripts x, y, and z defined corresponding to the towfish's coordinate axes mentioned in Section 2.3. For coordinate transformations, the DCM can be derived from three successive plane rotations involving the Euler angles. Since matrix multiplication is not commutative, the order of rotation is not commutative. Different Euler angle sequences may be implemented [9, 13]. For example, the order of plane rotations can be roll, pitch and yaw.

A sequence of rotations in the order of pitch θ_x, roll θ_y, and yaw θ_z for transformations from the towfish's body frame to the tangent plane was implemented in this work. The DCM can be determined using

$$\mathbf{R}_{b2t} = \mathbf{R}_z \mathbf{R}_y \mathbf{R}_x \tag{2.10}$$

where

$$\begin{aligned}
\mathbf{R}_x &= \begin{bmatrix} 1 & 0 & 0 \\ 0 & \cos\theta_x & -\sin\theta_x \\ 0 & \sin\theta_x & \cos\theta_x \end{bmatrix} \\
\mathbf{R}_y &= \begin{bmatrix} \cos\theta_y & 0 & \sin\theta_y \\ 0 & 1 & 0 \\ -\sin\theta_y & 0 & \cos\theta_y \end{bmatrix} \\
\mathbf{R}_z &= \begin{bmatrix} \cos\theta_z & -\sin\theta_z & 0 \\ \sin\theta_z & \cos\theta_z & 0 \\ 0 & 0 & 1 \end{bmatrix}
\end{aligned}$$

Therefore, a vector $\mathbf{e}$ in the body frame can be transformed into the tangent plane using:

$$\mathbf{e}^t = \mathbf{R}_{b2t}\mathbf{e}^b = \begin{bmatrix} \cos\theta_z\cos\theta_y & -\sin\theta_z\cos\theta_x + \cos\theta_z\sin\theta_y\sin\theta_x & \sin\theta_z\sin\theta_x + \cos\theta_z\sin\theta_y\cos\theta_x \\ \sin\theta_z\cos\theta_y & \cos\theta_z\cos\theta_x + \sin\theta_z\sin\theta_y\sin\theta_x & -\cos\theta_z\sin\theta_x + \sin\theta_z\sin\theta_y\cos\theta_x \\ -\sin\theta_y & \cos\theta_y\sin\theta_x & \cos\theta_y\cos\theta_x \end{bmatrix} \mathbf{e}^b \tag{2.11}$$

According to the orthonormality of the Direction Cosine Matrix, the rotation matrix used for transformation from the tangent plane to the body frame is

$$\mathbf{R}_{t2b} = \mathbf{R}_{b2t}^T \tag{2.12}$$

Since the integrated angular rate sensors are rigidly attached to the body frame, the angular rates (ω_x, ω_y, and ω_z) of the body frame are directly measured. The transformation between the angular rates of the body frame and the derivatives of

the Euler angles can be expressed as [12]

$$\begin{bmatrix} \omega_x \\ \omega_y \\ \omega_z \end{bmatrix} = \begin{bmatrix} 1 & 0 & -\sin\theta_y \\ 0 & \cos\theta_x & \cos\theta_y \sin\theta_x \\ 0 & -\sin\theta_x & \cos\theta_y \cos\theta_x \end{bmatrix} \begin{bmatrix} \frac{d\theta_x}{dt} \\ \frac{d\theta_y}{dt} \\ \frac{d\theta_z}{dt} \end{bmatrix} \tag{2.13}$$

The inverse transformation of the above equation gives the definition of the Euler angle derivatives as

$$\begin{bmatrix} \frac{d\theta_x}{dt} \\ \frac{d\theta_y}{dt} \\ \frac{d\theta_z}{dt} \end{bmatrix} = \begin{bmatrix} 1 & \sin\theta_x \tan\theta_y & \cos\theta_x \tan\theta_y \\ 0 & \cos\theta_x & -\sin\theta_x \\ 0 & \frac{\sin\theta_x}{\cos\theta_y} & \frac{\cos\theta_x}{\cos\theta_y} \end{bmatrix} \begin{bmatrix} \omega_x \\ \omega_y \\ \omega_z \end{bmatrix} \tag{2.14}$$

A singularity occurs in Equation 2.14, when the pitch angle θ_x goes to $\pm 90°$. It makes $\sec\theta_x$ and $\tan\theta_x$ undefined. This is also known as "Gimbal lock", a term originally describing the collapse situation in the gimbal mechanism caused by the alignment of two of the three gimbals so that one of the rotations is cancelled [14]. Despite this, Euler angles are intuitive and have been widely used in virtual reality, orientation tracking, and so on [9, 13].

2.4.3 Quaternions

A quaternion is a four-dimension vector and a linear combination of four quaternion elements 1, $\mathbf{i}$, $\mathbf{j}$, and $\mathbf{k}$. The latter three elements correspond to unit vectors along the coordinate axes. Every quaternion can be uniquely expressed in the form of

$$\mathbf{q} = q_0 + q_1\mathbf{i} + q_2\mathbf{j} + q_3\mathbf{k}$$

where q_0, q_1, q_2, and q_3 are real numbers. The fundamental formula for quaternion multiplication is

$$\mathbf{i} \circ \mathbf{i} = \mathbf{j} \circ \mathbf{j} = \mathbf{k} \circ \mathbf{k} = \mathbf{i} \circ \mathbf{j} \circ \mathbf{k} = -1$$

where the symbol $\circ$ is used to denote the quaternion product.

Quaternions provide a useful tool for formulating the composition of arbitrary

spatial rotations. Providing a vector $\mathbf{e}$ in the tangent plane as a pure quaternion $\mathbf{e}_t = 0 + e_1\mathbf{i} + e_2\mathbf{j} + e_3\mathbf{k}$, for example, the transformation of this vector from the tangent plane to the body frame can be expressed via the unit quaternion $\mathbf{q}$ as

$$\begin{aligned}
\mathbf{e}^b &= \mathbf{q} \circ \mathbf{e}^t \circ \mathbf{q}^* \\
&= \begin{bmatrix} q_0 & -q_1 & -q_2 & -q_3 \\ q_1 & q_0 & -q_3 & q_2 \\ q_2 & q_3 & q_0 & -q_1 \\ q_3 & -q_2 & q_1 & q_0 \end{bmatrix} \begin{bmatrix} 0 & -e_1 & -e_2 & -e_3 \\ e_1 & 0 & -e_3 & e_2 \\ e_2 & e_3 & 0 & -e_1 \\ e_3 & -e_2 & e_1 & 0 \end{bmatrix} \begin{bmatrix} q_0 \\ -q_1 \\ -q_2 \\ -q_3 \end{bmatrix} \\
&= \begin{bmatrix} q_0 & -q_1 & -q_2 & -q_3 \\ q_1 & q_0 & -q_3 & q_2 \\ q_2 & q_3 & q_0 & -q_1 \\ q_3 & -q_2 & q_1 & q_0 \end{bmatrix} \begin{bmatrix} q_0 & q_1 & q_2 & q_3 \\ -q_1 & q_0 & -q_3 & q_2 \\ -q_2 & q_3 & q_0 & -q_1 \\ -q_3 & -q_2 & q_1 & q_0 \end{bmatrix} \begin{bmatrix} 0 \\ e_1 \\ e_2 \\ e_3 \end{bmatrix} \\
&= \begin{bmatrix} 1 & 0 & 0 & 0 \\ 0 & 1-2q_2^2-2q_3^2 & 2q_1q_2-2q_0q_3 & 2q_1q_3+2q_0q_2 \\ 0 & 2q_1q_2+2q_0q_3 & 1-2q_1^2-2q_3^2 & 2q_2q_3-2q_0q_1 \\ 0 & 2q_1q_3-2q_0q_2 & 2q_2q_3+2q_0q_1 & 1-2q_1^2-2q_2^2 \end{bmatrix} \mathbf{e}^t
\end{aligned} \tag{2.15}$$

where $\mathbf{q}^*$ is the conjugate of the quaternion $\mathbf{q}$ and defined as

$$\mathbf{q}^* = q_0 - q_1\mathbf{i} - q_2\mathbf{j} - q_3\mathbf{k}$$

Consequently, when quaternions are used, the DCM for transforming vectors from the tangent plane to the body frame is

$$\mathbf{R}_{t2b} = \begin{bmatrix} 1-2q_2^2-2q_3^2 & 2q_1q_2-2q_0q_3 & 2q_1q_3+2q_0q_2 \\ 2q_1q_2+2q_0q_3 & 1-2q_1^2-2q_3^2 & 2q_2q_3-2q_0q_1 \\ 2q_1q_3-2q_0q_2 & 2q_2q_3+2q_0q_1 & 1-2q_1^2-2q_2^2 \end{bmatrix} \tag{2.16}$$

By comparison of the DCM equations formulated in Euler angles and quaternions (Equation 2.11 and Equation 2.16), the Euler angles can be calculated using quaternions:

$$\theta_x = \arctan2\left[2q_2q_3 - 2q_0q_1, 1 - 2q_1^2 - 2q_2^2\right] \tag{2.17}$$

$$\theta_y = \arcsin\left(-2q_1q_3 - 2q_0q_2\right) \tag{2.18}$$

$$\theta_z = \arctan2\left[2q_1q_2 - 2q_0q_3, 1 - 2q_2^2 - 2q_3^2\right] \tag{2.19}$$

The quaternion can also be expressed using a known DCM (see Equation 2.16) in the formulation of [12]

$$\mathbf{q} = \begin{bmatrix} \sqrt{1 + \mathbf{R}_{t2b}[1,1] + \mathbf{R}_{t2b}[2,2] + \mathbf{R}_{t2b}[3,3]}/2 \\ (\mathbf{R}_{t2b}[3,2] - \mathbf{R}_{t2b}[2,3])/4q_0 \\ (\mathbf{R}_{t2b}[1,3] - \mathbf{R}_{t2b}[3,1])/4q_0 \\ (\mathbf{R}_{t2b}[2,1] - \mathbf{R}_{t2b}[1,2])/4q_0 \end{bmatrix} \tag{2.20}$$

The quaternion derivatives can be deduced using the angular rate measurements as [12]

$$\begin{aligned} \dot{\mathbf{q}} &= \begin{bmatrix} \dot{q}_0 \\ \dot{q}_1 \\ \dot{q}_2 \\ \dot{q}_3 \end{bmatrix} = \frac{1}{2} \begin{bmatrix} q_1 & q_2 & q_3 \\ -q_0 & q_3 & -q_2 \\ -q_3 & -q_0 & q_1 \\ q_2 & -q_1 & -q_0 \end{bmatrix} \begin{bmatrix} \omega_x \\ \omega_y \\ \omega_z \end{bmatrix} \\ &= \frac{1}{2} \begin{bmatrix} 0 & \omega_x & \omega_y & \omega_z \\ -\omega_x & 0 & -\omega_z & \omega_y \\ -\omega_y & \omega_z & 0 & -\omega_x \\ -\omega_z & -\omega_y & \omega_x & 0 \end{bmatrix} \begin{bmatrix} q_0 \\ q_1 \\ q_2 \\ q_3 \end{bmatrix} = \frac{1}{2}\mathbf{\Psi}\mathbf{q} \end{aligned} \tag{2.21}$$

where ω_x, ω_y, and ω_z represent pitch, roll, and yaw angular rates around the towfish coordinate axes x, y, and z, respectively, and $\mathbf{\Psi}$ is a skew symmetric matrix given by

$$\mathbf{\Psi} = \begin{bmatrix} 0 & \omega_x & \omega_y & \omega_z \\ -\omega_x & 0 & -\omega_z & \omega_y \\ -\omega_y & \omega_z & 0 & -\omega_x \\ -\omega_z & -\omega_y & \omega_x & 0 \end{bmatrix}$$

The discrete form of the quaternion derivative equation has to be determined. Assuming that the angular rates are constant between a time interval $\triangle t$, the

first-order discrete equation is derived as

$$\begin{aligned}\mathbf{q}_{n+1} &= \mathbf{q}_n + \dot{\mathbf{q}}_n \triangle t = (\mathbf{I} + \frac{1}{2}\Psi \triangle t)\mathbf{q}_n \\ &= \frac{1}{2}\begin{bmatrix} 2 & \omega_x \triangle t & \omega_y \triangle t & \omega_z \triangle t \\ -\omega_x \triangle t & 2 & -\omega_z \triangle t & \omega_y \triangle t \\ -\omega_y \triangle t & \omega_z \triangle t & 2 & -\omega_x \triangle t \\ -\omega_z \triangle t & -\omega_y \triangle t & \omega_x \triangle t & 2 \end{bmatrix} \mathbf{q}_n \end{aligned} \tag{2.22}$$

The orientation parameterization using quaternions avoids the singularities of Euler angles. However, since the manoeuvres of the towfish rarely exceed the pitch angle $\pm 90°$, this is not significantly advantageous. Quaternions also have the advantage of simplicity and efficiency, which make them a common way to represent rotations in robotics, virtual reality, tracking, and other real-time applications [15, 16].

2.4.4 Geodetic-coordinate-to-tangent-plane Transformations

A variety of advanced navigation technologies are available, such as global position system technology and inertial navigation technology. However, each technology has different frame of reference [12]. GPS technology implements satellites in the space to pinpoint the target of interest in the parameter of longitude, latitude, and altitude with respect to the Earth's geodetic coordinate, whereas inertial navigation technology provides position and orientation measurements relative to the body frame. For local navigation applications, the scope of a smaller range is often on focus, and the navigation area of interest is often assumed to be flat, which is called the tangent plane. In order to fuse all the valuable navigation information, the tangent plane is chosen as the common ground. In the previous section, the coordinate transformation between the body frame and the tangent plane is discussed. This part of the section is focused on the transformation between the geodetic coordinate and the tangent plane.

The whole transformation process can be split into two parts. The first part is the transformation from the Earth's geodetic coordinate to the Earth's rectangular coordinate, which is introduced in Section 2.2.2. The transformation from the rectangular coordinate to the tangent plane coordinate is the second part.

The transformation from the Earth's rectangular coordinate to the tangent plane's North-East-Up (N-E-U) axes can be accomplished by a sequence of plane rotations. There are only two plane rotations required, a plane rotation around the z axis of the rectangular coordinate to align the x axis with the east axis (x axis) of the tangent plane and a sequential plane rotation about the new x' axis to align the z axis with the up axis of the tangent plane [12]. Therefore, with ϕ and λ representing longitude and latitude, the transformation matrix from the rectangular coordinate to the tangent plane coordinate is defined by

$$\mathbf{R}_{e2t} = \mathbf{R}_z \mathbf{R}_x \tag{2.23}$$

where

$$\begin{aligned} \mathbf{R}_z &= \begin{bmatrix} -\sin\phi & \cos\phi & 0 \\ -\cos\phi & \sin\phi & 0 \\ 0 & 0 & 1 \end{bmatrix} \\ \mathbf{R}_x &= \begin{bmatrix} 1 & 0 & 0 \\ 0 & -\sin\lambda & -\cos\lambda \\ 0 & \sin\lambda & -\cos\lambda \end{bmatrix} \end{aligned}$$

2.5 Kalman Filter

The Kalman filter is named after Rudolph E. Kalman, who published his research on a recursive solution to the discrete filtering problem in 1960 [4]. It has been used in a wide range of engineering applications for almost a half century to produce an optimal estimation for unknown states of a dynamic system from a variety of measurements corrupted by noise.

The Kalman filter is a recursive observer using two phases, the predict phase and the correct phase [10]. It implements only the estimated state from the previous time step for computing the current state in the predict phase. In the correct phase, the measurements from the current time step are used to update the predicted result to achieve the final optimized state estimation of the time step. A wide variety of Kalman filters have been developed based on the predict-correct philosophy, for example, the original linear Kalman filter, the extended Kalman

filter, and the unscented Kalman filter [10, 17]. In the following, the basic discrete Kalman filter is presented and the extended Kalman filter for nonlinear system estimation is given in detail.

2.5.1 Discrete Kalman Filters

In order to predict the state of interest at discrete points in time, a process model for expressing the characteristics of the referred system is required. The process model is assumed to be linear, and is governed by the equation [10]

$$\mathbf{x}_k = \mathbf{A}_k\mathbf{x}_{k-1} + \mathbf{B}_k\mathbf{u}_k + \mathbf{w}_{k-1} \tag{2.24}$$

where k is the current time step, $\mathbf{x}_k$ is the state vector at step k, $\mathbf{A}_k$ is the state transition matrix for the model, and $\mathbf{B}_k$ relates the control input $\mathbf{u}_k$. Since the measurements are prone to errors, the actual observation model at time k is [10]

$$\mathbf{z}_k = \mathbf{H}_k\mathbf{x}_k + \mathbf{v}_k \tag{2.25}$$

where $\mathbf{H}_k$ is the measurement matrix relating the measurement vector $\mathbf{z}_k$ to the system state, and where $\mathbf{w}_k$ and $\mathbf{v}_k$ represent the process and measurement noise, respectively. They are assumed to be *white* and *Gaussian* with zero mean and covariance matrices $\mathbf{Q}$ and $\mathbf{R}$. The covariance matrices are given by

$$\mathbf{Q}_k = \mathrm{E}[\mathbf{w}_k\mathbf{w}_k^T] = \mathrm{E}[\mathbf{w}_k^2] \tag{2.26}$$

and

$$\mathbf{R}_k = \mathrm{E}[\mathbf{v}_k\mathbf{v}_k^T] = \mathrm{E}[\mathbf{v}_k^2] \tag{2.27}$$

Theoretically, the state transition matrix, $\mathbf{A}_k$, the measurement matrix, $\mathbf{H}_k$, the input control matrix, $\mathbf{B}_k$, the process noise covariance matrix, $\mathbf{Q}_k$, and the measurement noise covariance matrix, $\mathbf{R}_k$, are assumed to be constant.

Two state estimates at step k relative to the true state vector $\mathbf{x}_k$ are defined as the *a priori* state estimate $\hat{\mathbf{x}}_k^-$ and the *a posteriori* state estimate $\hat{\mathbf{x}}_k$, which represent the estimates prior to the time step k and after the update of the measurement

$\mathbf{z}_k$, respectively. An *a priori* state estimate is computed using

$$\hat{\mathbf{x}}_k^- = \mathbf{A}\hat{\mathbf{x}}_{k-1} + \mathbf{B}\mathbf{u}_k \tag{2.28}$$

The corresponding *a priori* and *a posteriori* error covariance matrices are given by [10]

$$\begin{aligned} \mathbf{P}_k^- &= \mathrm{E}[(\mathbf{x}_k - \hat{\mathbf{x}}_k^-)(\mathbf{x}_k - \hat{\mathbf{x}}_k^-)^T] \\ \mathbf{P}_k &= \mathrm{E}[(\mathbf{x}_k - \hat{\mathbf{x}}_k)(\mathbf{x}_k - \hat{\mathbf{x}}_k)^T] \end{aligned}$$

The *a posteriori* state estimate can be computed as [10]

$$\hat{\mathbf{x}}_k = \hat{\mathbf{x}}_k^- + \mathbf{K}_k(\mathbf{z}_k - \mathbf{H}\hat{\mathbf{x}}_k^-) \tag{2.29}$$

where $\mathbf{K}_k$ is the Kalman gain that minimizes the *a posteriori* error covariance. The Kalman gain $\mathbf{K}_k$ at step k is given by [10]

$$\mathbf{K}_k = \mathbf{P}_k^-\mathbf{H}^T(\mathbf{H}\mathbf{P}_k^-\mathbf{H}^T + \mathbf{R})^{-1} \tag{2.30}$$

Note that the Kalman gain approaches zero as the measurement noise covariance $\mathbf{R}$ increases and rises up to $\mathbf{H}^{-1}$ as the *a priori* state estimate error covariance $\mathbf{P}_k^-$ increases. This can be interpreted that the measurement $\mathbf{z}_k$ is less emphatic when the measurement noise is bigger and is more emphatic when the state estimation is less accurate.

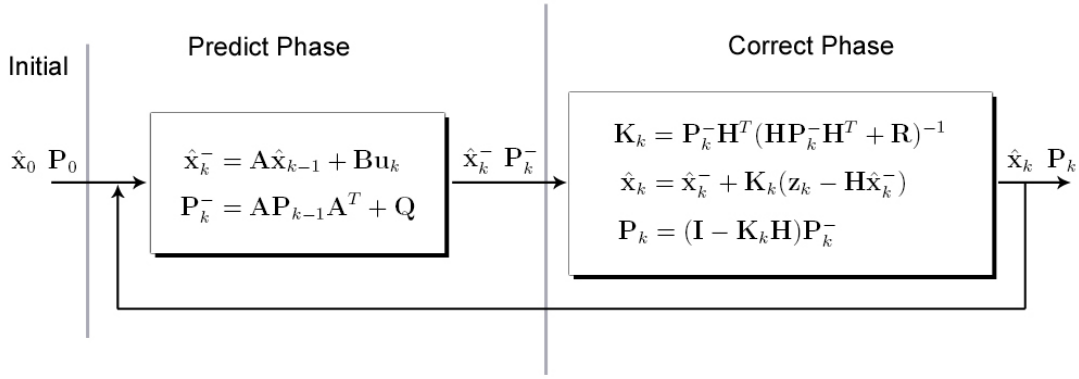

Figure 2.4. Illustration of the discrete Kalman filter structure [10].

The basic recursive structure of a discrete Kalman filter can be illustrated in a diagram (see Figure 2.4). The initial state and covariance estimates are used to predict the *a prior* state and the corresponding error covariance of the next step. During the correct phase, the Kalman gain is determined first. Then, an *a posteriori* state estimate is generated and folded back together with the obtained *a posteriori* error covariance to update the process model and start a new cycle.

2.5.2 Extended Kalman Filters

The standard discrete Kalman filters are limited to linear system estimation. When dealing with nonlinear dynamics or nonlinear measurements, a nonlinear Kalman filter is needed. An extended Kalman filter is a nonlinear Kalman filter that linearizes the process and observation models using partial derivatives to achieve nonlinear state estimates.

The nonlinear process and observation models can be described as

$$\mathbf{x}_k = f(\mathbf{x}_{k-1}, \mathbf{u}_k, \mathbf{w}_{k-1}) \tag{2.31}$$

$$\mathbf{z}_k = h(\mathbf{x}_k, \mathbf{v}_k) \tag{2.32}$$

Using the nonlinear models, the *a priori* state estimate and the predicted measurement can be directly computed as

$$\hat{\mathbf{x}}_k^- = f(\hat{\mathbf{x}}_{k-1}, \mathbf{u}_k, 0) \tag{2.33}$$

$$\hat{\mathbf{z}}_k^- = h(\hat{\mathbf{x}}_k^-, 0) \tag{2.34}$$

However, when calculating error covariance and Kalman gain, partial derivatives of nonlinear functions f and h are used for each time step. The first partial derivatives of the process and observation models are defined to be the following Jacobian matrices

$$\mathbf{A}_k = \frac{\partial f(\hat{\mathbf{x}}_{k-1}, \mathbf{u}_k, 0)}{\partial \mathbf{x}_k} \tag{2.35}$$

$$\mathbf{H}_k = \frac{\partial h(\hat{\mathbf{x}}_k^-, 0)}{\partial \mathbf{x}_k} \tag{2.36}$$

Extended Kalman filtering has been proven to be adequate in many navigation applications [18, 6]. However, frequent access to Jacobian calculation during an estimation cycle considerably increases time consumption and computational demand, which makes it less favorable in real-time applications.

CHAPTER 3

NAVIGATION CARD DESIGN AND IMPLEMENTATION

3.1 Introduction

The Synthetic Aperture Sonar (SAS) designed and built by the Acoustics Research Group at the University of Canterbury is named KiwiSAS. The navigation card is located inside a sealed can at the rear of the KiwiSAS towfish. The design of the navigation card started with an overview of the present available navigation technologies.

Inertial Measurement Units (IMU) have been used widely for navigation and motion tracking applications. IMUs are capable of providing both translational and rotational measurements. The decreasing cost and size as well as improved performance of Micro-Electro-Mechanical System (MEMS) inertial sensors allow inertial measurement units to be used for low-cost navigation applications. Typically they are combinations of three accelerometers and three angular rate sensors in a triaxial configuration.

MEMS accelerometers and rate gyroscopes utilize differential capacitance and the Coriolis effect to measure translational and angular acceleration. These sensors are considered strapdown devices since they have no moving or pendulous parts, which eliminates the need for mechanical gimbals [19]. However, these sensors have considerable errors, such as bias, and are dramatically affected by temperature. Therefore, the combination of inertial measurement units and other technologies becomes necessary. IMUs and GPS are often integrated to form a navigation unit to take advantage of the complementary nature of the two navigation technologies [18, 20]. However, the limited water-penetrating capability of electromagnetic waves makes GPS unsuitable for underwater navigation. Another motion tracking technology, which has been widely used, is magnetic tracking. Magnetometers measure the local magnetic field vector and, in spite of iron disturbances, provide long-term stability similar to GPS. Magnetic, Angular Rate, and Gravity (MARG) sensors have been used for motion tracking applications, as in [16] and [21].

An integrated navigation system based on MARG sensors was considered and built as shown in Figure 3.1. The card is built on a four-layer 180 mm standard sized Eurocard PCB with a DIN41612 edge connector to provide power. The schematic for the navigation card can be found in Appendix B. This chapter presents the integrated MARG sensors and summarizes the hardware configuration of the integrated navigation system.

3.2 Integrated MARG Sensors

The designed integrated navigation system contains three accelerometers, three angular rate gyros, and a magnetic hybrid in a triaxial configuration (see Figure 3.1). As shown at the lower left corner of the navigation card, the inertial modules are assembled orthogonal to each other to ensure the orthogonality of the sensing axes of the accelerometer and magnetometer triad. Because the accelerometers used in each inertial measurement module are dual-axis, in each axis in the body frame there are two sets of linear acceleration measurements. This section states the integrated sensing device specifications and capabilities.

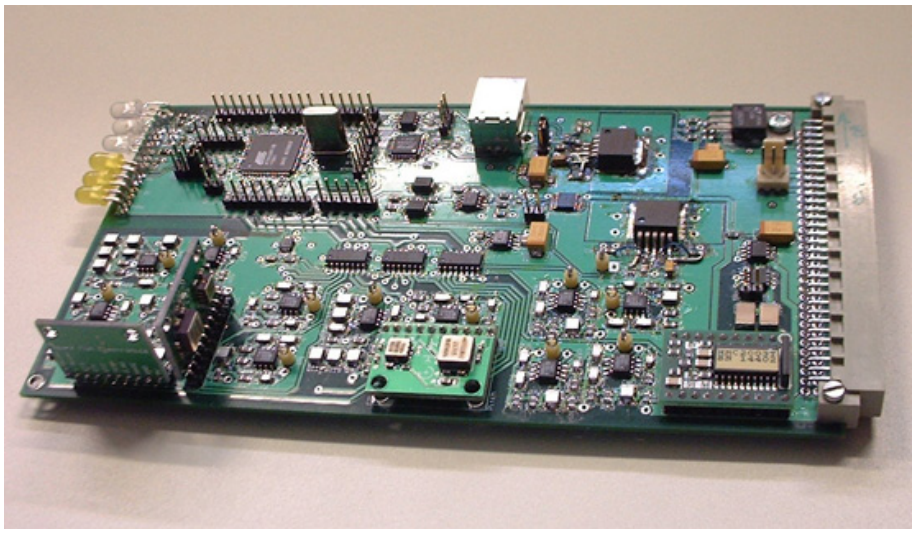

Figure 3.1. The navigation card for the KiwiSAS towfish with a PCB dimension of 100 mm by 180 mm and DIN41612 (Type B) edge connector. Note that three identical inertial measurement modules are located at the lower left corner and the magnetic hybrid is mounted horizontally at the lower right corner.

3.2.1 Inertial Measurement Units

Analog Devices provides varieties of low-cost MEMS-based sensors, including ADXRS series rate gyroscopes and ADXL series accelerometers available in a tiny Ball Grid Array (BGA) package. The MEMS sensors have the advantage that they require low power and have good reliability. However, the BGA footprint of these sensors makes hand-soldering tedious and impractical considering all the components on the navigation card prototype are meant to be hand-soldered. Sparkfun Electronics [22] supplies modules with these MEMS sensors pre-mounted on a circuit board (see Figure 3.2).

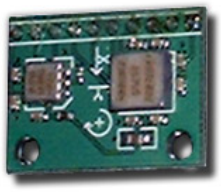

Figure 3.2. Inertial measurement unit combo board from Sparkfun. The dimensions are 20×25.4 mm.

Each IMU combo board contains one ADXRS401 rate gyroscope and a dual-

axial ADXL203 accelerometer. It has the ability to conduct two degrees of freedom measurements. The characteristics of ADXRS401 and ADXL203 are given in Table 3.1 and Table 3.2, respectively [23]. Considering that the dynamic characteristic of the towfish is slowly accelerating and rotating, the range of the gyroscopes and accelerometers is sufficient for monitoring the towfish's motions. Also, the bias drift temperature coefficient and the measurement noise of the inertial sensors are considerably low, which makes the inertial measurement modules desirable for this work.

Table 3.1. Rate gyroscope ADXRS401 specifications.

Characteristics	Units	Range
Supply Voltage	V	4.75 – 5.25
Dynamic Range	°/s	−75 – 75
Scale Factor	mV/°/s	15
Initial Null	V	2.5
Null Shift Tempco	mV/°C	1
Nonlinearity	%	0.1
Noise Density	$°/s/\sqrt{Hz}$	0.06
Temperature Vout at 298K	V	2.5
Temperature Scale Factor	mV/K	8.4
Dimensions	mm^3	7 x 7 x 3

Each IMU combo board provides an angular rate voltage output about the axis normal to the top surface of the assembled board and two acceleration voltage outputs on the longitudinal axis and the lateral axis of the assembled board, respectively. Since an ADXRS401 gyroscope has an internal temperature sensor and 2.5 V precision output, the temperature sensor voltage output and 2.5 V reference voltage output are also available from the output pins of the assembled board. Both inertial sensors share power supply and ground signals connected externally through the 5 V power input pin and ground connection pin on the board.

On the IMU boards, capacitors are added close to the inertial sensor signal outputs to implement low-pass filtering for anti-aliasing and noise reduction. The bandwidth of the accelerometer ADXL203 is configured as 500 Hz with 0.01 μF filter capacitor connected with each acceleration signal output pin. For the rate

Table 3.2. Accelerometer ADXL203 specifications.

Characteristics	Units	Range
Supply Voltage	V	3 – 6
Dynamic Range	g	−1.7 – 1.7
Scale Factor	V/g	1
Scale Factor Tempco	ppm/°C	±17
Zero g Bias	V	2.4 – 2.6
Initial 0 g Output Deviation from Ideal (25°C)	mg	±25
0 g Offset Tempco	mg/°C	±0.1
Nonlinearity	%	0.5
Noise Density	$\mu g/\sqrt{Hz}$	110
x and y Axes Alignment Error		±0.1°
Dimensions	mm^3	5 x 5 x 2

gyro ADXRS401, a 22 nF bandwidth limit capacitor is added, and the bandwidth is modified to 40 Hz. The bandwidth of the analog signals is further reduced by the low-pass filters integrated on the navigation card discussed in the next section.

3.2.2 Magnetometers

There are a number of different types of magnetometer available for the Earth's magnetic field detection. According to the sensing methodologies, there are mainly three types of magnetic sensor for the Earth's magnetic detection, which include fluxgate sensors, magnetoinductive (MI) sensors, and magnetoresistive (MR) sensors. Fluxgate sensors are the most widely used type for compass navigation systems [24]. These sensors provide a low cost means of magnetic field detection but tend to be bulky and have a slow response time. In contrast, MI magnetometers have a much smaller size and shape. However, this makes automatic assembly and axis alignment of this kind of sensor difficult [24]. MR magnetometers constructed with four magnetoresistive resistors in a wheatstone bridge configuration are produced as an integrated circuit and have high sensitivity, short response time, and low cost [24]. Also, the solid-state components provide high reliability and repeatability [24]. The towfish navigation system implements a triaxial MR magnetic sensor HMC2003 produced by Honeywell.

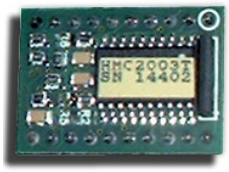

Figure 3.3. Magnetic hybrid HMC2003 from Honeywell. The dimensions are 20×25.4 mm.

Table 3.3. Magnetic Hybrid HMC2003 specifications.

Characteristics	Units	Range
Supply Voltage	V	6 – 15
Dynamic Range	gauss	−2 – 2
Scale Factor	V/gauss	0.98 – 1.02
Scale Factor Tempco	ppm/°C	-600
Null Field Output	V	2.3 – 2.7
Null Field Tempco	ppm/°C	±400
Resolution	μgauss	40
Bandwidth	kHz	1
Dimensions	mm^3	7 x 7 x 3

The HMC2003 is a three-axis magnetometer hybrid using a single axis magnetometer HMC1001 and dual-axial magnetic sensor HMC1002 (see Figure 3.3). Its characteristics are listed in Table 3.3. With 6 – 15 V power supply, the hybrid has three magnetic field strength outputs in the range of 0 – 5 V, 40 μgauss resolution and ±2 gauss dynamic range, well suited for measuring the Earth's magnetic field. The output signal bandwidth of HMC2003 is claimed to be 1 kHz. An internal 2.5 V reference pin is available, which can be used to improve measurement accuracy and stability. A couple of Honeywell patented Set/Reset pins are configured to be powered by strong regular current pulses to compensate for the errors caused by offset drifts. For each axis, there are two offset pins used to drive the internal offset straps. By providing a defined current, the offset strap can generate a magnetic field along the sensitive axis, which can be used to cancel the offset of the magnetometers and any ambient magnetic field [24].

3.3 Hardware Configuration

The navigation card electronics are controlled by an AVR 8-bit AT90CAN128 microcontroller with 12 MHz crystal oscillator. This interfaces with the equipped MARG sensors and communicates with a data collection card located in the transmitter can (see Section 2.1) at the front of the towfish via a Controller Area Network (CAN) bus. The received data can be transmitted over Universal Serial Bus (USB) to the computer in the towfish also contained in the transmitter can. Since the sensors put out analog signals, in order to have high-fidelity analog signals, the printed circuit board (PCB) layout was considered carefully.

For maximum elimination of the interference from digital logic ground to analog circuitry on the mixed-signal four-layer PCB, routing disciplines are followed for component placement and partitioning when laying out the PCB [25]. There are a few aspects of PCB layout to be noticed:

- Analog and digital sections are separated. As shown in Figure 3.1, the analog sensors are all located at the lower half of the PCB. Other electronics including the microcontroller are in the upper left portion, and power regulators are in the upper right portion.

- Analog and digital power planes are separated. Analog sensors except magnetometers are supplied by a 5 V regulator; another 5 V regulator is used for digital electronics power supply; the magnetic hybrid is supplied by a 10 V power regulator; also, the external reference voltage of the programmable gain amplifiers (PGA) is powered by 2.5 V reference power supply.

- One solid ground plane is used for providing a common reference and short ground current return path, which prevents big current loops.

A block diagram is shown in Figure 3.4. In the rest of the section, the construction and functionality of different electronics are described.

3.3.1 Navigation Data Acquisition

The signal obtained from sensors is accompanied by noise as well as vibrations from the towfish. In order to eliminate these disruptions, low-pass filtering was

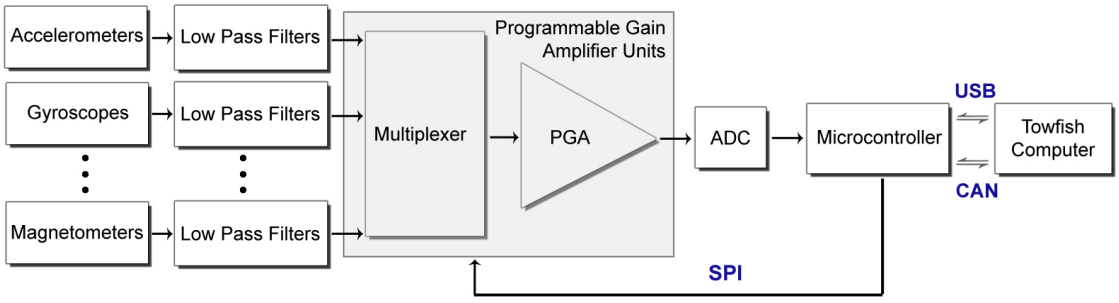

Figure 3.4. A block diagram of the navigation card.

used. Considering that the Butterworth filter provides a good compromise between attenuation and phase response [26] and it has no ripple in the pass band, a fourth-order Butterworth low-pass filter was used to reduce noise and prevent aliasing for each sensor output channel. The Sallen-Key filter topology was chosen. Figure 3.5 shows the unity-gain Sallen-Key circuit configured for low-pass operation.

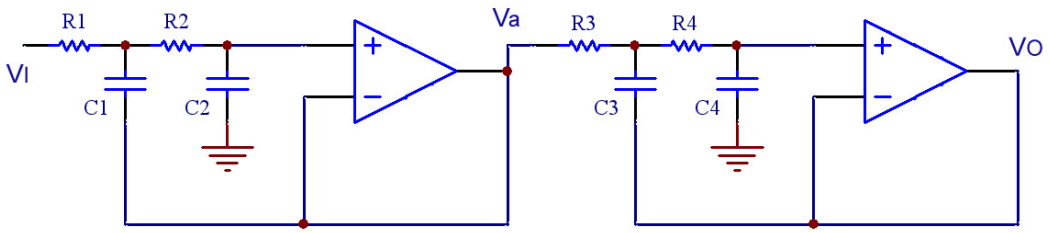

Figure 3.5. A fourth-order unity-gain Sallen-Key low-pass filter.

The filtered analog sensor signals are multiplexed and amplified using three analog Programmable Gain Amplifiers (PGAs) MCP6S28. The MCP6S28 provides eight channels and eight gain selections configurable through a Serial Peripheral Interface (SPI) port [27]. Two PGAs are configured in cascade with another PGA to provide 22 analog input channels. Twenty-one channels are used to sample signals including sensor outputs, temperature signals, and power supply measurements. Each channel can be selected and configured individually via the SPI interface. The cutoff frequency of the anti-aliasing filters and the PGA channel settings are configured as shown in Table 3.4. In order to identify each component clearly, a

navigation card model is displayed in Figure 3.6[1].

Table 3.4. Low-pass filter bandwidth and PGA channel configuration of the navigation data acquisition system.

Sensors		Bandwidth	Body coordinate	PGA channel
IMU-A	Accelerometer x axis	10 Hz	Negative cross-track axis	PGA-A CH1
	Accelerometer y axis	10 Hz	Negative along-track axis	PGA-A CH2
	Gyroscope	10 Hz	Negative yaw	PGA-B CH0
IMU-B	Accelerometer x axis	100 Hz	Negative cross-track axis	PGA-A CH0
	Accelerometer y axis	100 Hz	Height axis	PGA-A CH3
	Gyroscope	30 Hz	Negative roll	PGA-B CH1
IMU-C	Accelerometer x axis	10 Hz	Height axis	PGA-A CH4
	Accelerometer y axis	100 Hz	Negative along-track axis	PGA-A CH5
	Gyroscope	30 Hz	Negative pitch	PGA-B CH2
HMC2003	Magnetometer x axis	30 Hz	Negative along-track axis	PGA-C CH4
	Magnetometer y axis	30 Hz	Negative height axis	PGA-C CH3
	Magnetometer z axis	30 Hz	Cross-track axis	PGA-C CH5

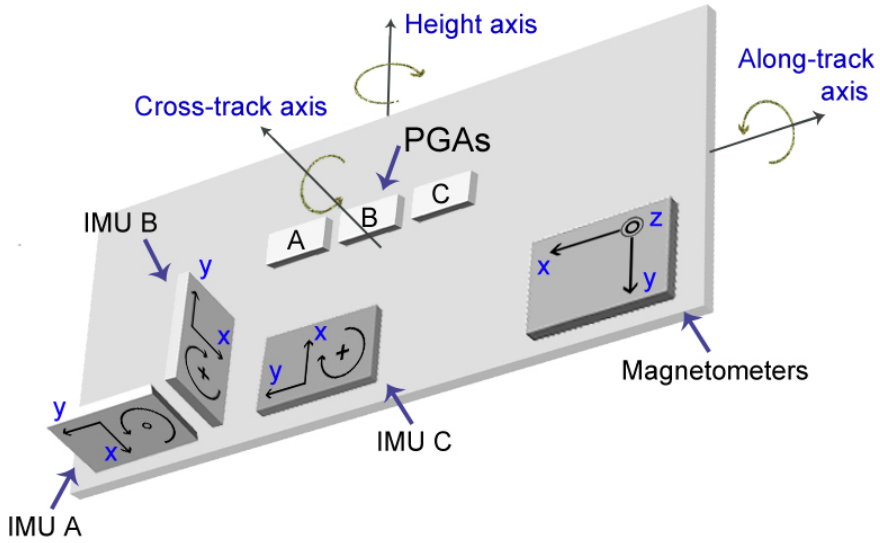

Figure 3.6. A navigation system model showing sensing axes and the body coordinates.

For this multiplexed data acquisition system, a 16-bit Successive Approximation Register (SAR) Analog-to-Digital converter (ADS8325) was selected. It offers

[1]The marking of the ADXL203 accelerometer sensing axes (x and y) on the inertial measurement units is found to be inconsistent with the manufacturer-provided datasheet [23]. The definitions of the datasheet is followed.

excellent linearity, very low noise, and low power dissipation [28]. No pipeline delay makes it ideal for multichannel sampling application [29]. The analog input of the ADS8325 is differential. The inverting analog input is connected to the ground for single-ended operation. Regulated power of 5 V for analog circuits is used to supply the chip and external reference input, which enables the analog input range of 0 V to 5 V. The maximum sampling rate of 100 kHz is sufficient for this application. Also, the ADS8325 has a synchronous 3-wire serial interface compatible with SPI, which provides an easy way for data transfer [28].

A SPI network was constructed for communication among the microcontroller, the PGAs and the ADC. The PGAs and the ADC are driven by the clock signal from the microcontroller SPI interface.

(1) Through the chip select pins and the Master Out - Slave In (MOSI) line of the SPI interface, the microcontroller controls and instructs each PGA individually. Channel and gain setting instructions are transmitted to the corresponding PGAs.

(2) One of PGAs directly ouputs to the signal input pin of the AD convertor. It is called the central PGA. The other two are configured in cascade with the central PGA. When an analog signal is to be sampled, the amplifier that the targeted signal is directly connected to and the central PGA receive the channel and gain configuration instructions and process the commands. The reconstructed targeted signal is put out from the analog output pin of the central PGA.

(3) When the wanted signal is ready, the microcontroller sets the chip select pin ($\overline{\text{CS}}$) of the ADC low, and initiates the conversion and data transfer, so that the Master In - Slave Out (MISO) line of the SPI interface is able to receive the digitized signal.

Since the SPI interface is a synchronous data transfer interface, data is always simultaneously shifted from Master to Slave on the MOSI line and from Slave to Master on the MISO line. However, in this design, only part of the transmission is meaningful. When the microcontroller sends instructions to the PGAs through the MOSI line, the characters read in from the MISO line are ignored, and vice

versa. Therefore, in order for the sampled signals to be read by the MISO line, an all-zero instruction, which means nothing to the PGAs, has to be shifted out from the MOSI line.

3.3.2 Magnetometer Set/Reset

Magnetoresistive (MR) sensors are fabricated with permalloy thin films that change in resistivity with respect to external magnetic fields. The magnetic domains of the film particles are orientated to a certain direction aligned with the sensing axis of the sensor. However, strong magnetic fields (more than 10 gauss) can disrupt the smooth factory orientation to arbitrary directions [30]. The HMC2003 provides an on-chip current strap called the Set/Reset strap for performing re-magnetization and for restoring the sensing characteristics. Also, by using the Set/Reset strap to alternate the sensor output polarity periodically, subtracting two readings eliminates any temperature induced drift and electronics offsets [30].

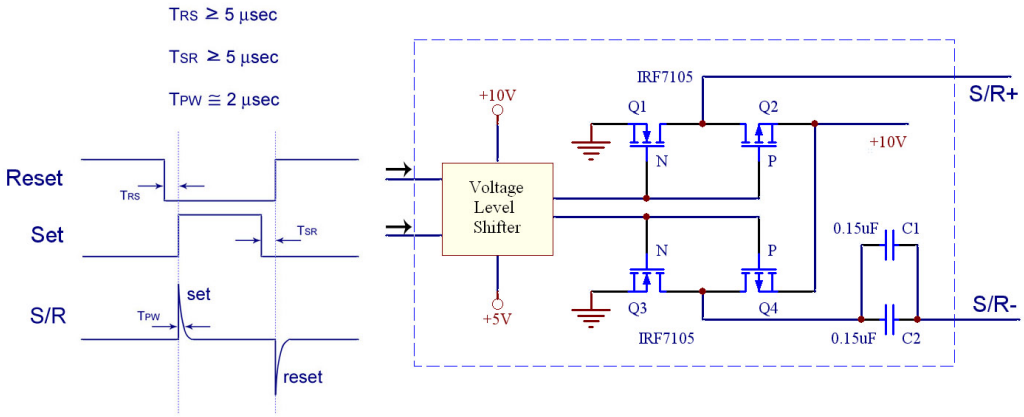

Figure 3.7. The circuit used for the magnetometer Set/Reset functionality [30].

The circuit constructed for providing the strong set/reset pulses is illustrated in Figure 3.7. It is powered by a regulated 10 V supply. The 5 V CMOS logic inputs from the microcontroller are translated by a CMOS voltage level shifter (CD4504B) to 10 V CMOS logic level signals, and drive two P and N channel power metal-oxide-semiconductor field-effect transistors (MOSFET) IRF7105 to produce approximately 20 V across the Set/Reset strap. Because the resistance of the strap is about 4.5 Ω [31], a strong current pulse of approximately 4 amps

```
$PNACC,31344,32499,45084,32057,33036,45336,18000*42
$PNRGY,28440,32158,27537,18001*59
$PNMAG,35054,31130,26448,18002*55
$PNMSC,32607,32555,32632,33120,33132,33118,33089,221,220,18006*45
```

Figure 3.8. An example of the navigation card proprietary NMEA0183 data format.

can be generated with a pulse width of about 2 μs. The set and reset pulses have the same effect on the sensor. The only difference is that the sensor output signal changes sign. Set pulses are defined as pulsed currents that enter the positive pin (S/R+) of the Set/Reset strap.

3.3.3 Data Communication Interface

The sampled navigation data is transmitted to the computer inside the towfish, and streamed from the towfish up the tow-cable to computers on the towboat for storage and display. The CAN bus and USB interface are implemented for the towfish internal data communication.

All the electronics are sealed inside of the towfish pressure housing consisting of a stainless steel canister with a perspex end-cap sealed with o-rings. The navigation card is positioned in the receiver can at the rear of the pressure housing. The top and bottom edges of the board are supported by guide rails, while the rear side of card is held tightly by the edge connector interfaced with the 64-way DIN41612 backplane. Currently, 12 V power input and the CAN interface are available for the navigation card from the DIN41612 bus.

With the equipped CAN transceiver chip, the navigation data is broadcasted to the CAN bus. A data collection card located in the transmitter can at the front of the towfish collects the data available on the CAN bus. The card formats into NMEA strings, and transmits the data over USB to the computer in the towfish also contained in the transmitter can.

A USB-serial converter is integrated on the navigation card for embedded programming and testing purposes. With a 12 V battery connected to the on-board power supply header, the navigation card is able to put out the navigation data via the USB interface in NMEA format so that the integrated navigation system can be individually calibrated and tested.

The implemented navigation card data format is illustrated in Figure 3.8. The format is based on the NMEA0183 standard which is developed for marine interfaces. The data is human readable. It can be easily loaded into computers and for a program to parse for postprocessing.

Each NMEA sentence begins with the character "$", followed by a five character ID. The prefix P shows these sentences are propriety sentences, which are not part of the NMEA standard protocol, and the following letter N stands for navigation. The last three letters of the ID indicate the type of sentence that is being sent. For example, ACC indicates the the signal sentence contains the sampled data from the accelerometers and MSC means that the corresponding sentences have all the miscellaneous sampled data including temperature, voltage reference, and so on. Each NMEA sentence ends with a checksum field, a carriage return and line feed. The checksum field starts with the star character "*" and is implemented to verify the validity of the data. Between the beginning and end of each sentence are ASCII data fields separated by commas. The last field of the ASCII data is the time stamp field indicating time of occurrence.

3.4 Software Flow Diagram

The current embedded software configuration is based on the timer scheme. There is a main loop triggered at a certain frequency set up by the 8-bit timer 2 of the AT90CAN128 microcontroller in Clear Timer on Compare (CTC) mode. Inside the main loop, the MARG sensors' outputs and other analog signals, for example, temperature and voltage reference signals, are sampled and processed. The basic software flowchart is illustrated in Figure 3.9.

The sampling rate of each sensor is configured according to the bandwidth of signal being sampled. The Nyquist theorem[2] is closely followed. The bandwidth setting of each sensing channel can be found in Table 3.4. For the CAN bus configuration, each CAN data packet consists of a sequence number byte, two data bytes, and two time stamps bytes, which gives a total frame length[3] of 87 bits/frame [32].

[2]The Nyquist theorem, also known as the sampling theorem, states that, in order to reproduce an analog signal, the sampling frequency should be greater than twice the bandwidth of the signal. Lower sampling rates result in incomplete reconstruction of the sampled signal.

[3]The standard CAN frame length is equal to $47 + 8N$ bits for N data bytes (up to 8 bytes)

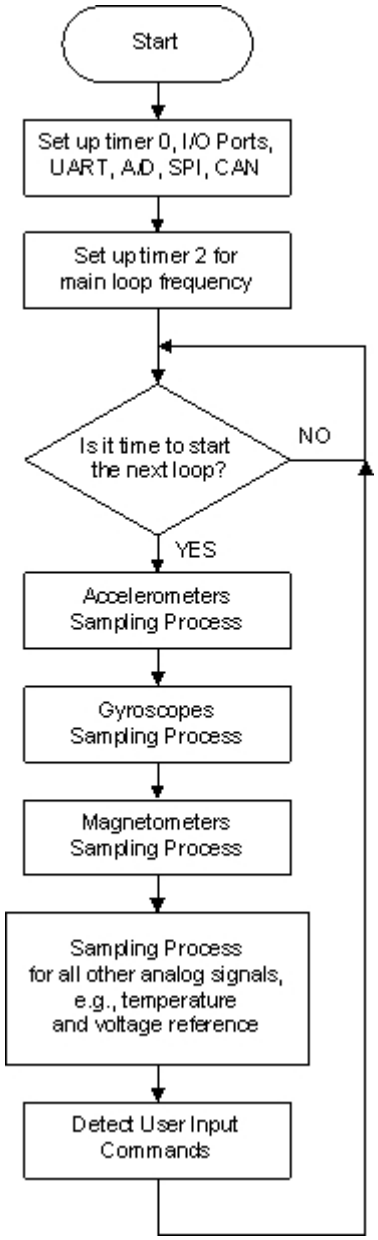

Figure 3.9. Basic navigation card software flowchart.

With a bit rate of 500 kbps, the frame rate is equal to 5747 frames/s. Currently, the baud rate between the microcontroller on the data collection card and its associated USB interface is 57600 bps. The configured sampling frequency for each signal is shown in Table 3.5.

After formatted into the NMEA strings (see Section 3.3.3), the length is 52 bytes for accelerometer measurements, 34 bytes for rate gyroscope measurements, and

Table 3.5. Analog signal sampling frequency configuration.

	Accelerometers	Gyroscopes	Magnetometers	Others
Sampling rate (Hz)	100/3	200/3	200/3	1

34 bytes for magnetometer measurements. At a result, the required transfer rate is about 50134 bps. Thus, both CAN bus and USB can satisfy the transfer rate of the navigation data.

The sampling process of each signal starts at the pre-configured sampling frequency by comparing the time stamps based on the main loop frequency. The flowchart of gyroscope sampling process is demonstrated in Figure 3.10. Other sampling processes run in a similar way.

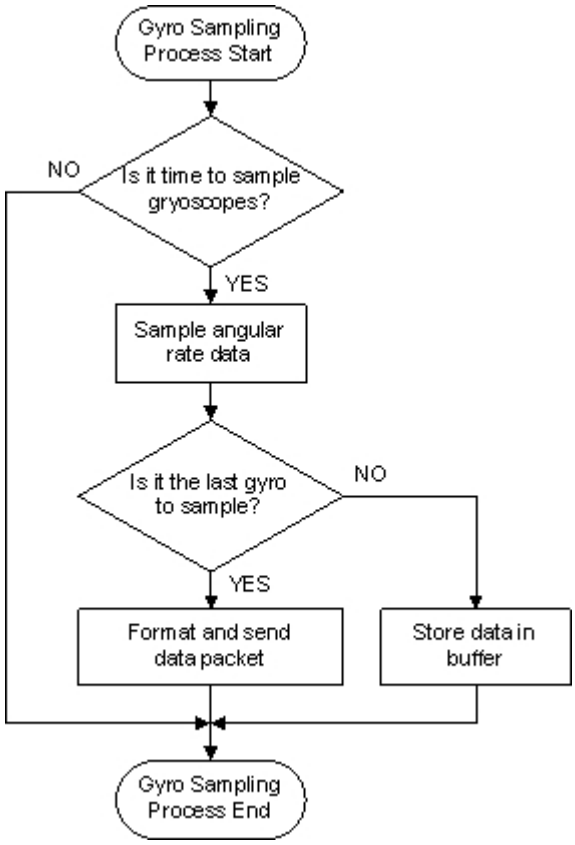

Figure 3.10. Flowchart of gyroscope sampling process.

CHAPTER 4

SENSOR CALIBRATION

The implemented sensing components are susceptible to many errors caused, for example, by sensor axis misalignment, bias and scale factor drift, and external disturbances. These errors are of great concern during the navigation process. In order to obtain correct navigation information, sensor calibration is required. In this chapter, the error model of each sensor is analyzed and the calibration routines are discussed. Some calibration results are illustrated at the end of each section to demonstrate the effectiveness of the calibration techniques. The calibration method is accomplished by hand without the aid of specialized equipment.

4.1 Common Errors

Errors corrupt the navigation solution. Most of the error sources are from sensor errors and random disturbances. There are a few errors common to all types of MARG sensors, which are the focus of the calibration routines.

Bias Error — A bias can be simply defined as the output signal of a sensor when there is no input to the sensor. It is independent of the input but

dependent on temperature. The significance of variation of a bias over temperature is different for each individual sensor. For example, the ADXL203 accelerometers have comparatively high immunity to temperature drift. The temperature coefficient of bias is approximately 0.1 mg/°C (see Table 3.2), whereas the coefficient for the ADXL320 accelerometers of the same type is more than 0.5 mg/°C [23]. Considering that the temperature drift of the sensing components inside the towfish from turn-on to normal operating is about 10 – 20°C , the bias error of ADXL203 can be modelled as a constant. However, a bias may vary from turn-on to turn-on. The initial alignment process dealing with turn-on bias is discussed in Chapter 5. Comparatively, the bias error of low-grade gyroscopes is of more concern. The bias of a gyroscope is often modelled as a first-order Gauss-Markov process [7].

Scale Factor Error — Scale factor is also called sensitivity, which interprets a voltage output of a sensor into a magnitude of the observed field. When the same types of sensors are subject to an identical field, the consequent output from each may not be the same owing to scale factor error. The scale factor is also affected by temperature drift. For example, the scale factor variation of ADXL203 over the whole operating temperature range from −55°C to 125°C is about 0.3% (see Table 3.2).

Misalignment — Ideally, a triad of sensors is constructed orthogonally, and the defined coordinate frame is aligned with the Cartesian coordinate of the body frame. However, in reality, manufacturing and assembly errors result in considerable sensor axis misalignment. Misalignments cause cross-coupling between the measurements of each axis in a triad. Because sensor axis misalignment does not change from turn-on to turn-on[1], the misalignment calibration procedure needs only to be performed once.

[1]The constancy of sensor axis misalignment is under the assumption that the sensors are rigidly mounted and their relative position is not affected by the external forces, such as vibration.

4.2 Accelerometers

Accelerometers measure the absolute acceleration with respect to an inertial frame. Theoretically, the Earth's rotational effects are within the scope of accelerometers, and may affect the acceleration measurements. Among them, the Coriolis effect[2] is of most concern. Applying to the inertial frame defined with the origin at the centre of mass of the Earth, the total acceleration caused by the specific force impacting on an accelerometer triad can be formulated as [34]

$$\mathbf{a}_{\text{acc}} = \mathbf{a}^b - \mathbf{g}^b + 2(\boldsymbol{\omega}_e + \boldsymbol{\omega}_i) \times \mathbf{v} \tag{4.1}$$

where $\boldsymbol{\omega}_e$ is the angular rate vector of the Earth with respect to the inertial frame, $\boldsymbol{\omega}_i$ is the angular rate vector of the vehicle with respect to the inertial frame, and $\mathbf{v}$ is the translational velocity vector relative to the Earth frame. The addition of the two angular velocity vectors, $\boldsymbol{\omega}_e$ and $\boldsymbol{\omega}_i$, results in the rotation of the body frame with respect to the Earth frame, and its cross product with the velocity vector $\mathbf{v}$ generate the Coriolis effects [34]. According to the properties of the cross product operation, the acceleration force caused by the Coriolis effect is always perpendicular to the velocity vector $\mathbf{v}$. Because the accelerometers utilize differential capacitance to measure only the acceleration along the sensing axis [23], the Coriolis effect is negligible. Consequently, the model of an accelerometer triad relative to the body frame can be expressed as[3]

$$\mathbf{V}_{\text{acc}} = \mathbf{s}_{\text{acc}}\,\mathbf{P}\,\mathbf{T}\,(\mathbf{a}^b - \mathbf{g}^b) + \mathbf{b}_{\text{acc}} + \mathbf{w}_{\text{acc}} \tag{4.2}$$

where $\mathbf{T}$ is the direction cosine matrix for transformations from the body frame to an orthogonal sensor frame, $\mathbf{P}$, named the nonorthogonality correction matrix, is for adjusting the nonorthogonal realistic sensor frame into the orthogonal sensor frame, and $\mathbf{w}_{\text{acc}}$ represents the measurement noise vector of the accelerometers. The noise vector is assumed to have zero mean Gaussian components.

[2]The Coriolis effect is caused by relative movements of an object respect to the constantly rotating Earth, whereas centrifugal force is caused by the rotation of the Earth regardless of the dynamic status of the object. Commonly, centrifugal force is considered as part of the Earth's gravity [33].

[3]Through this study, the gravitational vector is given as the action force instead of the reaction force of the accelerometers. Therefore, the sign in front of the gravitational vector is negative.

During initial calibration, the sensing units are moved slowly to minimize the translational acceleration impacted on the sensors. Assuming that the moderate movements of the sensing units during calibration have negligible influence on the measurements, $\mathbf{a}^b$ can be ignored, and the output model for calibration is

$$\mathbf{V}_{\text{acc}} = -\mathbf{s}_{\text{acc}}\,\mathbf{P}\,\mathbf{T}\,\mathbf{g}^b + \mathbf{b}_{\text{acc}} + \mathbf{w}_{\text{acc}} \tag{4.3}$$

The vector $\mathbf{g}^b$ is the gravitational acceleration relative to the body frame and can be interpreted by transforming the true gravity vector $\mathbf{g}$ with respect to the tangent plane using a direction cosine matrix symbolized as $\mathbf{R}_{t2b}$

$$\mathbf{g}^b = \mathbf{R}_{t2b}\,\mathbf{g} \tag{4.4}$$

4.2.1 Bias Calibration

The accelerometers are constantly subjected to the Earth's gravitational field. Although the gravity is location dependent, it is constant within a small range [35], especially during initial calibration. Each accelerometer can be calibrated individually by placing it according to the sensing axis in a vertical position to measure in one direction and then turning it over to measure in the other direction. According to Equation 4.3, the measured values $\mathrm{V}_{\text{acc}}^{\text{up}}$ and $\mathrm{V}_{\text{acc}}^{\text{down}}$ of the i^{th} accelerometer can be used to calculate the initial bias by

$$(\mathrm{b}_{\text{acc}})_i = \frac{(\mathrm{V}_{\text{acc}}^{\text{up}})_i + (\mathrm{V}_{\text{acc}}^{\text{down}})_i}{2} \tag{4.5}$$

From Equation 4.3, it can be seen that the scale factor is correlated to the nonorthogonality correction matrix $\mathbf{P}$. However, a simple method for the scale factor calibration using the same measurements can be performed using

$$(\mathrm{s}_{\text{acc}})_i = \frac{(\mathrm{V}_{\text{acc}}^{\text{up}})_i - (\mathrm{V}_{\text{acc}}^{\text{down}})_i}{2} \tag{4.6}$$

which ignores the nonorthogonality of the accelerometers and assumes that both the acceleration measurements are achieved with the sensing axis aligned with the Earth's gravity vector. A nonlinear least squares calibration algorithm considering

both the nonorthogonality correction and the scale factor error is discussed in the following subsection.

4.2.2 Misalignment and Scale Factor Calibration

Practically, the sensing axes of the accelerometers are not perfectly aligned with the body frame coordinates. Thus, the misalignment calibration is essential for providing accurate acceleration measurements of the towfish. The essential part of misalignment calibration is called nonorthogonality correction, which fixes the sensing axes of accelerometers into an orthogonal triad. Moveover, an orthogonal rotation matrix is required to transform this fixed orthogonal triad to the body frame. In this part of the section, a nonlinear least squares algorithm is introduced for estimating the nonorthogonality correction parameters and the scale factors.

To begin with, the accelerometer observation model (Equation 4.3) can be used to solve $\mathbf{g}$. The yielded equation is

$$\mathbf{g} = -\mathbf{R}_{t2b}^{-1}\,\mathbf{T}^{-1}\,\mathbf{P}^{-1}\,\mathbf{s}_{\text{acc}}^{-1}\,(\mathbf{V}_{\text{acc}} - \mathbf{b}_{\text{acc}} - \mathbf{w}_{\text{acc}}) \tag{4.7}$$

The inner product of $\mathbf{g}$ is equal to

$$\begin{aligned}
\mathbf{g}^T\mathbf{g} &= (\mathbf{R}_{t2b}^{-1}\,\mathbf{T}^{-1}\,\mathbf{P}^{-1}\,\mathbf{s}_{\text{acc}}^{-1}\,(\mathbf{V}_{\text{acc}} - \mathbf{b}_{\text{acc}} - \mathbf{w}_{\text{acc}}))^T(\mathbf{R}_{t2b}^{-1}\,\mathbf{T}^{-1}\,\mathbf{P}^{-1}\,\mathbf{s}_{\text{acc}}^{-1}(\mathbf{V}_{\text{acc}} - \mathbf{b}_{\text{acc}} - \mathbf{w}_{\text{acc}})) \\
&= (\mathbf{V}_{\text{acc}} - \mathbf{b}_{\text{acc}})^T\,\mathbf{s}_{\text{acc}}^{-T}\mathbf{P}^{-T}\mathbf{P}^{-1}\mathbf{s}_{\text{acc}}^{-1}(\mathbf{V}_{\text{acc}} - \mathbf{b}_{\text{acc}}) \\
&\quad -(\mathbf{V}_{\text{acc}} - \mathbf{b}_{\text{acc}})^T\,\mathbf{s}_{\text{acc}}^{-T}\,\mathbf{P}^{-T}\,\mathbf{P}^{-1}\,\mathbf{s}_{\text{acc}}^{-1}\,\mathbf{w}_{\text{acc}}^T \\
&\quad -\mathbf{w}_{\text{acc}}^T\,\mathbf{s}_{\text{acc}}^{-T}\,\mathbf{P}^{-T}\,\mathbf{P}^{-1}\,\mathbf{s}_{\text{acc}}^{-1}(\mathbf{V}_{\text{acc}} - \mathbf{b}_{\text{acc}}) \\
&\quad +\mathbf{w}_{\text{acc}}^T\,\mathbf{s}_{\text{acc}}^{-T}\,\mathbf{P}^{-T}\mathbf{P}^{-1}\mathbf{s}_{\text{acc}}^{-1}\,\mathbf{w}_{\text{acc}}
\end{aligned} \tag{4.8}$$

Note that the orthogonality characteristic of the direction cosine matrices $\mathbf{T}$ and $\mathbf{R}_{t2b}$ is implemented to simplify the equation. By taking the expected value, the following is obtained:

$$\text{E}[\mathbf{g}^T\mathbf{g}] = \text{E}[(\mathbf{V}_{\text{acc}} - \mathbf{b}_{\text{acc}})^T\,\mathbf{s}_{\text{acc}}^{-T}\,\mathbf{P}^{-T}\,\mathbf{P}^{-1}\,\mathbf{s}_{\text{acc}}^{-1}\,(\mathbf{V}_{\text{acc}} - \mathbf{b}_{\text{acc}})] + \text{const} \tag{4.9}$$

Since the gravity vector in the tangent plane is simply a pointing-down unit vector multiplying the gravitational constant g, the following equation can be constructed

as the cost function to be minimized over the specified elements for the nonlinear least squares estimation[4]:

$$\mathrm{C} = \sum_{i=1}^{N} (\sqrt{(\mathbf{V}_{\mathrm{acc}} - \mathbf{b}_{\mathrm{acc}})^T \, \mathbf{s}_{\mathrm{acc}}^{-T} \, \mathbf{P}^{-T} \, \mathbf{P}^{-1} \, \mathbf{s}_{\mathrm{acc}}^{-1} \, (\mathbf{V}_{\mathrm{acc}} - \mathbf{b}_{\mathrm{acc}})} - \mathrm{g})^2 \tag{4.10}$$

Assuming the bias of each accelerometer has been calibrated using the method mentioned above, the nonorthogonality correction matrix $\mathbf{P}$ and/or the scale factor $\mathbf{s}_{\mathrm{acc}}$ can be chosen as the elements to be estimated. The correction matrix is 3×3 and $\mathbf{s}_{\mathrm{acc}}$ is a diagonal matrix with the scale factor of each sensor as the diagonal entries. Therefore, nominally, including the scale factor of each accelerometer, there are twelve unknown parameters when the correction matrix $\mathbf{P}$ is configured as

$$\mathbf{P} = \begin{bmatrix} \mathrm{P}_{11} & \mathrm{P}_{12} & \mathrm{P}_{13} \\ \mathrm{P}_{21} & \mathrm{P}_{22} & \mathrm{P}_{23} \\ \mathrm{P}_{31} & \mathrm{P}_{32} & \mathrm{P}_{33} \end{bmatrix}$$

when one sensing axis is constrained and only the other two are adjusted, the correction matrix can be simplified to a lower triangular matrix:

$$\mathbf{P} = \begin{bmatrix} \mathrm{P}_{11} & 0 & 0 \\ \mathrm{P}_{21} & \mathrm{P}_{22} & 0 \\ \mathrm{P}_{31} & \mathrm{P}_{32} & \mathrm{P}_{33} \end{bmatrix}$$

The estimation parameters can be further reduced to six by using the alignment angles, α, β, and γ shown in Figure 4.1. The selection of the coaxis between the sensor frame and the calibrated orthogonal triad is arbitrary, and the x axis is used as the coaxis in formulation and illustration. The angle-based nonorthogonality correction matrix can be constructed as [36]

$$\mathbf{P} = \begin{bmatrix} 1 & 0 & 0 \\ \cos\alpha & \sin\alpha & 0 \\ \cos\gamma & \cos\beta & \sqrt{1 - \cos^2\beta - \cos^2\gamma} \end{bmatrix}$$

[4]The Matlab function *lsqnonlin* was used to fulfill the estimation procedure.

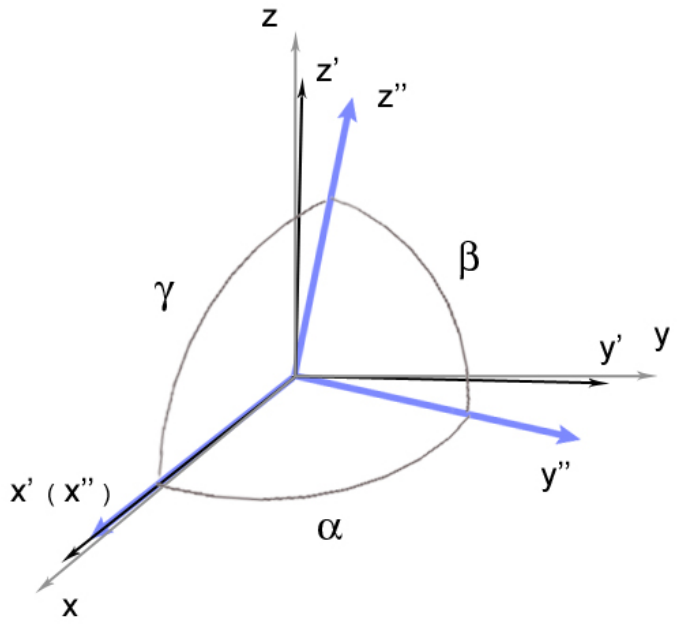

Figure 4.1. Illustration of the nonorthogonality correction using the alignment angles.

Since the nonorthogonality correction only adjusts the sensing axes into an orthogonal triad (see Figure 4.1), the calibration of the transformation matrix $\mathbf{T}$ is required for transformation from this triad to the body frame. For calculating the transformation matrix, the towfish sits still aligned with the tangent plane, and the outputs of the accelerometers are measured. According to the accelerometer model (see Equation 4.3), the following occurs:

$$\mathbf{T}\,\mathbf{g}^b = -\mathbf{P}^{-1}\,\mathbf{s}_{\text{acc}}^{-1}\,(\mathbf{V}_{\text{acc}} - \mathbf{b}_{\text{acc}}) \tag{4.11}$$

Since the towfish is stationary aligned with the tangent coordinate, the gravitational component of the body frame, $\mathbf{g}^b$, is equal to the Earth's gravity vector $\mathbf{g}$. The left side of this equation can be extended further using the DCM formulation consisting of Euler angles.

$$\mathbf{T}\,\mathbf{g} = \begin{bmatrix} \cos\phi_z\cos\phi_y & \sin\phi_z\cos\phi_y & -\sin\phi_y \\ -\sin\phi_z\cos\phi_x + \cos\phi_z\sin\phi_y\sin\phi_x & \cos\phi_z\cos\phi_x + \sin\phi_z\sin\phi_y\sin\phi_x & \cos\phi_y\sin\phi_x \\ \sin\phi_z\sin\phi_x + \cos\phi_z\sin\phi_y\cos\phi_x & -\cos\phi_z\sin\phi_x + \sin\phi_z\sin\phi_y\cos\phi_x & \cos\phi_y\cos\phi_x \end{bmatrix} \begin{bmatrix} 0 \\ 0 \\ \mathrm{g} \end{bmatrix}$$

$$= \begin{bmatrix} -\mathrm{g}\sin\phi_y \\ \mathrm{g}\cos\phi_y \sin\phi_x \\ \mathrm{g}\cos\phi_y \cos\phi_x \end{bmatrix} \tag{4.12}$$

It can be seen that only pitch and roll misaligned angles, ϕ_x and ϕ_y, can be compensated using Equation 4.11. Consequently, by assuming the yaw angle equals to zero, the simplified transformation matrix can be expressed as:

$$\mathbf{T} = \begin{bmatrix} \cos\phi_y & 0 & -\sin\phi_y \\ \sin\phi_y \sin\phi_x & \cos\phi_x & \cos\phi_y \sin\phi_x \\ \sin\phi_y \cos\phi_x & -\sin\phi_x & \cos\phi_y \cos\phi_x \end{bmatrix} \tag{4.13}$$

4.2.3 Experimental Results

The accelerometer calibration experiments were performed according to the algorithm and procedures described above. The bias for each accelerometer has been calibrated several times. The measurements were averaged and the comparison of the calculated bias of each calibration shows that the variation of turn-on bias is quite insignificant. The result for accelerometer bias calibration is listed in Table 4.1 and expressed by the equivalent offset for a 16-bit binary analog-to-digital convertor:

Table 4.1. Experimental results for accelerometer bias calibration expressed using the digital output of the 16-bit analog-to-digital convertor in decimal format.

Accelerometer	Test 1	Test 2	Test 3
x-axis	32296.5	32296.5	32293.5
y-axis	32734.5	32736.5	32726.5
z-axis	32300	32300.5	32297.5

The nonorthogonality correction matrix constructed by three alignment angles was adopted for misalignment calibration. Thus, there are six elements for the nonlinear least squares algorithm including the scale factor of each accelerometer. In Table 4.2, the estimation result is shown. Because the x-axis and y-axis acceleration measurements are provided by a dual-axis accelerometer, the alignment angle between these two axes, α, should be comparably small and expected to

match the manufacturer-defined axes alignment error, $\pm 0.1°$(see Table 3.2). As can be seen, the calibrated alignment angle α is 89.9117° and the alignment error is only 0.0883°, which proves the satisfaction of the nonorthogonality correction algorithm.

Table 4.2. Experimental result of scale factor and aligned angles for accelerometers.

Scale factor (V/g)			Aligned angles		
x-axis	y-axis	z-axis	α	β	γ
0.9854	0.9864	0.9951	89.9117°	91.1850°	88.8985°

The original measurements and the data after nonorthogonality correction are illustrated in comparison in Figure 4.2. The transformation matrix **T** is computed

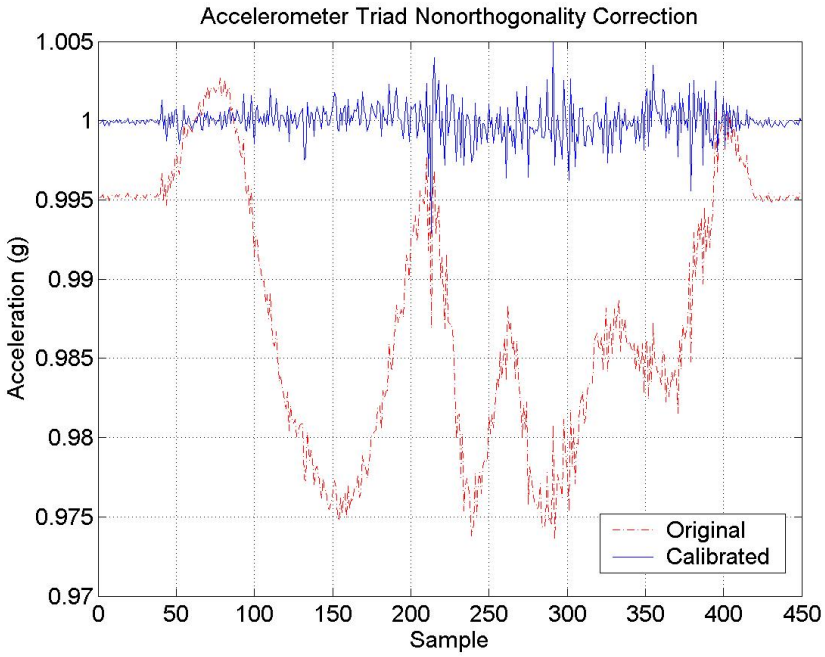

Figure 4.2. Comparison between the original and nonorthogonality corrected total gravitational acceleration.

using the stationary measurements of the accelerometer triad obtained when the body frame of the towfish is aligned with the tangent plane coordinate. The

calibrated result of the transformation matrix is

$$\mathbf{T} = \begin{bmatrix} 1 & 0 & 0.0094 \\ 0.0002 & 0.9998 & -0.0180 \\ -0.0094 & 0.0180 & 0.9998 \end{bmatrix}$$

The diagram in Figure 4.3 shows the comparison between the original and calibrated y-axis accelerometer measurements, and demonstrates the effectiveness of the accelerometer calibration algorithm.

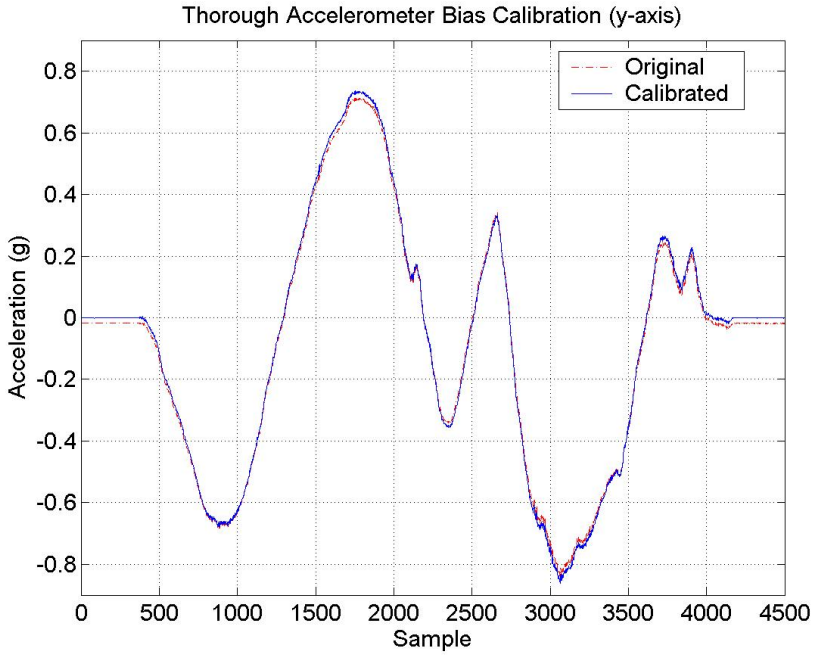

Figure 4.3. Comparison before and after the thorough bias calibration.

4.3 Magnetometers

Magnetometers are sensitive to any nearby objects that have magnetic properties including the Earth. The magnetic fields generated by the objects except the Earth are considered as disturbances for the Earth's magnetic navigation applications. With no magnetic disturbance, a magnetometer triad is able to provide the Earth's magnetic heading of a levelled platform referenced to the tangent plane. If

the declination angle[5] of the Earth's local magnetic field is known, the true heading can be achieved. This certainly provides valuable information for underwater navigation without the assistance of position sensors. However, errors such as bias error and misalignment exist in the magnetic sensors. In addition, the nearby magnetic disturbances disrupt the heading measurements. The calibration methods to compensate these errors are presented in this section.

4.3.1 Temperature Effects and Magnetic Disturbances

The effects of temperature on magnetometers can be classified into two categories, scale factor deviation and bias drift with temperature [24]. As listed in Table 3.3, the scale factor and null field temperature coefficients indicate how these two parameters change with temperature. Since bearing estimation uses the ratio of two orthogonal magnetometers (see Equation 5.6), the temperature dependence of the scale factor can be neglected. In comparison, bias drift with temperature affects the heading accuracy more. The temperature compensation algorithm for the bias is discussed in Section 4.3.2.

Another consideration for sensing accuracy is the effects of nearby magnetic materials on the Earth's magnetic field. Ideally, when a magnetometer triad is rotated in a full circle horizontally, the output plot of the x and y axes is a perfect circle centred at the the origin as illustrated in Figure 4.4 and the measurement of the z axis keeps constant. Practically, the effects of the magnetic disturbances distort the circle. Magnetic disturbances can be divided into two types according to their related characteristics [37].

Hard Iron Disturbance — This kind of interference is caused by nearby magnetized materials such as the electronics and circuit boards. The magnetic vector generated by these magnetic disturbances has constant magnitude and fixed direction with respect to the magnetometers. The magnetized materials could be attached to the magnetometers inside the towfish; alternatively, the disturbance may constantly affect the magnetic field surrounding the

[5]The angle between the true north and the magnetic north. The positive declination angle points to the east. For example, the declination angle in Lyttelton Harbour is approximately 23.4°.

towfish but be some distance from the sensors. Generally, while the towfish is running underwater, the magnetized materials attached to the sensing platform have more impact on the magnetic measurements. The disturbance constantly appends magnetic components to the all the magnetic sensing axes. This effect appears in the 2D plot as a shift of the circle's centre (see Figure 4.4).

Soft Iron Disturbance — This kind of interference is caused by nearby ferrous materials or variable magnetic fields, for example, the surrounding ferrous rocks while the towfish is moving and the altering electromagnetic interference (EMI) of the nearby electronics. The distinction between the hard iron and soft iron disturbances is that the magnetic vector generated by the soft iron disturbance has inconstant magnitude and direction with respect to the magnetometers. Hence, it deforms the circle as shown in Figure 4.4. Because of the variability and weakness of the soft iron disturbance, the effect on the magnetometers is often insignificant.

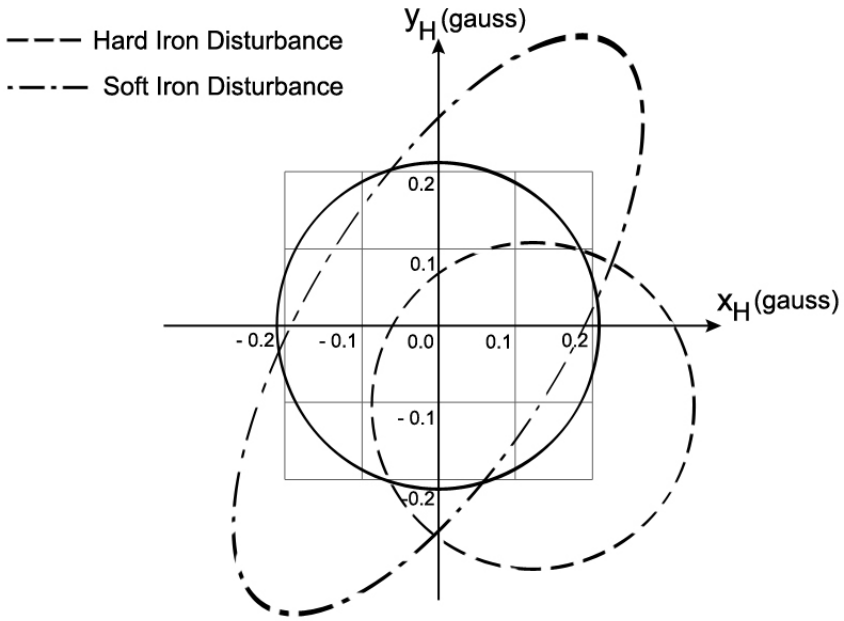

Figure 4.4. Locus of the x and y axis measurements of a horizontally rotated magnetometer triad including hard and soft iron disturbances [37].

4.3.2 Bias Calibration

The bias is the output magnitude of a magnetic sensor subject to a zero magnetic environment. The bias can be determined by taking a measurement inside a magnetically shielded region [38]. For this work, because the implemented magnetic hybrid HMC2003 is equipped with the Set/Reset strap for orientating the magnetic sensing direction (see Section 3.2.2), no specialized equipment is required; consequently the bias of each magnetic sensor can be calibrated through setting and resetting the sensing orientation.

For the initial calibration purpose, the set/reset algorithm simply flips the sensing orientation of each magnetic sensor to measure the ambient magnetic field at the same spot. Because the position and attitude of the sensors are not changed, the Earth's magnetic field, which constantly covers the magnetic sensors, and hard iron disturbance can be considered to be constant. Only soft iron disturbance may vary with time. Therefore, in order to correctly determine the bias, soft iron disturbance has to be avoided carefully. An open field is ideal for calibrating bias to minimize variation of the ambient magnetic disturbances. Assuming the ambient soft iron disturbance is negligible, the outputs of magnetometers can be sampled while the magnetic sensing orientation is flipped a number of times by sending set/reset commands. The bias can be computed using the bi-directional magnetic field measurements as

$$(\mathrm{b}_{\mathrm{mag}})_i = \frac{(\mathrm{V}^{\mathrm{set}}_{\mathrm{mag}})_i + (\mathrm{V}^{\mathrm{reset}}_{\mathrm{mag}})_i}{2} \tag{4.14}$$

Some measurements obtained from a single magnetic sensor are plotted in Figure 4.5 to illustrate the bias calibration process.

The set/reset algorithm can also be used for compensating the bias drift caused by temperature. The same set/reset procedure is implemented periodically through the whole sampling process, and the bi-directional measurements are applied to Equation 4.14 to track the variation of the bias.

4.3.3 Magnetometer Modelling and Calibration

The calibration of magnetometers can be performed by turning the sensors through a series of known headings, a technique called "swinging". A complete equation modelling the misalignment, hard iron, and soft iron errors can be written as [3]

$$\triangle\psi = A + B\sin(\psi_m) + C\cos(\psi_m) + D\sin(2\psi_m) + E\cos(2\psi_m)$$

where ψ_m is the measured compass heading, A represents the magnetometer misalignment error, $B\sin(\psi_m) + C\cos(\psi_m)$ is a function for the hard iron error, and $D\sin(2\psi_m) + E\cos(2\psi_m)$ is the soft iron error model. The least squares algorithm is used to evaluate the five unknowns using the measurements from the known headings, and the true vehicle heading ψ can be determined by

$$\psi = \psi_m - \triangle\psi$$

This calibration algorithm is only suitable when a dual-axis magnetometer is levelled, whereas for a triaxial magnetic sensing unit this method is not applicable.

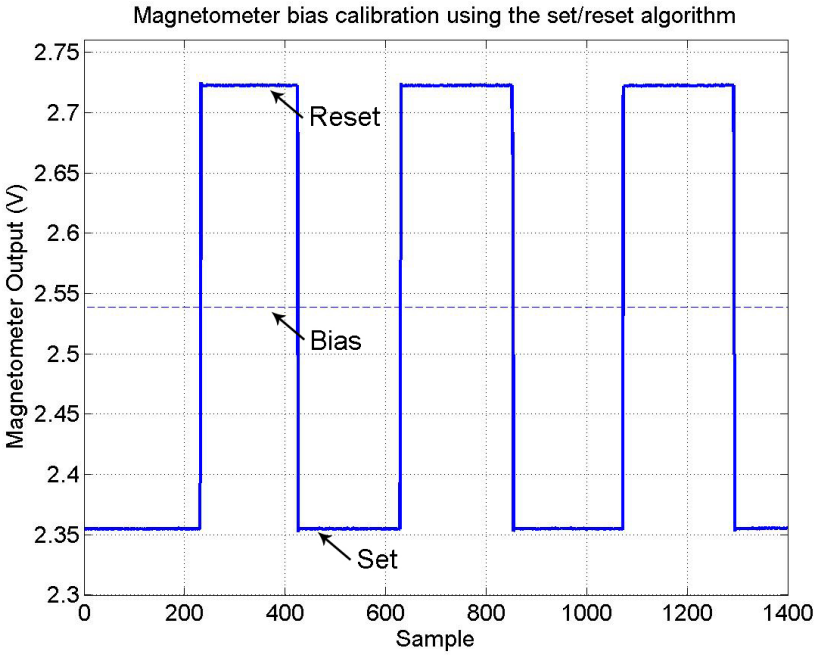

Figure 4.5. Illustration of the bias calibration using the set/reset algorithm.

Obviously, a secondary heading determination system is required for giving the headings for this algorithm. The accuracy of the headings given by the secondary system greatly influences the calibration results.

Similar to the accelerometers, a magnetometer triad system can be mathematically modelled as [39]

$$\mathbf{V}_{\text{mag}} = \mathbf{s}_{\text{mag}}\,\mathbf{P}\,\mathbf{T}\,\mathbf{B}^b + \mathbf{b}_{\text{mag}} + \mathbf{w}_{\text{mag}} \tag{4.15}$$

The difference is that the gravitational acceleration is replaced by the ambient magnetic intensity $\mathbf{B}^b$. The magnetometer bias represented by $\mathbf{b}_{\text{mag}}$ can be determined using the set/reset algorithm. The measurement noise $\mathbf{w}_{\text{mag}}$ is added to the model and assumed to have zero mean Gaussian components.

The magnetic intensity relative to the body frame can also be expressed using the intensity relative to the tangent plane as

$$\mathbf{B}^b = \mathbf{R}_{t2b}\,\mathbf{B}^t = \mathbf{R}_{t2b}\,(\mathbf{B}^t_e + \delta\mathbf{B}^t) \tag{4.16}$$

where $\mathbf{B}^t$ is the total magnetic intensity vector in the tangent plane, $\mathbf{B}^t_e$ is the Earth's nominal magnetic field intensity related to the tangent plane, and $\delta\mathbf{B}^t$ represents the ambient magnetic disturbances. Since the effects of soft iron disturbance on magnetometers is incoherent, and also this type of disturbance has relatively low magnitude especially in an open field or at the sea, soft iron disturbance is often negligible. Thus, $\delta\mathbf{B}^t$ is considered mainly as hard iron disturbance.

Derived using the same algorithm employed for the accelerometers (see Section 4.2.2), the cost function is constructed to minimize over the elements $\mathbf{s}_{\text{mag}}$ and $\mathbf{P}$

$$\mathrm{C} = \sum_{i=1}^{N} (\sqrt{(\mathbf{V}_{\text{mag}} - \mathbf{b}_{\text{mag}})^T\,\mathbf{s}_{\text{mag}}^{-T}\,\mathbf{P}^{-T}\,\mathbf{P}^{-1}\,\mathbf{s}_{\text{mag}}^{-1}\,(\mathbf{V}_{\text{mag}} - \mathbf{b}_{\text{mag}})} - (\mathbf{B}^t_e + \delta\mathbf{B}^t))^2 \tag{4.17}$$

where the correction matrix $\mathbf{P}$ is constructed using three alignment angles as

$$\mathbf{P} = \begin{bmatrix} 1 & 0 & 0 \\ \cos\alpha & \sin\alpha & 0 \\ \cos\gamma & \cos\beta & \sqrt{1-\cos^2\beta-\cos^2\gamma} \end{bmatrix}$$

Since the scale factor is relative to the total magnetic intensity $\mathbf{B}_e^t + \delta\mathbf{B}^t$, in order to determine the absolute scale factor, the intensity term needs to be quantified. Without aid of specialized equipment, one way to obtain the local magnetic intensity is to explore the online magnetic field database available from the National Geophysical Data Center (NGDC) website using global positioning information. The resulting values are computed using the current International Geomagnetic Reference Field (IGRF) and are generally accurate to within 100-250 nT for the magnetic intensity elements [40]. When the intensity term is known, both of the elements $\mathbf{s}_{\text{mag}}$ and $\mathbf{P}$ can be estimated. Alternatively, because of the normality of the angle-based correction matrix $\mathbf{P}$, its determination is independent of the magnetic intensity. Therefore, without losing the generality, the term $\mathbf{B}_e^t + \delta\mathbf{B}^t$ can be replaced by one [39]. It is concluded that

$$\mathrm{C} = \sum_{i=1}^{N} \left(\sqrt{(\mathbf{V}_{\text{mag}} - \mathbf{b}_{\text{mag}})^T \, \mathbf{s}_{\text{mag}}^{-T} \, \mathbf{P}^{-T} \, \mathbf{P}^{-1} \, \mathbf{s}_{\text{mag}}^{-1} \, (\mathbf{V}_{\text{mag}} - \mathbf{b}_{\text{mag}})} - 1\right)^2 \tag{4.18}$$

To minimize this cost function over correction matrix and scale factor elements, $\mathbf{P}$ can be calculated regardless of quantifying the total magnetic field intensity.

4.3.4 Disturbance Compensation

The magnetic disturbances affect the heading accuracy dramatically for both initial calibration and navigation processes. The selected estimator for the disturbance compensation is called the Two-Step Estimator (TSE) [41].

The basic idea of two step estimation is to divide the problem of a nonlinear cost function minimization into two steps, a linear first step and a nonlinear second step. The desired parameters are the states for the second step, and the combinations of the second-step states are chosen as the first-step states so that the first-step estimation is linear. Thus, the linear first-step problem can be solved optimally

using a linear Kalman filter or linear least squares fit. The resulting first-step states are treated as measurements for the second-step problem, and an iterative Gauss-Newton algorithm is used to perform a nonlinear least squares fit. This algorithm avoids the linearized process of recursive nonlinear estimators such as the extended Kalman filter and consequently provides optimal estimates. The study of magnetometer calibration adopting the TSE algorithm is based on a reported research [42].

First, the mathematical model for the nonlinear two-step estimator is derived. According to Equation 4.15 and Equation 4.16, the Earth's magnetic intensity is given by

$$\mathbf{B}_e = \mathbf{B}^t - \delta\mathbf{B} = \mathbf{R}_{b2t}\,\mathbf{T}^{-1}\,\mathbf{P}^{-1}\,\mathbf{s}_{\text{mag}}^{-1}\,(\mathbf{V}_{\text{mag}} - \mathbf{b}_{\text{mag}}) - \delta\mathbf{B} \tag{4.19}$$

Considering the fact that the locus of the Earth's magnetic field measurements of an orthogonal magnetometer triad is a sphere, the following can be obtained:

$$\left(\frac{\mathrm{V}_x}{s_x} - \delta B_x\right)^2 + \left(\frac{\mathrm{V}_y}{s_y} - \delta B_y\right)^2 + \left(\frac{\mathrm{V}_z}{s_z} - \delta B_z\right)^2 = B_e^2 \tag{4.20}$$

where V_x, V_y, and V_z are orthogonally corrected bias-free magnetometer voltage outputs. Note that the transformation matrices $\mathbf{R}_{b2t}$ and $\mathbf{T}$ are neglected, because only the nonorthogonality correction is required to guarantee the orthogonality of the magnetometer triad and satisfy the above equation. Equation 4.20 can be rearranged in matrix format as follows:

$$-(\mathrm{V}_x)^2 = [-2\mathrm{V}_x \quad \mathrm{V}_y^2 \quad -2\mathrm{V}_y \quad \mathrm{V}_z^2 \quad -2\mathrm{V}_z \quad 1] \begin{bmatrix} \widetilde{\delta B}_x \\ k_2 \\ k_2(\widetilde{\delta B}_y) \\ k_3 \\ k_3(\widetilde{\delta B}_z) \\ k_4 \end{bmatrix} \tag{4.21}$$

where

$$\begin{aligned} \widetilde{\delta B}_x &= s_x(\delta B_x) \\ \widetilde{\delta B}_y &= s_y(\delta B_y) \end{aligned}$$

$$
\begin{aligned}
\widetilde{\delta B}_z &= s_z(\delta B_z) \\
k_1 &= s_x^2\, B_e^2 \\
k_2 &= s_x^2 / s_y^2 \\
k_3 &= s_x^2 / s_z^2 \\
k_4 &= \widetilde{\delta B}_x^2 + k_2(\widetilde{\delta B}_y)^2 + k_3(\widetilde{\delta B}_z)^2 - k_1
\end{aligned}
$$

In the two-step estimation, $[\widetilde{\delta B}_x, k_2, k_2(\widetilde{\delta B}_y), k_3, k_3(\widetilde{\delta B}_z), k_4]^T$ is defined as the states for the linear first step. By gathering the voltage outputs from the magnetometer triad, a system of equations can be collected, and the first-step states can be solved, for instance, using a linear Kalman filter. The estimated first-step states and their associated error covariances are treated as measurements in the second step, where the hard iron disturbance δB_x, δB_y, and δB_z, as well as the scale factors s_x, s_y, and s_z are used as the states. A nonlinear least squares algorithm such as the Gauss-Newton method can be implemented for the nonlinear second step. For open-field experiments, the first-step states can be assumed to be time independent, and the optimal static solution can be derived because the two steps are decoupled [41].

4.3.5 Experimental Results

A few experiments were performed for magnetometer initial calibration. The set/reset algorithm was used at the beginning of each test to calculate the bias, and the results are listed in Table 4.3.

Table 4.3. Experimental results for magnetometer bias calibration expressed using the digital output of the 16-bit analog-to-digital convertor in decimal format.

Accelerometer	Test 1	Test 2	Test 3
x-axis	33551.5	33570	33553
y-axis	33277	33280	33276
z-axis	33204.5	33204	33205.5

The nonorthogonality correction matrix was also calculated. The matrix was constructed using alignment angles, and the computed results of the three align-

ment angles are shown in Table 4.4. Considering that the nonorthogonality correction matrix is independent of the magnetic intensity (see Section 4.3.3), the trial location can be selected arbitrarily if only the ambient magnetic field intensity keeps relatively constant. This experiment was accomplished in a lab at the University of Canterbury. The original total magnetic intensity was computed in comparison with the nonorthogonality corrected total magnetic intensity (see Figure 4.6). It can be seen that, although no precise ambient magnetic intensity was implemented, the nonorthogonality matrix calibrated correction matrix gives an absolute relationship between the orthogonal sensing package frame and the nonorthogonal sensing axes. There is still some vibration of the corrected total magnetic intensity, which is suspected to be magnetic disturbances in the lab.

Table 4.4. Experimental results of alignment angles for magnetometers.

Test	Aligned angles		
	α	β	γ
1	89.70°	85.73°	86.38°
2	88.57°	85.52°	86.24°
3	90.22°	85.92°	86.90°

The data from a sea trial in Lyttelton Harbour (Christchurch, New Zealand) was used for the simulation of the magnetic disturbance compensation. According to the magnetic field data from the National Geophysical Data Center (NGDC) [40], the total Earth's magnetic intensity is about 0.579 gauss. The linear least squares algorithm and Gauss-Newton method were implemented for the two step estimation. A thoroughly calibrated magnetic data is illustrated in Figure 4.4 in comparison with the original data, and the scale factors are also calculated from the two-step estimator as shown in Table 4.5.

Table 4.5. The calibrated magnetometer scale factors.

	Magnetometers		
	x	y	z
Scale Factor	1.0682	1.0987	1.1408

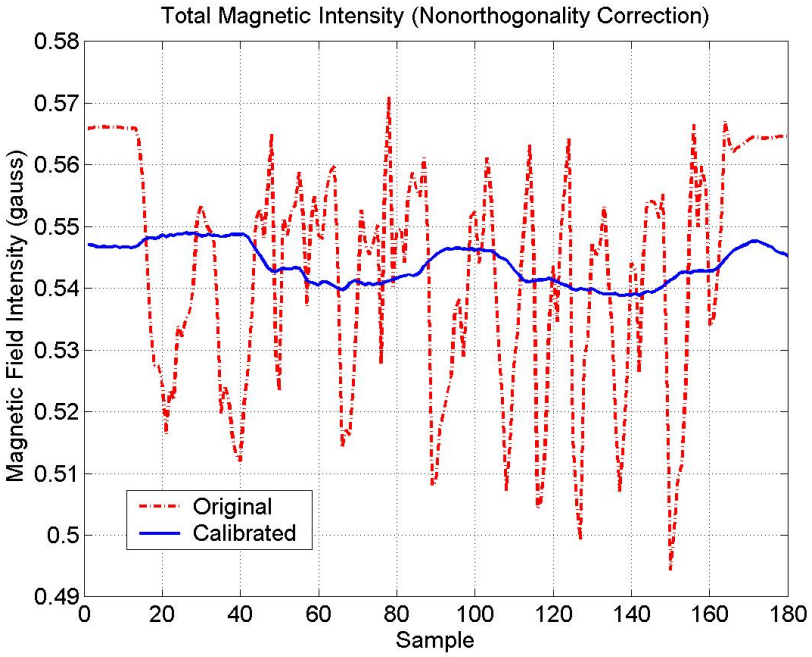

Figure 4.6. Comparison between the original and nonorthogonality corrected total magnetic intensity.

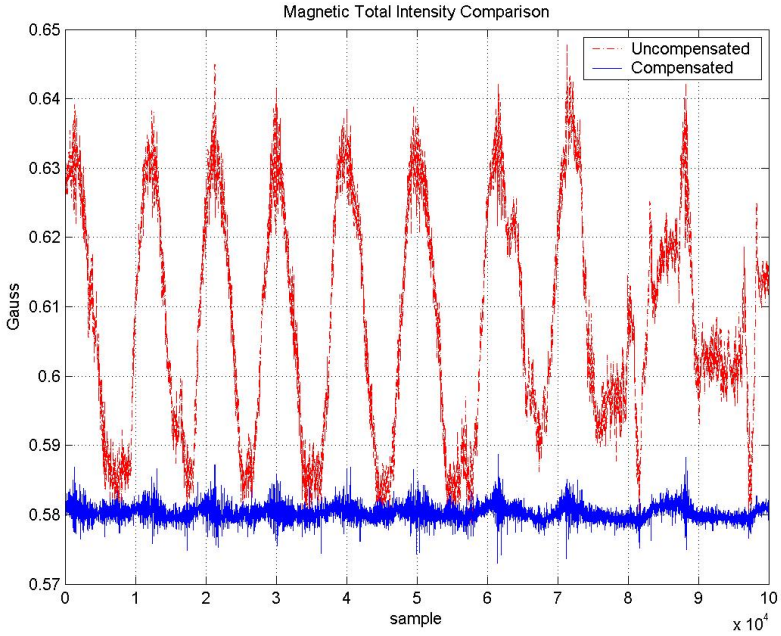

Figure 4.7. The total Earth's magnetic intensity comparison before and after compensation.

4.4 Rate Gyroscopes

The rate gyroscopes are the essential elements for this dead reckoning system. These sensors provide output signals proportional to rotation rates used to monitor the orientation of the towfish. However, these output signals are contaminated by errors such as noise, bias drift, and scale factor error. In this section, the error model of the rate gyroscopes is studied, and the initial calibration algorithms are discussed in detail.

4.4.1 Bias Error

Ideally, the gyro bias is considered as a random constant and can be determined using the observed output signals while a gyroscope is stationary and horizontally aligned. Theoretically, a gyro is able to detect any rotation around the sensing axis including the Earth's rotation rate. The technique implementing gyros to sense the Earth's rotation for heading calibration is known as gyrocompassing [43]. However, for low performance gyroscopes, the effect of the Earth's rotation is negligible. Since the Earth's rotation rate is about $0.004\,^{\circ}/\mathrm{s}$, for instance, for the ADXRS401 gyroscopes, the rotation of the Earth results in an output signal of approximately $60\,\mu\mathrm{V}$, which is well below the noise floor for this kind of gyroscopes[6].

Strictly speaking, the gyro bias is not constant over time. The actual bias can be categorized to two components. One component is identified as non-deterministic output errors, and the other are errors caused by external factors such as temperature variation [44]. The non-deterministic error can be modelled as a stochastic constant. Hence, the one of most concern is the output error caused by external factors. One of the obvious external factors affecting the gyro bias is temperature variation. One way to calibrate the temperature sensitivity of the bias is to place a gyro in a temperature chamber and monitor its output [44]. For this work, the sensor units were kept in the laboratory over night and day. Since each ADXRS401 rate gyro has an integrated temperature sensor inside the sensor packaging, each gyro and the associated internal temperature were precisely measured. The desire is to imitate a wide range of temperature variance and construct a lookup table

[6]With the bandwidth configured as 10 Hz, the noise floor of the ADXRS401 gyroscopes is about 1.5 mV.

of the bias over the temperature range for future compensation. A static test was performed on the Analog Devices ADXRS401 rate gyros and the voltage output of one rate gyro is shown in Figure 4.8.

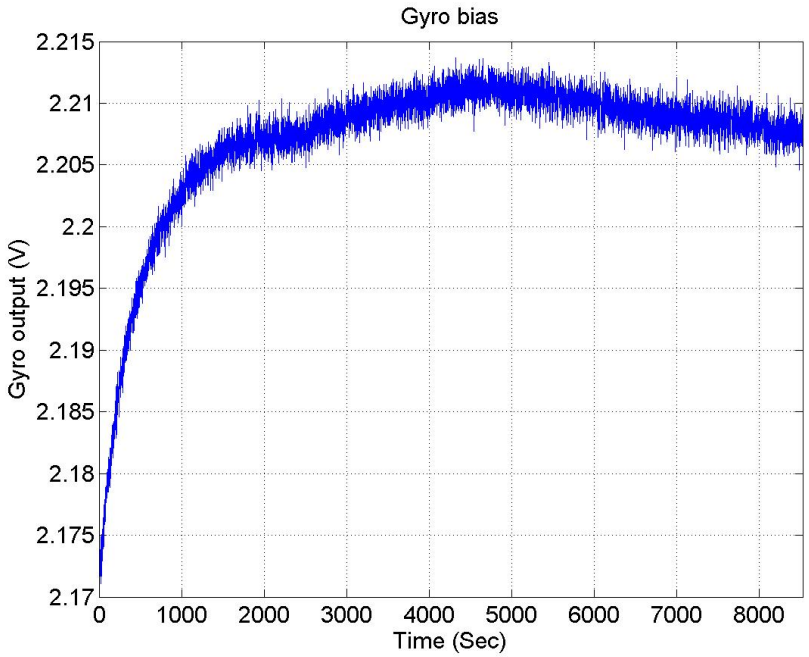

Figure 4.8. Gyroscope voltage output for bias determination.

The implementation of the bias lookup table over temperature provides a solution for temperature compensation during postprocessing. However, it increases time consumption and computational demand. Also, this algorithm considers the bias drift is only caused by temperature variation, and other external factors are neglected.

Another technique for compensating the bias is to construct a error model. The bias of a rate gyro can be considered to be a stochastic process driven by white noise sequences [45]. For a rate gyro, the bias is correlated in time and can be modelled as a first order Gauss-Markov process [16, 45], which can be expressed mathematically as

$$\dot{\mathrm{b}}_{\mathrm{rgy}} = -\frac{1}{\tau}\mathrm{b}_{\mathrm{rgy}} + \mathrm{w}_b \tag{4.22}$$

where $\mathrm{b}_{\mathrm{rgy}}$ is the gyro bias, the constant τ is called the correlation time, and w_b represents the driving process noise.

In order to determine the Gauss-Markov process model for the gyro bias, the correlation time constant τ has to be obtained. By using the static measurements of the ADXRS401 rate gyros, the autocorrelation function was derived[7], and an autocorrelation function plot of one of these gyros is displayed in Figure 4.9. The mean value was removed from the long term angular rate measurements. The autocorrelation function has been normalized so that the magnitude at zero-lag is unity. The correlation time constant for this rate gyro is approximately 350 s determined when the autocorrelation is reduced to the 36.78 percent of the total noise variance.

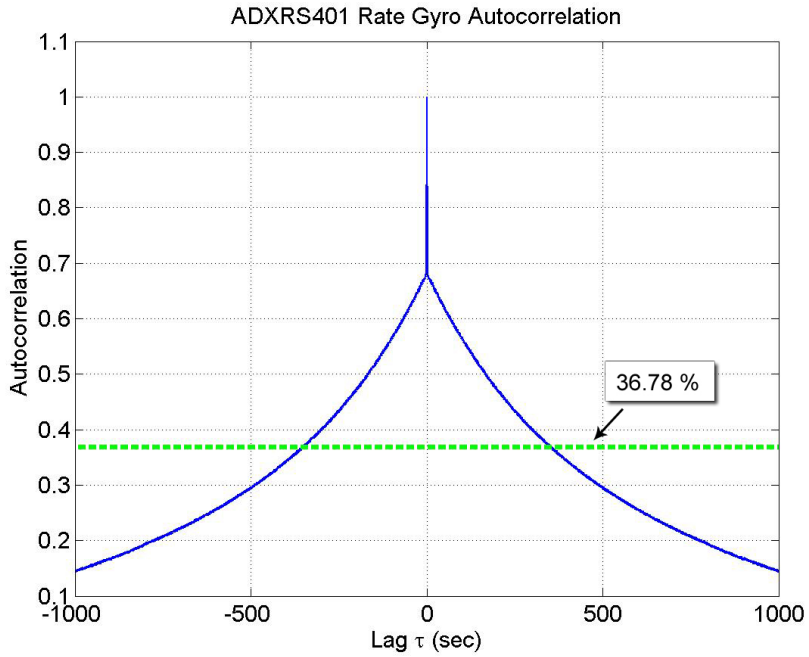

Figure 4.9. Autocorrelation plot for the ADXRS401 rate gyro.

4.4.2 Scale Factor Error

Unlike the gyro bias, the scale factor error has no influence on the stationary measurements of a gyro, whereas the effect of this error only occurs during rotation. According to this characteristic, the gyro scale factor can be observed when the sensing platform takes a turn. Commonly, this is accomplished using specialized

[7]The Matlab function *xcorr* was used to fulfill the autocorrelation calculation.

equipment such as a turn table, which gives precise and configurable rotation rates, and the scale factor can be directly calculated using the desired angular rate and the measured results.

In practice, the calibration of scale factor can also be accomplished but with increased difficulty and reduced accuracy. Considering generally the scale factor of a gyro is constant for both clockwise and anti-clockwise rotations, if a vehicle takes an equal number of clockwise and anti-clockwise rotations around the rate axis of a gyro[8], the heading error due to scale factor tends to be zero [46]. The period of time spent should be minimized so that temperature variation is negligible. The rotated angle calculation using the measured angular rate ω_i can be given mathematically as

$$\theta_i = \int \omega_i + (b_{\text{rgy}})_i + \mathrm{v}_m \, \mathrm{d}t = \int (s_{\text{rgy}})_i \, \mathrm{V}_i + (b_{\text{rgy}})_i + \mathrm{v}_m \, \mathrm{d}t \tag{4.23}$$

where b_{rgy} and s_{rgy} are defined as the gyro bias and scale factor, and v_m is the gyro output noise. Since the rotated angles on the left side of the equation are the same for clockwise and anti-clockwise rotations described above, and the polarity of the output voltage is opposite, the scale factor of this gyro can be computed by subtracting the integration equations for both rotations. However, similar to the gyro bias, the scale factor also changes with temperature. Some studies have also implemented a first order Gauss-Markov process for this error component [16, 45].

[8]The rate axis of a gyro is defined as the axis normal to the sensor package top. A gyro produces a positive output voltage for clockwise rotation about its rate axis.

CHAPTER 5

SENSOR FUSION AND RESULTS

Sensor calibration can only optimize the performance of an individual sensor, whereas even better results can be achieved using the properly chosen combination of sensors according to each characteristic strength and weakness. The hybridization of sensors is known as sensor fusion. In this work, the calibrated MARG sensor data is integrated to provide more accurate estimation through an extended Kalman filter.

The filter is constructed based on quaternions. This rotation parameterization technique avoids singularity and simplifies the rotation and derivative calculations as discussed in Section 2.4. However, in order to integrate the angular rates and translational acceleration data measured from the inertial sensors to achieve position, velocity, and attitude estimation, initial position, initial velocity, and the initial attitude angles of the body frame relative to the tangent plane must be known accurately. This process is known as initial alignment. In Section 5.1, the algorithm used for the initial alignment is described. The details of the quaternion-based extended Kalman filter is presented in Section 5.2, followed by some simulations and experimental results to demonstrate the implementation of the designed

filter.

5.1 Initial Alignment

The accuracy of the navigation estimation is heavily dependent on the initial alignment of the body frame. The initial alignment process includes the determination of the initial position and velocity values and initial attitude angles relative to the tangent plane. According to the dynamics of the body frame with respect to the tangent plane, the initial alignment can be categorized into stationary alignment and in-motion alignment.

5.1.1 Stationary Initial Attitude Alignment

Stationary alignment is performed when the towfish platform is at rest with the result that the velocities and accelerations of the platform can be considered zero. The settled location can be simply set as the origin of the tangent plane for the following navigation proposes. The focus of stationary alignment is specifically on the initial attitude alignment.

The initial attitude alignment determines the rotation matrix between the body frame to the user-defined tangent plane. In principle, the stationary initial attitude alignment can be directly obtained from the measurements of the integrated accelerometers and the magnetic hybrid. Two of the Euler angles, pitch and roll, can be calculated using the accelerometer measurements along the x-axis and y-axis of the towfish coordinate. The magnetic hybrid provides the azimuth information of the towfish platform. However, because of the turn-on bias deviation of the accelerometers and the ambient magnetic disturbances of the magnetic hybrid, the navigation data needs to be compensated first.

As shown in Table 3.2, the initial bias deviation from the ideal value of the ADXL203 accelerometers is $\pm 25\,\mathrm{mg}$, which means the variation of the turn-on bias can be as much as $50\,\mathrm{mg}$. While the towfish platform aligns horizontal along both x and y axis with the tangent plane, the unknown bias can bring approximately 3° alignment error in pitch and roll angles. This acts similar to the gyro bias and introduce an error in velocity and position calculation. In Chapter 4,

a nonlinear least squares routine for the nonorthogonality calibration of the accelerometers has been introduced. Since the nonorthogonality is mainly caused by manufacturing and assembling error, the nonorthogonal parameters only need to be calibrated once. By using the pre-calibrated nonorthogonality information, the turn-on bias can be estimated according to the same technique (see Section 4.2.2). The difference is that the designed parameters of the nonlinear least squares routine change from the nonorthogonality elements to the bias elements. Note that although this is called stationary alignment, in order to achieve better estimation results, multi-position alignment may be required. Because the ADXL203 accelerometers provide high zero g bias stability and high sensitivity accuracy [23], the calibration of scale factor error and temperature drift of the accelerometers can be neglected. According to the coordinate transformation matrix based on Euler angles (see Equation 2.11), the compensated data from the accelerometers is used to establish the following equation:

$$\begin{bmatrix} a_x \\ a_y \\ a_z \end{bmatrix} = \mathbf{R}_{b2t}^{T} \begin{bmatrix} 0 \\ 0 \\ \mathrm{g} \end{bmatrix} \tag{5.1}$$

Consequently, the pitch and roll angles can be calculated as:

$$\theta_x = \arctan\left(\frac{a_y}{a_z}\right) \quad \text{and} \quad \theta_y = -\arcsin\left(\frac{a_x}{\mathrm{g}}\right) \tag{5.2}$$

The magnetic hybrid outputs the ambient magnetic field measurements for all three axes of the towfish body. By using the two-step estimation method (see Section 4.3), the true Earth's magnetic field can be refined. The calibrated Earth's magnetic field measurements relative to the towfish platform can be used for azimuth estimation. In order to result in the correct yaw angle relative to the tangent plane, the Euler angles calculated from the accelerometers are used to transform the magnetic measurements of the body frame to the tangent plane. Equation 2.11 is simplified by neglecting the yaw plane rotation, which means only pitch and roll of the three-step rotation sequence (see Section 2.4.2) are taken. The

modified transformation matrix is

$$\mathbf{R}_{b2t} = \begin{bmatrix} \cos\theta_y & \sin\theta_y \sin\theta_x & \sin\theta_y \cos\theta_x \\ 0 & \cos\theta_x & -\sin\theta_x \\ -\sin\theta_y & \cos\theta_y \sin\theta_x & \cos\theta_y \cos\theta_x \end{bmatrix} \tag{5.3}$$

Assuming that the magnetic component is represented by B with the superscript denoting the related frame and the subscript denoting the specific axis, the tangent magnetic components can be calculated using

$$\begin{aligned} B_x^t &= \cos\theta_y B_x^b + \sin\theta_y \sin\theta_x B_y^b + \sin\theta_y \cos\theta_x B_z^b \\ B_y^t &= \cos\theta_x B_y^b - \sin\theta_x B_z^b \qquad (5.4) \\ B_z^t &= -\sin\theta_y B_x^b + \cos\theta_y \sin\theta_x B_y^b + \cos\theta_y \cos\theta_x B_z^b \qquad (5.5) \end{aligned}$$

The yaw angle is expressed in the ratio of the tangent magnetic components as

$$\theta_z = \arctan\left(\frac{B_x^t}{B_y^t}\right) - \theta_{\text{dec}} \tag{5.6}$$

where θ_{dec} is the location-dependent and time-dependent declination angle of the Earth's magnetic field vector, for instance, 23.381° currently in Lyttelton Harbour. Therefore, the complete initial transformation matrix from the body frame to the tangent plane can be resolved. In order to distinguish from the orientation transformation matrix, $\mathbf{C}_{b2t}$ is used to represent the initial orientation matrix, and can be specified as

$$\mathbf{C}_{b2t} = \mathbf{C}_{t2b}^T = \begin{bmatrix} \cos\theta_z \cos\theta_y & -\sin\theta_z \cos\theta_x + \cos\theta_z \sin\theta_y \sin\theta_x & \sin\theta_z \sin\theta_x + \cos\theta_z \sin\theta_y \cos\theta_x \\ \sin\theta_z \cos\theta_y & \cos\theta_z \cos\theta_x + \sin\theta_z \sin\theta_y \sin\theta_x & -\cos\theta_z \sin\theta_x + \sin\theta_z \sin\theta_y \cos\theta_x \\ -\sin\theta_y & \cos\theta_y \sin\theta_x & \cos\theta_y \cos\theta_x \end{bmatrix} \tag{5.7}$$

5.1.2 In-Motion Initial Alignment

The in-motion alignment is carried out when the towfish is in motion. Since on the open water the towfish can be hardly stationary, in-motion alignment is a practical

and essential alignment technique for the towfish navigation. In this subsection, the scheme implemented for the towfish alignment is presented.

Commonly, in-motion alignment estimation requires external velocity or position sensors [47, 48]. Inside the towfish, a pressure sensor is available to monitor the depth of the towfish. Also, since the tow cable is accurately marked (see Section 2.1), the distance between the towboat and the towfish is known. Therefore, if the position of the towboat is marked as the origin of the tangent plane, the distance relative to the tangent plane can be calculated from the length of the tow cable and the depth of the towfish. Because of the weight of the tow cable and the chain used to depress the towfish, the shape of the tow cable should also be considered for the distance calculation. According to the dynamic characteristics of the towfish, if the towboat drives along a close-to-straight line at a constant speed, ideally the towfish travels without any translational force from the boat[1]. Therefore, in theory, by taking the position of the towboat provided by the GPS unit on board and the distance between the boat and the towfish, the position of the towfish can be estimated.

In Section 5.2, a quaternion-based extended Kalman filter is presented for position, velocity, and attitude estimation. For this work, the position information obtained from the global positioning information of the boat can be directly implemented for determining the start point of the towfish for every run.

5.2 Quaternion-Based Extended Kalman Filter

This section presents a quaternion-based extended Kalman filter that combines the well calibrated measurements of the integrated MARG sensors to produce attitude, velocity, and position estimation in a complementary fashion. Although gyro measurements have been calibrated, there are still considerable errors which grow with time due to integration. The magnetometer triad is used to measure the Earth's magnetic field providing a magnetic heading. This magnetic heading provide the external reference to correct the gyro drift in yaw, and is also stabilized by the gyroscopes. The accelerometer triad provides dynamic and static measurements for detecting the translational acceleration and orientation. The resulting pitch

[1]The effect waves and the vibration of the towfish are neglected.

and roll angles provide a means to resolve the measured magnetic field into the horizontal component (see Equation 5.4) to form a compass heading, and also curb the gyro drift in pitch and roll. The mechanism diagram of the designed Kalman filter is illustrated in Figure 5.1.

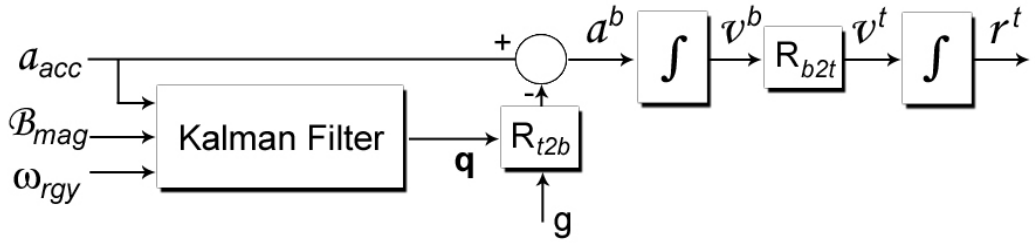

Figure 5.1. The mechanism of the quaternion-based extended Kalman filter.

As shown in Figure 5.1, a direct filtering architecture[2] is used for this quaternion-based extended Kalman filter. Position, velocity and attitude are directly chosen as the state of the navigation model. For the coordinate transformation, quaternions are used rather than Euler angles in order to avoid singularity and improve calculation efficiency. For every sampling of the navigation data, the quaternion representation is updated, and the coordinate transformation matrix between the body frame and the tangent plane can be resolved for decoupling the translational acceleration from the gravitational acceleration.

According to the basics of the Kalman filtering introduced in Section 2.5, a Kalman filter consists of a process model and an observation model to fulfill the predict and correct phases of the recursive filtering. In the following, the process model and observation model of the quaternion-based extended Kalman filter are described in detail.

[2]Direct filtering adopts total state space, compared to the error state space architecture of indirect filter. Direct filtering models position, velocity, and attitude of a navigation system and uses the sensor signals as inputs, whereas an indirect filtering uses system errors as states and requires system errors as inputs [49].

5.2.1 Process Model

The goal of this Kalman filter is to provide position, velocity, and attitude estimation of the towfish. The attitude quaternion, $\mathbf{q}$, the velocity relative to the body frame, $\mathbf{v}^b$, and the position with respect to the tangent plane, $\mathbf{r}^t$, are directly used as the states of the filter. Also, because the gyroscope measurements are corrupted by a bias influenced by temperature and other undetermined factors (see Section 4.4) and correlated with time, the gyro bias, $\mathbf{b}_{\text{rgy}}$, is also chosen as a state of the filter. Therefore, the state vector of the Kalman filter can be expressed as

$$\mathbf{x} = [(\mathbf{q})^T \quad (\mathbf{b}_{\text{rgy}})^T \quad (\mathbf{v}^b)^T \quad (\mathbf{r}^t)^T]^T \tag{5.8}$$

A process model is required to predict the value of each state. It can be seen in Figure 5.1 that the orientation estimate represented by quaternions is of the essence and determines position and velocity in a direct manner. The attitude quaternion provide the coordinate transformation from the body frame to the tangent plane. The propagation of the quaternion state is described using the angular rates of the body frame, $\boldsymbol{\omega}^b$, according to the differential equation:

$$\dot{\mathbf{q}} = \frac{1}{2}\mathbf{q}\boldsymbol{\omega}^b = \frac{1}{2}\boldsymbol{\Psi}\mathbf{q} \tag{5.9}$$

where

$$\boldsymbol{\omega}^b = [\omega_x \quad \omega_y \quad \omega_z]^T$$

and

$$\boldsymbol{\Psi} = \begin{bmatrix} 0 & -\omega_x & -\omega_y & -\omega_z \\ \omega_x & 0 & \omega_z & -\omega_y \\ \omega_y & -\omega_z & 0 & \omega_x \\ \omega_z & \omega_y & -\omega_x & 0 \end{bmatrix}$$

Note that renormalization is required at the end of each iteration for providing a unity quaternion to perform vector rotation. The gyro bias term, $\mathbf{b}_{\text{rgy}}$, and the gyroscope measurement noise term, $\mathbf{w}_{\text{rgy}}$, are subtracted from the raw angular rate measurements, $\boldsymbol{\omega}_{\text{rgy}}$, obtained from the gyroscopes to resolve the bias and noise

corrected angular rates of the body frame:

$$\boldsymbol{\omega}^b = \boldsymbol{\omega}_{\text{rgy}} - \mathbf{b}_{\text{rgy}} - \mathbf{w}_{\text{rgy}} \tag{5.10}$$

The transformation matrix between the tangent plane and the body frame can be written in terms of the four-element quaternion state vector as

$$\mathbf{R}_{t2b} = \mathbf{R}_{b2t}^T = \begin{bmatrix} 1-2q_2^2-2q_3^2 & 2q_1q_2-2q_0q_3 & 2q_1q_3+2q_0q_2 \\ 2q_1q_2+2q_0q_3 & 1-2q_1^2-2q_3^2 & 2q_2q_3-2q_0q_1 \\ 2q_1q_3-2q_0q_2 & 2q_2q_3+2q_0q_1 & 1-2q_1^2-2q_2^2 \end{bmatrix} \tag{5.11}$$

For translational modelling, the velocity with reference to the body frame is chosen. The advantage is that the available velocity information (either direct or indirect), such as the speed data from GPS for the alignment purpose and the accelerometer measurements, is relative to the same frame of reference, and the velocity with reference to the tangent plane can be simply resolved using the transformation matrix given above. The disadvantage is the slightly increased complexity of the Jacobian matrix computation. The velocity differential equation can be described in terms of the total acceleration caused by the specific force (see Equation 4.1) measured by the accelerometer triad, the transformation matrix derived from the quaternion, $\mathbf{R}_{t2b}$, and initial orientation matrix, $\mathbf{C}_{t2b}$.

$$\dot{\mathbf{v}}^b = \mathbf{a}_{\text{acc}} - \mathbf{R}_{t2b}\mathbf{C}_{t2b}\mathbf{g} \tag{5.12}$$

The position of interest is with reference to the tangent plane. The propagation of the position state can be described using the differential equation:

$$\dot{\mathbf{r}}^t = \mathbf{R}_{b2t}\mathbf{C}_{b2t}\mathbf{v}^b \tag{5.13}$$

As discussed in Section 4.4, the gyro bias can be modelled as a first order Gauss-Markov process. Hence, the propagation of the gyro bias, $\mathbf{b}_{\text{rgy}}$, is described mathematically as

$$\dot{\mathbf{b}}_{\text{rgy}} = -\frac{1}{\boldsymbol{\tau}}\mathbf{b}_{\text{rgy}} + \mathbf{w}_b$$

$$= \begin{bmatrix} -\frac{1}{\tau_x} & 0 & 0 \\ 0 & -\frac{1}{\tau_y} & 0 \\ 0 & 0 & -\frac{1}{\tau_z} \end{bmatrix} \mathbf{b}_{\text{rgy}} + \mathbf{w}_b \tag{5.14}$$

where $\mathbf{w}_b$ represents the driving process noise. The correlation time constant ($\tau_x = \tau_y = \tau_z$) for three ADXRS401 gyroscopes was determined as approximately 350 s (see Section 4.4).

Consequently, combing the quaternion differential equation (Equation 5.9), the bias propagation equation (Equation 5.14), and the translational differential equations (Equation 5.12 and 5.13), the state equation can be written as

$$\begin{bmatrix} \dot{\mathbf{q}} \\ \dot{\mathbf{b}}_{\text{rgy}} \\ \dot{\mathbf{v}}^b \\ \dot{\mathbf{r}}^t \end{bmatrix} = \begin{bmatrix} \frac{1}{2}\Psi\mathbf{q} \\ -\frac{1}{\boldsymbol{\tau}}\mathbf{b}_{\text{rgy}} \\ \mathbf{a}_{\text{acc}} - \mathbf{R}_{t2b}\mathbf{C}_{t2b}\mathbf{g} \\ \mathbf{R}_{b2t}\mathbf{C}_{b2t}\mathbf{v}^b \end{bmatrix} \tag{5.15}$$

5.2.2 Observation Model

The calibrated navigation data from the accelerometers and magnetometers on the navigation card provides observation for the Kalman filter to correct the state prediction. Therefore, the observation vector for the extended Kalman filter is given by

$$\mathbf{z} = [\mathbf{a}_{\text{acc}} \quad \mathbf{B}_{\text{mag}}]^T \tag{5.16}$$

Although calibration has been performed for the rate gyroscopes, the measurements are still corrupted by stochastic error and noise, which cause a random walk for the quaternion state estimation. This error increases with time. Therefore, in the correct phase of the Kalman filter, the implementation of the observation vector focuses on the correction of the quaternion state estimation.

By using the accelerometers as tilt sensing devices, the random walk in pitch and roll can be corrected based on the constant Earth's gravity. Also, the magnetometers give the yaw correction with reference to the Earth's magnetic field.

Both measurements can be expressed using a quaternion representation as

$$\mathbf{a}_{\text{acc}} = \mathbf{R}_{t2b}\,\mathbf{g} = \text{g}\begin{bmatrix} 2q_1q_3 + 2q_0q_2 \\ 2q_2q_3 - 2q_0q_1 \\ 1 - 2q_1^2 - 2q_2^2 \end{bmatrix} \tag{5.17}$$

and

$$\mathbf{B}_{\text{mag}} = \mathbf{R}_{t2b}\,\mathbf{B}_e^t = \begin{bmatrix} 1 - 2q_2^2 - 2q_3^2 & 2q_1q_2 - 2q_0q_3 & 2q_1q_3 + 2q_0q_2 \\ 2q_1q_2 + 2q_0q_3 & 1 - 2q_1^2 - 2q_3^2 & 2q_2q_3 - 2q_0q_1 \\ 2q_1q_3 - 2q_0q_2 & 2q_2q_3 + 2q_0q_1 & 1 - 2q_1^2 - 2q_2^2 \end{bmatrix} \begin{bmatrix} B_{ex}^t \\ B_{ey}^t \\ B_{ez}^t \end{bmatrix} \tag{5.18}$$

where g and $\mathbf{B}_e^t$ are the Earth's gravitational constant and magnetic intensity vector with respect to the tangent plane.

5.2.3 Filter Parameters and Implementation

In order to implement the filter, a few important parameters need to be initialized on startup. First is the initial state, $\hat{\mathbf{x}}_0$. With the orientation matrix specified for initial orientation of the body frame relative to the tangent plane, the attitude quaternion is set to $[1, 0, 0, 0]^T$. The initial gyro bias drift estimates are set to 0. Because, for the conducted experiments, the body platform started from a stationary position, the initial translational velocities in the three axes of the body frame are set to 0 and the initial position is chosen to be the origin of the tangent plane.

Table 5.1. Sensor noise characteristics.

	Gyroscopes		Accelerometers		Magnetometers
Bandwidth	10 Hz	30 Hz	10 Hz	100 Hz	30 Hz
Sensor noise	0.19 °/s	0.33 °/s	0.35 mg	1.1 mg	7.1 μgauss

The key elements of the Kalman filter are the three covariance matrices, including the state error covariance, the process noise covariance, and the measurement noise covariance matrices. Since the state errors are considered uncorrelated, the

initial error covariance matrix, $\mathbf{P}_0$, has the off-diagonal entries set to 0. The diagonal entries are configured to 0.01. The measurement noise covariance matrix, $\mathbf{R}$, consists of the square of the Root Mean Square (RMS) noise for each sensor on the diagonals of the matrix. The off-diagonal terms are zero, since the measurements are assumed to be uncorrelated. The sensor noise characteristics (see Section 3.2) and the corresponding bandwidth for each signal channel (see Section 3.4) are summarized in Table 5.1. The process noise matrix on the Kalman filter, $\mathbf{Q}$, defines the model uncertainty and disturbance. Because the attitude quaternion is obtained from the angular rate measurements, the diagonal entries of the process noise covariance for the quaternion is quantified as the square of the standard derivation of the gyroscope noise.

The Earth's gravity and magnetic strength are location dependent. These values are also required for the filter initialization. Because of the gravity anomalies, the local gravity value at sea level can be calculated, given latitude λ, as [35]

$$\mathrm{g} = 9.780327(1 + 0.0053024\sin^2(\lambda) - 0.0000058\sin^2(2\lambda)) \tag{5.19}$$

This conventional gravity formula has an accuracy of $1\,\mu\mathrm{m/s}^2$ sufficient for this navigation application [35]. As mention in Section 4.3.3, the Earth's magnetic intensity vector, $\mathbf{B}_e^t$, can be quantified using the Earth's magnetic parameters available online [40], such as the total Earth's magnetic strength, B_e, the declination angle, θ_{dec}, and the inclination angle[3], θ_{inc}. The magnetic intensity vector can be formulated as

$$\mathbf{B}_e^t = \begin{bmatrix} B_e\cos\theta_{\mathrm{inc}}\sin\theta_{\mathrm{dec}} \\ B_e\cos\theta_{\mathrm{inc}}\cos\theta_{\mathrm{dec}} \\ -B_e\sin\theta_{\mathrm{inc}} \end{bmatrix} \tag{5.20}$$

The implementation procedure of the Kalman filter algorithm is outlined in the following. Matlab code showing the algorithm is presented in Appendix A.

Step 1: Data initialization The navigation card NMEA output sentences were converted into arrays of raw data for each type of sensors. Synchronization of

[3]The angle between the Earth's magnetic vector and the plane of the horizon. The positive inclination angle points down. For example, the inclination angle in Lyttelton Harbour is approximately -68.612°. Because the axis configuration of the tangent plane is north-east-up, the sign in front of the z axis (see Equation 5.20) of the magnetic vector is negative.

the data was performed due to the different sampling rates for sensors. The calibration process was conducted using the predetermined sensor calibration information. The process includes nonorthogonality correction, scale factor and bias implementation, and gyro bias temperature compensation.

Step 2: Initial alignment The accelerometer and magnetometer measurements were used to approximate the initial orientation matrix. Initial velocity and position were also specified according to the dynamics of the body platform.

Step 3: Filter initialization and loop The initial parameters of the Kalman filter were given as discussed in Section 5.2.3. The parameters include initial state, the associated error covariance matrix, and process noise and measurement noise covariance matrices. The algorithm of the Kalman filter is referred to in Section 2.5. Note that in the predict phase all the integrations were carried out using the fourth order Runge-Kutta method.

5.3 Experimental Results

For experimental purposes, the navigation card was attached to a small skate board. The initial calibration was performed according to the algorithm provided in Chapter 4. In order to verify the accuracy of the experimental results, a XH6831 USB GPS receiver was also attached to the skate board. The GPS receiver has a built-in active antenna and supports industry standard NMEA 0183 commands. It can provide horizontal position accuracy of about 15 m and velocity accuracy of about 0.1 m/s. A laptop was connected to both the navigation card and the GPS receiver via the USB interface for receiving the data through HyperTerminal.

The simulation and experimental results are demonstrated in two parts. The first part focuses on the orientation estimation performance of the Kalman filter implementing the sensor cluster in comparison with the estimation of the filter implementing the rate gyroscopes alone and the calculation based solely on the combination of accelerometers and magnetometers. The second part includes the velocity and position estimation of the sensor fusion to examine the capability of the (total state space) filtering strategy in evaluating velocity and position information.

5.3.1 Orientation Estimation

Theoretically, both gyroscopes and the combination of accelerometers and magnetometers are capable to provide orientation estimation. With known initial attitude, the orientation information can be updated using the angular rates measured by the rate gyroscopes through integration. The combination of accelerometers and magnetometers measure the relative rotation with respect to the Earth's gravity and the Earth's magnetic field to achieve the orientation information. The problem of the gyroscope orientation estimation is the gyro drift due to the fluctuations of the gyroscope offset and measurement noise. The concern of a combination of accelerometers and magnetometers is that the sensor measurements are noisy and disturbed. From the orientation estimation perspective, the disturbances include translational acceleration and magnetic disturbances. However, the resulting values of this combination have long term stability and much less drift, whereas the short term stability of gyroscopes can be utilized to compensate the disturbances of the combination. The simulation results in this part of the section is focussed on the verification of the orientation estimation capability of the designed filter to solve both the gyro drift and the disturbances of the combination of accelerometers and magnetometers.

The navigation data was simulated according to the characteristics of the MARG sensors. The orientation and some dynamic manoeuvres were designed in the simulation, and white noise was added to the ideal data. Additionally, the translational acceleration and magnetic disturbances were included in the simulated accelerometer and magnetometer measurements. The orientation estimation results are illustrated in Figure 5.2 and Figure 5.3 using the intuitive Euler angle representation. The velocity and position estimation results in the same simulation are presented in the next section. The Euler angles calculated using the combination of the accelerometers and magnetometers as well as the gyroscopes alone are shown in comparison. As seen in these figures, the sensor fusion gave significant improvement over individual sensors in orientation estimation. The combination estimation is plotted in the dashed line. Because of the translational acceleration, the combination gave erroneous pitch and roll estimation. The simulated magnetic disturbance occurring at 10 s was detected by the magnetometers. This resulted in the inaccuracy of the yaw estimation. By combining the gyroscope measurements,

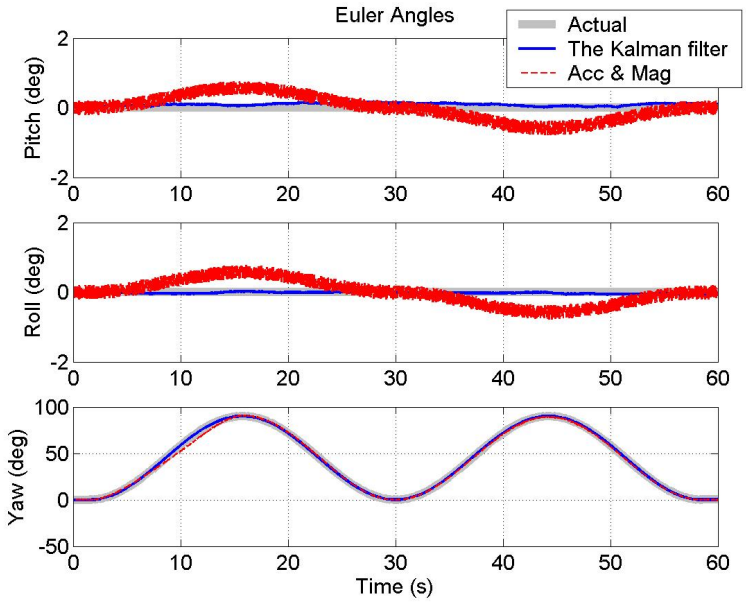

Figure 5.2. Euler angle representation of the orientation estimation from the quaternion-based extended Kalman filter using simulated MARG measurements in comparison with the Euler angles calculated using the measurements from the combination of accelerometers and magnetometers.

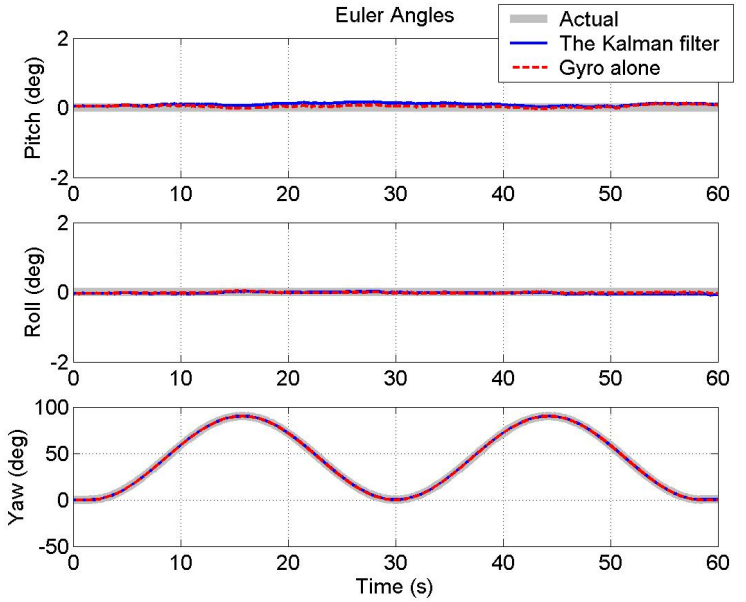

Figure 5.3. Euler angle representation of the orientation estimation from the quaternion-based extended Kalman filter using simulated MARG measurements in comparison with the Euler angles calculated using the measurements from the gyroscope alone.

the filter eliminated the disturbances and provided estimation very close to the actual values. On the other hand, the estimated values are compared with the results using the gyroscopes alone. It can be seen in Figure 5.3 that occasionally the results using the gyroscopes alone are even more closer to the actual values than those from the Kalman filter. The reason of that is that the gyro drift contaminating in the orientation estimates is comparatively small compared to the disturbances brought in by the combination so that the errors of the combination became dominant in the estimation process. Accordingly, the measurement noise covariance was increased to reduce the effects of the disturbances to the estimation, which means the model calculation based on the gyroscope measurements is trusted more. Therefore, the disturbances from the combination were compensated well whereas the compensation of the gyro drift is not really obvious.

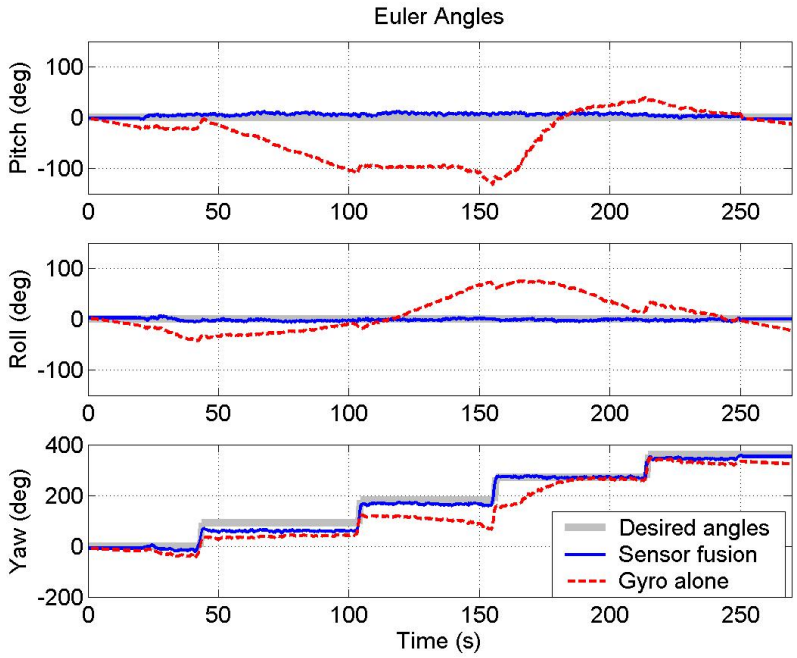

Figure 5.4. Euler angle representation of the orientation estimation in comparison with the angle values obtained from gyro alone estimation.

An experimental result is illustrated in Figure 5.4. In the experiment, the navigation card was moved around the perimeter of a football field. The Kalman filter estimated the orientation in agreement with the desired values and eliminated the gyro drift. The estimated results are also compared with the Euler angles directly

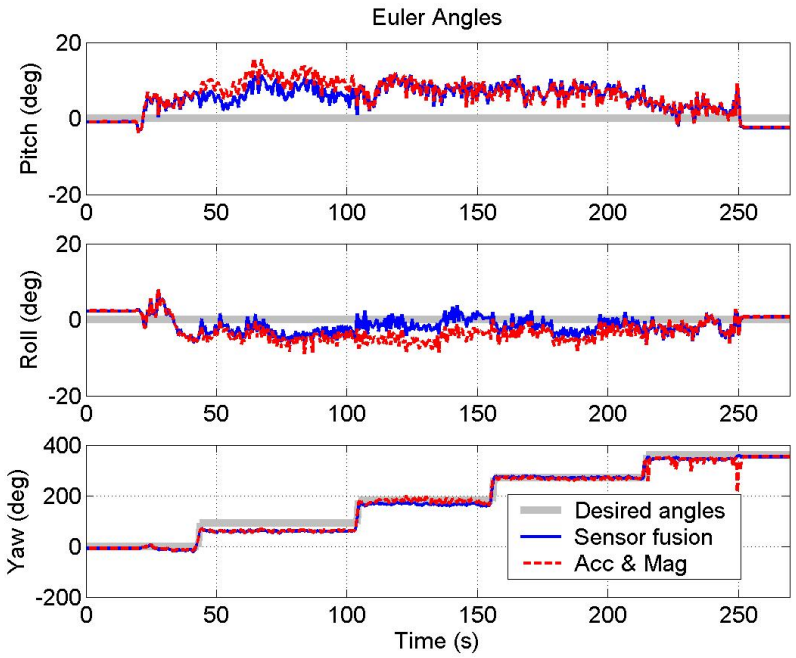

Figure 5.5. Euler angle representation of the orientation estimation in comparison with the angle values obtained from the combination of accelerometers and magnetometers.

calculated based on the combination of the accelerometers and magnetometers. The gray line represents the desired angles achieved with the assumption that the navigation card moves on a horizontal surface and each turn is a right angle. The difference of two set of Euler angles can be seen clearly. The Kalman filter removes some component from the pitch and roll angles gained from the accelerometers, which makes the estimated Euler angles closer to the desired angles. On the other hand, the yaw angle estimation from the Kalman filter provides smooth transition and eliminates the spike in the yaw angle obtained from the magnetometers. The simulation and experimental results show that the Kalman filter can tolerate linear acceleration and magnetic disturbances to a moderate degree and eliminate the gyro drift to provide considerably accurate orientation information.

5.3.2 Velocity and Position Estimation

The other important part of the experiment concentrates on velocity and position estimation. The simulation given in the last section also gives the velocity and position estimation of the designed filter. The accuracy of the velocity and po-

sition is heavily determined by the orientation estimation results. Because, from the simulation, the Kalman filter gave precise orientation to decouple the translational acceleration from the gravitational acceleration and eliminate the magnetic disturbances (see Section 5.3.1), the velocity and position estimation were resolved using the resulting translational acceleration and orientation information. The results are illustrated in Figure 5.6 and Figure 5.7. As can be seen, the velocity and position calculated from the Kalman filter match closely to the actual values. For testing the robustness of the filter in practice, some experiments were performed, and results are shown in the following section.

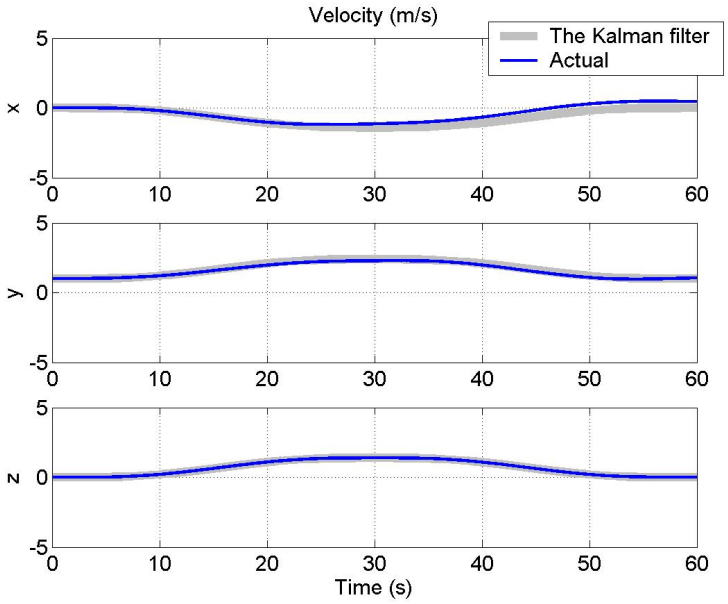

Figure 5.6. Velocity estimates with respect to the body frame resulted from the quaternion-based extended Kalman filter using simulated MARG measurements.

Figure 5.8 presents the position estimation of the quaternion-based extended Kalman filter compared with the values obtained from the USB GPS unit. In this experiment, the skate board was pulled along a slightly curved path on a flat surface. In the figure, the square represents the start point and the circle represents the last sampling point. All position information is expressed with respect to the tangent plane. It can be seen that the sensor fusion prediction followed the trajectory obtained from GPS very closely at the beginning but drifted apart close to the finish. The GPS did not provide accurate position information due to

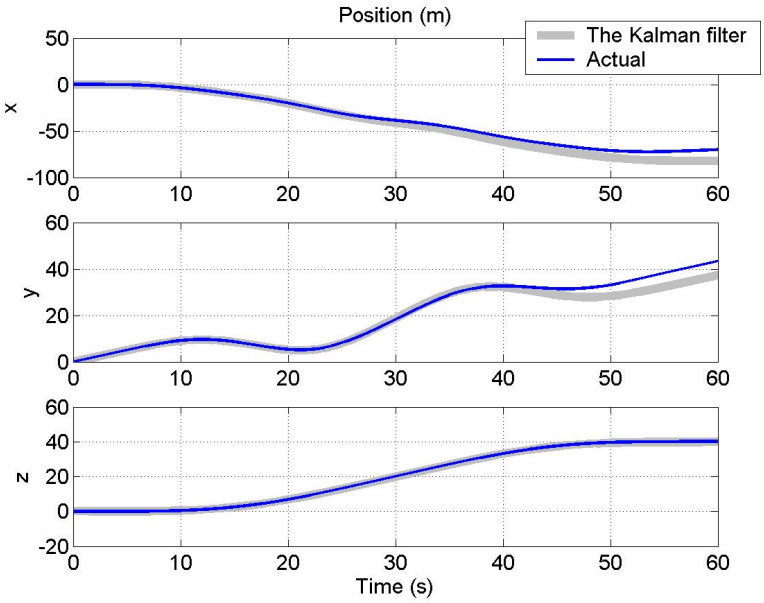

Figure 5.7. Position estimates with respect to the tangent plane resulted from the quaternion-based extended Kalman filter using simulated MARG measurements.

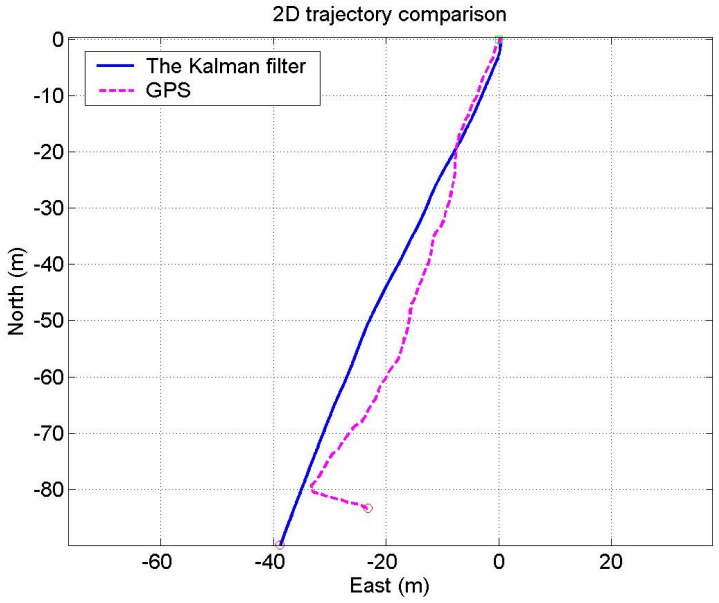

Figure 5.8. 2D trajectory plot of a straight line run using the position estimated by the quaternion-based extended Kalman filter in comparison with the position obtained from GPS.

the limited accuracy especially when the skate board approached the end of the path. This can be more clearly seen from a 3D position plot shown in Figure 5.9. Comparatively, the position estimated by the sensor fusion has smoother transition and is more realistic.

The effectiveness of the sensor fusion estimation can also be demonstrated with and without the aid of the accelerometers and magnetometers. In this experiment, the skate board started stationary and was moved in anti-clockwise circles three times. The position plot shown in Figure 5.11 is obtained from the prediction based on the gyroscopes alone. The predicted position plots a spiral growing in scale. The performance is unsatisfactory due to the gyro drift and noise. In comparison, when the Kalman filter was aided by the observation of the accelerometers and magnetometers, the performance is improved. The resulting position estimation is given in Figure 5.11 in comparison with the GPS-obtained position. However, because the navigation card is not velocity-aided or position-aided, the growing errors of velocity and position estimation can not be eliminated effectively.

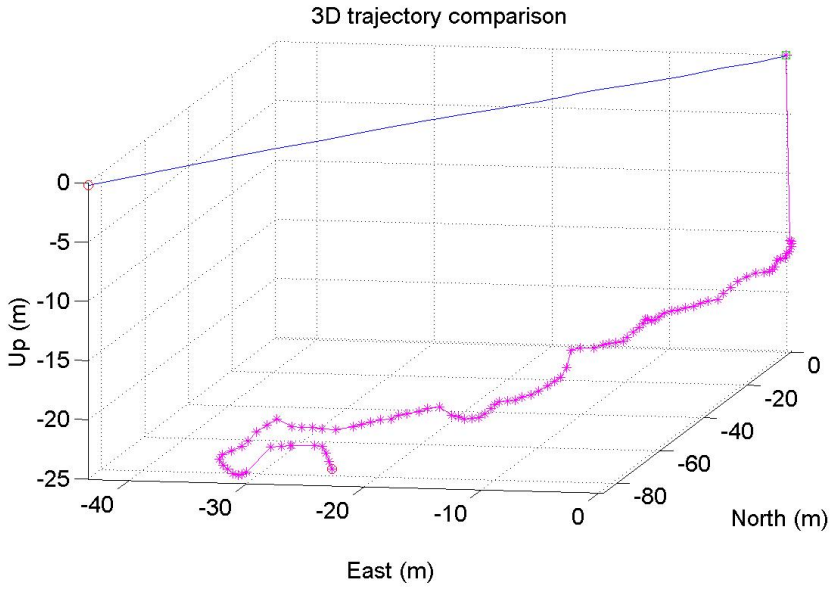

Figure 5.9. 3D trajectory plot of a straight line run using the position estimated by the quaternion-based extended Kalman filter in comparison with the position obtained from GPS.

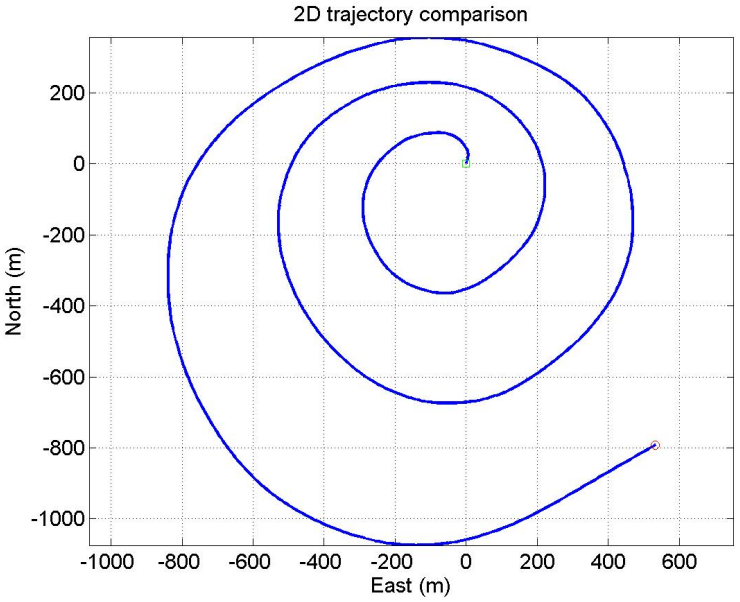

Figure 5.10. 2D trajectory plot of three anti-clockwise circles estimated by the quaternion-based extended Kalman filter without the aid of the accelerometers and magnetometers.

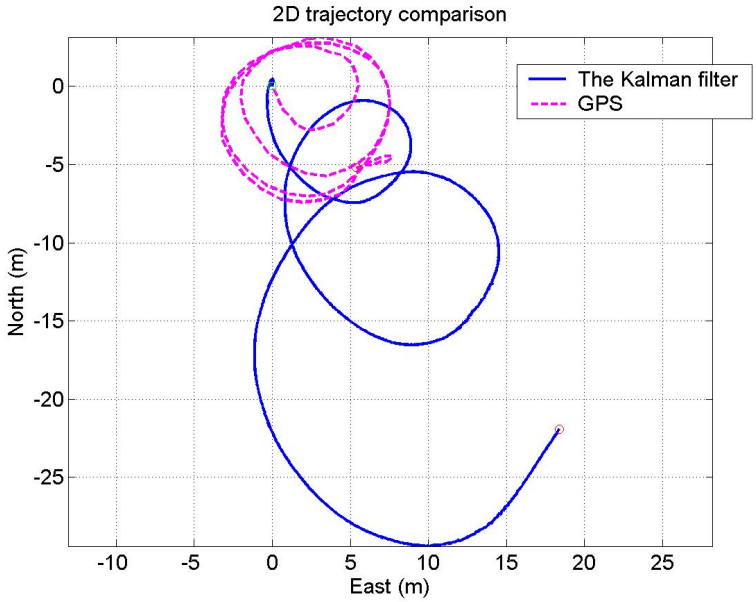

Figure 5.11. 2D trajectory plot of three anti-clockwise circles estimated by the quaternion-based extended Kalman filter with the aid of the accelerometers and magnetometers in comparison with the position obtained from GPS.

CHAPTER 6

CONCLUSIONS AND RECOMMENDATIONS

6.1 Conclusions

The work in this thesis developed a thorough navigation solution for orientation and position tracking. It included the construction of the integrated sensing module, sensor calibration algorithm study, and sensor fusion implementation.

An integrated navigation card was constructed based on low-cost off-the-shelf MARG sensors. The sensor cluster was mounted in an orthogonal triad configuration to monitor the motions in six degrees of freedom. The data acquisition system and associated electronics were tested and are able to correctly sample and transmit the navigation data to the towfish computer for postprocessing.

Sensor calibration algorithms were studied and the stochastic properties of the sensors were analyzed. The nonlinear least squares algorithm was used to minimize cost functions based on the accelerometer and magnetometer models to determine the calibration parameters, such as scale factor and misalignment. Some results

demonstrated the accuracy of the calibration algorithm.

Sensor fusion was developed based on the extended Kalman filter. The quaternion was used for the parameterization of the coordinate transformation. It simplified the rotation and derivative calculations and improved the fusion efficiency. The extended Kalman filter was based on a total state space model, which outputs the position, velocity, and attitude as well as the gyro bias. The total state space scheme provided a simple and efficient estimation method. The simulations and experimental results demonstrated that the MARG sensors can be configured in a complementary fashion to compensate the weakness of one sensor with the strength of another sensor. It was also proven that the Kalman filter using the total state space model can provide accurate orientation estimation but is inadequate for position and velocity estimation based on only the MARG sensors due to the sensor noise and integration error. The filter gave poorer estimation results when the platform had more manoeuvres.

6.2 Recommendations

Compared to the total state space model, the error state space model has more advantages. The error model defines the errors of the sensors rather than the total states, such as position and velocity. The inputs for this model are the deviation of each defined total state. Because the error state space model only provides the correction for the sensor signals, it is more robust than the total state space model. However, because the error state space model contains more nonlinear terms, the complexity of the model is increased correspondingly. By applying the error state space model, the errors of the sensor parameters as well as the uncertainty of initial parameters can be estimated with improved accuracy. Moreover, different sensor fusion algorithm can be adopted, such as the unscented Kalman filter [17]. The unscented Kalman filter uses a deterministic sampling technique to specify a minimal set of carefully chosen sample points, which propagate through the nonlinear model capturing the mean and covariance accurate to the second order [17]. The unscented Kalman filter can improve the robustness of the estimation.

Currently, the in-motion alignment scheme is totally based on theoretical consumption. Some parameters can not be accurately computed in practice. The

error state space model can also include the initial alignment error so that the initial values can be indirectly determined by the filter. The unscented Kalman filter can improve the tolerance towards the erroneous initial values so that large initial alignment errors are allowed [48].

The system can also be improved by including velocity or position sensors, for example, a doppler velocity log (DVL). As mentioned, the constructed total state space model is capable of accurate orientation estimation based on the integrated MARG sensors. If velocity or position information is available, the errors caused by sensor noise and integration error can be compensated accordingly. A simple and low-cost solution is to integrate a flow sensor to roughly determine the velocity of the underwater vehicle or a GPS unit for position fixing when the underwater vehicle periodically swims to the surface. The redundant axes of the ADXL203 accelerometers can also be implemented in the future research to improve the system performance [50].

APPENDIX A

MATLAB CODE

```
% Quaternion-based extended Kalman filter matlab code
%   Process including
%   1. Data initialization
%   2. Initial alignment
%   3. Kalman filter initialization and loop

% Globalization
global tau_b g Bt dec inc
% Initialize parameters
tau_b = 400;
% the Earth's gravity calculated according the latitude value
g = 9.7905;
% The Earth's magnetic field strength
Bt = 0.5791331;
% Declination angle, pointing to the north-east direction
dec = 23.356;
% Inclination angle, pointing up in the southern hemisphere
inc = 68.612;

% 1. Data loading
% Ananmea is a funtion to read and synchronize the navigation
% data from a NMEA file
[acc,rgy,mag,msc]=ananmea('..\logs\navf27.txt');

% Sensor calibration and compensation
% Accelerometer nonorthogonality correction matrix
pa = [89.9117 91.1850 88.8985]/180*pi; % Alignment angles (deg)
pam33 = sqrt(1-cos(pa(2))*cos(pa(2))-cos(pa(3))*cos(pa(3)));
pam = [1 0 0;cos(pa(1)) sin(pa(1)) 0;...
       cos(pa(3)) cos(pa(2)) pam33];
tam = [1 0 0.0094;0.0002 0.9998 -0.0180;-0.0094 0.0180 0.9998];
% Precalibrated magnetometer correction matrix
pm = [89.70 85.73 86.38]/180*pi; % Alignment angles (deg)
pmm33 = sqrt(1-cos(pa(2))*cos(pa(2))-cos(pa(3))*cos(pa(3)));
pmm = [1 0 0;cos(pa(1)) sin(pa(1)) 0;...
       cos(pa(3)) cos(pa(2)) pmm33];
% Calibration scale factor and bias (low bandwidth accelerometers)
accnull = [32296.5 32736.5 32300.5];
accsf = [0.9854 0.9864 0.9951]; % V/g
magnull = [33674 33129 33389];
magsf = [1.0682 1.0987 1.1408]; % V/gauss
% acceleration x
acca(:,1) = -(acc(:,4) - accnull(1))*5/65536/accsf(1);
% acceleration y
acca(:,2) = -(acc(:,5) - accnull(2))*5/65536/accsf(2);
% acceleration z
acca(:,3) =  (acc(:,6) - accnull(3))*5/65536/accsf(3);
% magnetic strength x
maga(:,1) =  (mag(:,1) - magnull(1))*5/65536/magsf(1);
% magnetic strength y
maga(:,2) = -(mag(:,2) - magnull(2))*5/65536/magsf(2);
% magnetic strength z
maga(:,3) = -(mag(:,3) - magnull(3))*5/65536/magsf(3);
% Orthogonality correction process
for i = 1:length(acca)
    accb(i,:) = (inv(tam)*inv(pam)*acca(i,:)')';
end
for i = 1:length(maga)
    magb(i,:) = (inv(pmm)*maga(i,:)')';
end
% Bias compensation process using bias-temperature lookup table
load rgycalt
% Biasconvertor is a function to track the null value by matching
% the current temperature measurement with the lookup table
% provided by the MAT file.
rgynull = biasconvertor(rgy,msc,[t1 t2 t3 r1 r2 r3]);
% Manufacturer specified scale factor is used for gyros
rgysf = [0.015 0.015 0.015];     % V/deg/s
for i = 1:length(rgy)
    rgyb(i,:) = -(rgy(i,1:3) - rgynull(1,:))*5/65536./rgysf;
end

% 2. Initial alignment
% Initial Euler angles calculation (rad/s)
iniang(1:2) = [atan(accb(1,2)/accb(1,3)) -asin(accb(1,1))];
magt(1) = cos(iniang(2))*magb(1,1)...
            +sin(iniang(2))*sin(iniang(1))*magb(1,2)...
            +sin(iniang(2))*cos(iniang(1))*magb(1,3);
magt(2) = cos(iniang(1))*magb(1,2)-sin(iniang(1))*magb(1,3);
iniang(3) = atan2(magt(1),magt(2))-dec/180*pi;
% Initial orientation matrix calculation
bt11 = cos(iniang(3))*cos(iniang(2));
bt12 = -sin(iniang(3))*cos(iniang(1))...
       +cos(iniang(3))*sin(iniang(2))*sin(iniang(1));
bt13 = sin(iniang(3))*sin(iniang(1))...
       +cos(iniang(3))*sin(iniang(2))*cos(iniang(1));
bt21 = sin(iniang(3))*cos(iniang(2));
bt22 = cos(iniang(3))*cos(iniang(1))...
       +sin(iniang(3))*sin(iniang(2))*sin(iniang(1));
bt23 = -cos(iniang(3))*sin(iniang(1))...
       +sin(iniang(3))*sin(iniang(2))*cos(iniang(1));
bt31 = -sin(iniang(2));
```

```
bt32 = cos(iniang(2))*sin(iniang(1));
bt33 = cos(iniang(2))*cos(iniang(1));
inib2t = [bt11 bt12 bt13; bt21 bt22 bt23; bt31 bt32 bt33];
init2b = inib2t';
% Initial velocity of tangent plane and body frame.
% For experiments, the platform starts from stationary
inivelb = [0 0 0];          % m/s^2
invelt = (inib2t*inivelb')';% m/s^2

% 3. Kalman filter initialization and loop
% State vector:
%   x1: quaternion component q0 (scalar)
%   x2: quaternion component q1
%   x3: quaternion component q2
%   x4: quaternion component q3
%   x5: angular rate bias for x-axis
%   x6: angular rate bias for y-axis
%   x7: angular rate bias for z-axis
%   x8: velocity in x-axis of body frame
%   x9: velocity in y-axis of body frame
%  x10: velocity in z-axis of body frame
%  x11: Position East
%  x12: Postion North
%  x13: Position Up

% Sampling frequency of the gyroscopes
rgyfreq = 200/3;
% Initialize the time stamp
h = 1/rgyfreq;
t = 0;
% Kalman filter initialization
clear S
S.x = [1 0 0 0 0 0 0 invelb 0 0 0]';
state = length(S(1).x);
S.P = 0.01*eye(state);
S.z = [accb(1,:) magb(1,:)]';
Qrgy = [(0.19/180*pi)^2 0 0;0 (0.33/180*pi)^2 0;...
          0 0 (0.33/180*pi)^2];
Q = [Qrgy zeros(3,state-3);zeros(state-3,3) 0.01*eye(state-3)];
R = [(0.35e-3)^2*eye(3) zeros(3);zeros(3) (7.1e-6)^2*eye(3)];

% Main loop of the Kalman filter
total = length(rgyb);
% Initialize waitbar
waiter=waitbar(0,'Filtering in progress');
for count = 1:total
    waitbar(count/total,waiter);
    x = S(end).x;
    P = S(end).P;
    z = [accb(count,:) magb(count,:)]';
    % The predict process using the 4th order Runge-Kutta method
    xhat = rk4(x,t(count),h,'procmod',...
           [accb(count,:)' init2b rgyb(count,:)'/180*pi]);
    t(count+1) = t(count) + h;
    % Calcuate Jacobian matrix (partial derivatives of f related to x)
    A = feval('jprocmod',x,[],[],...
        [accb(count,:)' init2b rgyb(count,:)'/180*pi]);
    % Calculate error covariance matrix
    Phat = A*P*A' + Q;
    % Calcuate Jacobian matrix (partial derivatives of h related to x)
    H = feval('jmeasmod',x,[],accb(1,:),magb(1,:));
    % Compute the Kalman gain.
    K = Phat*H'/(H*Phat*H'+R);
    % Correct Process
    zhat = feval('measmod',xhat,[],accb(1,:),magb(1,:));
    x = xhat + K*(z - zhat);
    % Perform quaternion normalization
    x(1:4,:) = quatnormalizer(x(1:4,:));
    % Update error covariance matrix
    P = (eye(state) - K*H)*Phat;
    % Store results
    S(end+1).x = x;
    S(end).P = P;
    S(end).z = zhat;
end
close(waiter);
```

```
function dq = procmod(x,t,param)
% Process model for predicting the state estimates
global tau_b g
acb = param(:,1);
init2b = param(:,2:4);
rgb = param(:,5);
inib2t = init2b';

if length(x) == 13
    x1 = x(1); x2 = x(2); x3 = x(3); x4 = x(4); x5 = x(5);
    x6 = x(6); x7 = x(7); x8 = x(8); x9 = x(9); x10 = x(10);
    x11 = x(11); x12 = x(12); x13 = x(13);
```

```
13  else
14      return
15  end
16
17  r1 = rgb(1) - x5;
18  r2 = rgb(2) - x6;
19  r3 = rgb(3) - x7;
20
21  % Process model state equation
22  dq(1:4,:) = 1/2*[0 r1 r2 r3;
23                   -r1 0 -r3 r2;
24                   -r2 r3 0 -r1;
25                   -r3 -r2 r1 0]*[x1 x2 x3 x4]';
26  mt2b = [1-2*x3^2-2*x4^2 2*x2*x3-2*x1*x4 2*x2*x4+2*x1*x3;
27          2*x2*x3+2*x1*x4 1-2*x2^2-2*x4^2 2*x3*x4-2*x1*x2;
28          2*x2*x4-2*x1*x3 2*x3*x4+2*x1*x2 1-2*x2^2-2*x3^2];
29  mb2t = mt2b';
30  dq(5:7,:) = -1/tau_b*eye(3)*x(5:7);
31  dq(8:10,:) = g*(acb-mt2b*init2b*[0 0 1]');
32  dq(11:13,:) = inib2t*mb2t*[x8 x9 x10]';
```

```
1   function A = jprocmod(x,u,w,param)
2   % Process model Jacobian matrix
3   global tau_b g
4   acb = param(:,1);
5   init2b = param(:,2:4);
6   rgb = param(:,5);
7   inib2t = init2b';
8
9   if length(x) == 13
10      x1 = x(1); x2 = x(2); x3 = x(3); x4 = x(4); x5 = x(5);
11      x6 = x(6); x7 = x(7); x8 = x(8); x9 = x(9); x10 = x(10);
12      x11 = x(11); x12 = x(12); x13 = x(13);
13  else
14      return
15  end
16
17  if length(u) == 0, u = zeros(13,1); end
18
19  a1 = acb(1); a2 = acb(2); a3 = acb(3);
20  A = zeros(13,13);
21
22  r1 = rgb(1) - x5;
23  r2 = rgb(2) - x6;
24  r3 = rgb(3) - x7;
25
26  A(1,2) =  1/2*r1;
27  A(1,3) =  1/2*r2;
28  A(1,4) =  1/2*r3;
29  A(1,5) = -1/2*x2;
30  A(1,6) = -1/2*x3;
31  A(1,7) = -1/2*x4;
32  A(2,1) = -1/2*r1;
33  A(2,3) = -1/2*r3;
34  A(2,4) =  1/2*r2;
35  A(2,5) =  1/2*x1;
36  A(2,6) = -1/2*x4;
37  A(2,7) =  1/2*x3;
38  A(3,1) = -1/2*r2;
39  A(3,2) =  1/2*r3;
40  A(3,4) = -1/2*r1;
41  A(3,5) =  1/2*x4;
42  A(3,6) =  1/2*x1;
43  A(3,7) = -1/2*x2;
44  A(4,1) = -1/2*r3;
45  A(4,2) = -1/2*r2;
46  A(4,3) =  1/2*r1;
47  A(4,5) = -1/2*x3;
48  A(4,6) =  1/2*x2;
49  A(4,7) =  1/2*x1;
50
51  A(5,5) = -1/tau_b;
52  A(6,6) = -1/tau_b;
53  A(7,7) = -1/tau_b;
54
55  A(8,1) = -g*(-2*x4*init2b(2,3)+2*x3*init2b(3,3));
56  A(8,2) = -g*(2*x3*init2b(2,3)+2*x4*init2b(3,3));
57  A(8,3) = -g*(-4*x3*init2b(1,3)+2*x2*init2b(2,3)...
58            + 2*x1*init2b(3,3));
59  A(8,4) = -g*(-4*x4*init2b(1,3)-2*x1*init2b(2,3)...
60            + 2*x2*init2b(3,3));
61  A(9,1) = -g*(2*x4*init2b(1,3)-2*x2*init2b(3,3));
62  A(9,2) = -g*(2*x3*init2b(1,3)-4*x2*init2b(2,3)...
63            - 2*x1*init2b(3,3));
64  A(9,3) = -g*(2*x2*init2b(1,3)+2*x4*init2b(3,3));
65  A(9,4) = -g*(2*x1*init2b(1,3)-4*x4*init2b(2,3)...
66            + 2*x3*init2b(3,3));
67  A(10,1) = -g*(-2*x3*init2b(1,3)+2*x2*init2b(2,3));
68  A(10,2) = -g*(2*x4*init2b(1,3)+2*x1*init2b(2,3)...
```

```
            - 4*x2*init2b(3,3));
A(10,3) = -g*(-2*x1*init2b(1,3)+2*x4*init2b(2,3)...
            - 4*x3*init2b(3,3));
A(10,4) = -g*(2*x2*init2b(1,3)+2*x3*init2b(2,3));

A(11,1) = inib2t(1,1)*(2*x4*x9-2*x3*x10)...
          +inib2t(1,2)*(-2*x4*x8+2*x2*x10)...
          +inib2t(1,3)*(2*x3*x8-2*x2*x9);
A(11,2) = inib2t(1,1)*(2*x3*x9+2*x4*x10)...
          +inib2t(1,2)*(2*x3*x8-4*x2*x9+2*x1*x10)...
          +inib2t(1,3)*(2*x4*x8-2*x1*x9-4*x2*x10);
A(11,3) = inib2t(1,1)*(-4*x3*x8+2*x2*x9-2*x1*x10)...
          +inib2t(1,2)*(2*x1*x8+2*x4*x10)...
          +inib2t(1,3)*(2*x1*x8+2*x4*x9-4*x3*x10);
A(11,4) = inib2t(1,1)*(-4*x4*x8+2*x1*x9+2*x2*x10)...
          +inib2t(1,2)*(-2*x1*x8-4*x4*x9+2*x3*x10)...
          +inib2t(1,3)*(2*x2*x8+2*x3*x9);
A(11,8) = inib2t(1,1)*(1-2*x3^2-2*x4^2)...
          +inib2t(1,2)*(2*x2*x3-2*x1*x4)...
          +inib2t(1,3)*(2*x2*x4+2*x1*x3);
A(11,9) = inib2t(1,1)*(2*x2*x3+2*x1*x4)...
          +inib2t(1,2)*(1-2*x2^2-2*x4^2)...
          +inib2t(1,3)*(2*x3*x4-2*x1*x2);
A(11,10) = inib2t(1,1)*(2*x2*x4-2*x1*x3)...
          +inib2t(1,2)*(2*x3*x4+2*x1*x2)...
          +inib2t(1,3)*(1-2*x2^2-2*x3^2);
A(12,1) = inib2t(2,1)*(2*x4*x9-2*x3*x10)...
          +inib2t(2,2)*(-2*x4*x8+2*x2*x10)...
          +inib2t(2,3)*(2*x3*x8-2*x2*x9);
A(12,2) = inib2t(2,1)*(2*x3*x9+2*x4*x10)...
          +inib2t(2,2)*(2*x3*x8-4*x2*x9+2*x1*x10)...
          +inib2t(2,3)*(2*x4*x8-2*x1*x9-4*x2*x10);
A(12,3) = inib2t(2,1)*(-4*x3*x8+2*x2*x9-2*x1*x10)...
          +inib2t(2,2)*(2*x1*x8+2*x4*x10)...
          +inib2t(2,3)*(2*x1*x8+2*x4*x9-4*x3*x10);
A(12,4) = inib2t(2,1)*(-4*x4*x8+2*x1*x9+2*x2*x10)...
          +inib2t(2,2)*(-2*x1*x8-4*x4*x9+2*x3*x10)...
          +inib2t(2,3)*(2*x2*x8+2*x3*x9);
A(12,8) = inib2t(2,1)*(1-2*x3^2-2*x4^2)...
          +inib2t(2,2)*(2*x2*x3-2*x1*x4)...
          +inib2t(2,3)*(2*x2*x4+2*x1*x3);
A(12,9) = inib2t(2,1)*(2*x2*x3+2*x1*x4)...
          +inib2t(2,2)*(1-2*x2^2-2*x4^2)...
          +inib2t(2,3)*(2*x3*x4-2*x1*x2);
A(12,10) = inib2t(2,1)*(2*x2*x4-2*x1*x3)...
          +inib2t(2,2)*(2*x3*x4+2*x1*x2)...
          +inib2t(2,3)*(1-2*x2^2-2*x3^2);
A(13,1) = inib2t(3,1)*(2*x4*x9-2*x3*x10)...
          +inib2t(3,2)*(-2*x4*x8+2*x2*x10)...
          +inib2t(3,3)*(2*x3*x8-2*x2*x9);
A(13,2) = inib2t(3,1)*(2*x3*x9+2*x4*x10)...
          +inib2t(3,2)*(2*x3*x8-4*x2*x9+2*x1*x10)...
          +inib2t(3,3)*(2*x4*x8-2*x1*x9-4*x2*x10);
A(13,3) = inib2t(3,1)*(-4*x3*x8+2*x2*x9-2*x1*x10)...
          +inib2t(3,2)*(2*x1*x8+2*x4*x10)...
          +inib2t(3,3)*(2*x1*x8+2*x4*x9-4*x3*x10);
A(13,4) = inib2t(3,1)*(-4*x4*x8+2*x1*x9+2*x2*x10)...
          +inib2t(3,2)*(-2*x1*x8-4*x4*x9+2*x3*x10)...
          +inib2t(3,3)*(2*x2*x8+2*x3*x9);
A(13,8) = inib2t(3,1)*(1-2*x3^2-2*x4^2)...
          +inib2t(3,2)*(2*x2*x3-2*x1*x4)...
          +inib2t(3,3)*(2*x2*x4+2*x1*x3);
A(13,9) = inib2t(3,1)*(2*x2*x3+2*x1*x4)...
          +inib2t(3,2)*(1-2*x2^2-2*x4^2)...
          +inib2t(3,3)*(2*x3*x4-2*x1*x2);
A(13,10) = inib2t(3,1)*(2*x2*x4-2*x1*x3)...
          +inib2t(3,2)*(2*x3*x4+2*x1*x2)...
          +inib2t(3,3)*(1-2*x2^2-2*x3^2);
```

```
function z = measmod(x,w,gt,h)
% Measurement model used for updating estimation
if length(x) == 13
    x1 = x(1); x2 = x(2); x3 = x(3); x4 = x(4); x5 = x(5);
    x6 = x(6); x7 = x(7); x8 = x(8); x9 = x(9); x10 = x(10);
    x11 = x(11); x12 = x(12); x13 = x(13);
else
    return
end

h1 = h(1); h2 = h(2); h3 = h(3);

z(1,:) = (x1^2+x2^2-x3^2-x4^2)*gt(1)+2*(x2*x3-x1*x4)*gt(2)...
         + 2*(x2*x4+x1*x3)*gt(3);
z(2,:) = 2*(x2*x3+x1*x4)*gt(1)+(x1^2+x3^2-x2^2-x4^2)*gt(2)...
         + 2*(x3*x4-x1*x2)*gt(3);
z(3,:) = 2*(x2*x4-x1*x3)*gt(1)+2*(x3*x4+x1*x2)*gt(2)...
         + (x1^2+x4^2-x2^2-x3^2)*gt(3);
z(4,:) = (x1^2+x2^2-x3^2-x4^2)*h1+2*(x2*x3-x1*x4)*h2...
         + 2*(x2*x4+x1*x3)*h3;
```

```
21  z(5,:) = 2*(x2*x3+x1*x4)*h1+(x1^2+x3^2-x2^2-x4^2)*h2 ...
22           + 2*(x3*x4-x1*x2)*h3;
23  z(6,:) = 2*(x2*x4-x1*x3)*h1+2*(x3*x4+x1*x2)*h2 ...
24           + (x1^2+x4^2-x2^2-x3^2)*h3;
```

```
1  function H = jmeasmod(x,w,gt,h)
2  % Measurement model Jacobian matrix
3  if length(x) == 13
4      x1 = x(1); x2 = x(2); x3 = x(3); x4 = x(4); x5 = x(5);
5      x6 = x(6); x7 = x(7); x8 = x(8); x9 = x(9); x10 = x(10);
6      x11 = x(11); x12 = x(12); x13 = x(13);
7  else
8      return
9  end
10
11 h1 = h(1); h2 = h(2); h3 = h(3);
12 H = zeros(6,13);
13
14 H(1,1) = 2*x1*gt(1)-2*x4*gt(2)+2*x3*gt(3);
15 H(1,2) = 2*x2*gt(1)+2*x3*gt(2)+2*x4*gt(3);
16 H(1,3) = -2*x3*gt(1)+2*x2*gt(2)+2*x1*gt(3);
17 H(1,4) = -2*x4*gt(1)-2*x1*gt(2)+2*x2*gt(3);
18 H(2,1) = 2*x4*gt(1)+2*x1*gt(2)-2*x2*gt(3);
19 H(2,2) = 2*x3*gt(1)-2*x2*gt(2)-2*x1*gt(3);
20 H(2,3) = 2*x2*gt(1)+2*x3*gt(2)+2*x4*gt(3);
21 H(2,4) = 2*x1*gt(1)-2*x4*gt(2)+2*x3*gt(3);
22 H(3,1) = -2*x3*gt(1)+2*x2*gt(2)+2*x1*gt(3);
23 H(3,2) = 2*x4*gt(1)+2*x1*gt(2)-2*x2*gt(3);
24 H(3,3) = -2*x1*gt(1)+2*x4*gt(2)-2*x3*gt(3);
25 H(3,4) = 2*x2*gt(1)+2*x3*gt(2)+2*x4*gt(3);
26 H(4,1) = 2*x1*h1-2*x4*h2+2*x3*h3;
27 H(4,2) = 2*x2*h1+2*x3*h2+2*x4*h3;
28 H(4,3) = -2*x3*h1+2*x2*h2+2*x1*h3;
29 H(4,4) = -2*x4*h1-2*x1*h2+2*x2*h3;
30 H(5,1) = 2*x4*h1+2*x1*h2-2*x2*h3;
31 H(5,2) = 2*x3*h1-2*x2*h2-2*x1*h3;
32 H(5,3) = 2*x2*h1+2*x3*h2+2*x4*h3;
33 H(5,4) = 2*x1*h1-2*x4*h2+2*x3*h3;
34 H(6,1) = -2*x3*h1+2*x2*h2+2*x1*h3;
35 H(6,2) = 2*x4*h1+2*x1*h2-2*x2*h3;
36 H(6,3) = -2*x1*h1+2*x4*h2-2*x3*h3;
37 H(6,4) = 2*x2*h1+2*x3*h2+2*x4*h3;
```

APPENDIX B

NAVIGATION CARD SCHEMATICS

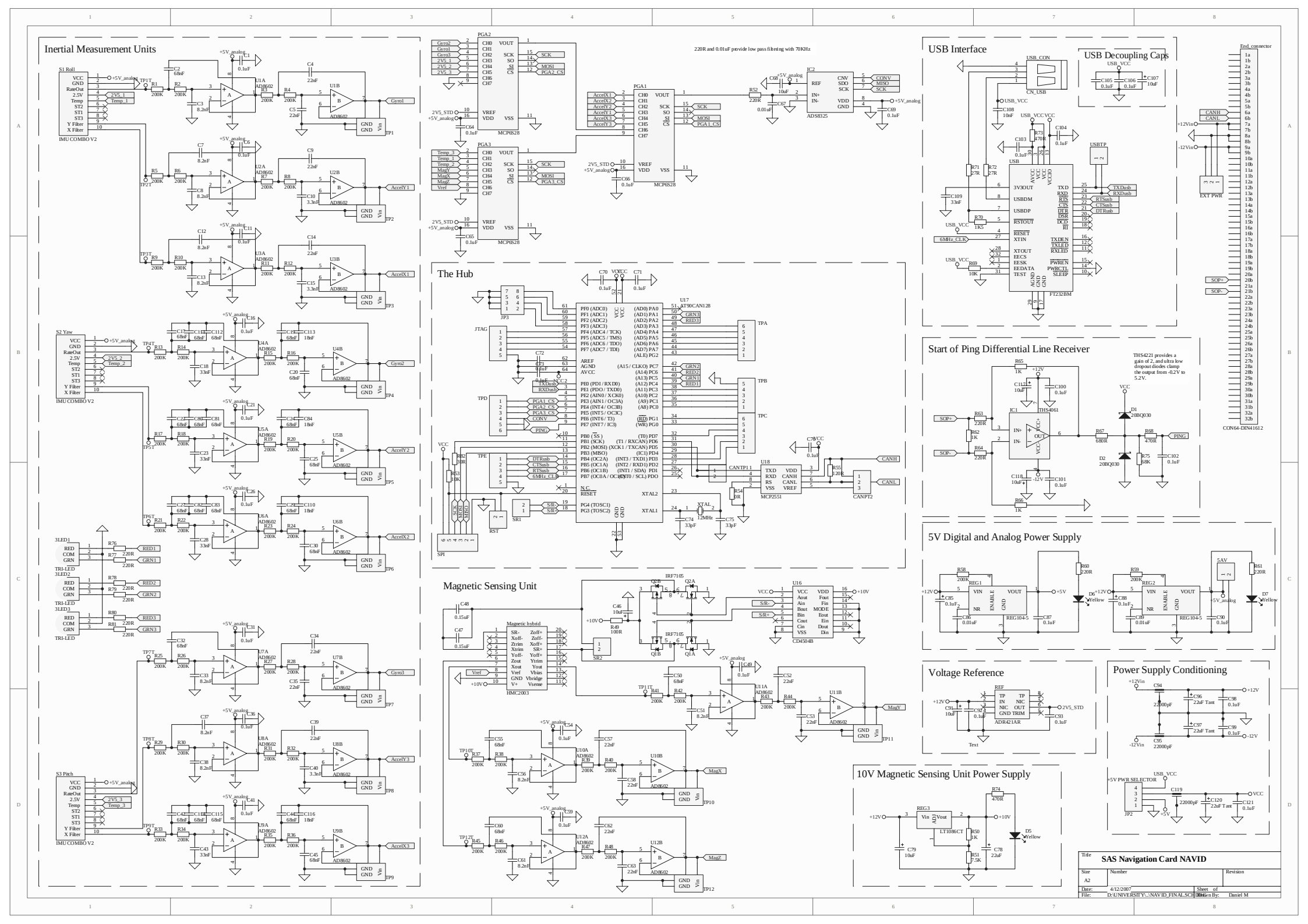
Inertial Measurement Units
IMU COMBO V2
S1 Roll
S2 Yaw
S3 Pitch
TRI-LED
3LED1
3LED2
3LED3
PGA2
PGA3
PGA1
MCP6S28
ADS8325
220R and 0.01uF provide low pass filtering with 70KHz
The Hub
JTAG
SPI
AT90CAN128
MCP2551
CANTP1
CANTP2
USB Interface
USB_CON
CN_USB
FT232BM
EXT PWR
USB Decoupling Caps
End_connector
CON64-DIN41612
Start of Ping Differential Line Receiver
THS4221 provides a gain of 2, and ultra low dropout diodes clamp the output from -0.2V to 5.2V.
THS4061
5V Digital and Analog Power Supply
REG1
REG2
REG104-5
Voltage Reference
ADR421AR
Power Supply Conditioning
10V Magnetic Sensing Unit Power Supply
LT1086CT
Magnetic Sensing Unit
Magnetic hybrid
HMC2003
CD4504B
IRF7105
Title
SAS Navigation Card NAVID
Size
A2
Number
Revision
Date:
4/12/2007
Sheet of
File:
D:\UNIVERSITY\...\NAVID_FINALSCH.DDB
Drawn By:
Daniel M

REFERENCES

[1] J. Pat, "Synthetic aperture sonar image reconstruction using a multiple-receiver towfish," Master's thesis, Department of Electrical and Computer Engineering, University of Canterbury, March 2000.

[2] D. W. Hawkins, *Synthetic Aperture Imaging Algorithms: with application to wide bandwidth sonar*. PhD thesis, Department of Electrical and Computer Engineering, University of Canterbury, October 1996.

[3] J. J. Mach, "Toward auto-calibration of navigation sensors for miniature autonomous underwater vehicles," Master's thesis, Virginia Polytechnic Institute and State University, USA, July 2003.

[4] R. E. Kalman, "A new approach to linear filtering and prediction problems," *Transaction of the ASME – Journal of Basic Engineering*, pp. 35–45, 1960.

[5] N. Eduardo and D. W. Hugh, "Initial calibration and alignment of low cost inertial navigation units for land vehicle applications," *Journal of Robotics Systems*, pp. 81–92, February 1999.

[6] J. S. Dittrich and E. N. Johnson, "Multi-sensor navigation system for an autonomous helicopter," in *AIAA/IEEE Digital Avionics Systems Conference*, 2002.

[7] D. Gebre-Egziabher, R. C. Hayward, and J. D. Powell, "Design of multi-sensor attitude determination systems," *IEEE Transactions on Aerospace and Electronic Systems*, pp. 627–649, March 2004.

[8] E. N. Pilbrow, M. P. Hayes, and P. T. Gough, "Inertial navigation system for a synthetic aperture sonar towfish," in *ENZCON2002*, November 2002.

[9] E. Foxlin, "Inertial head-tracker sensor fusion by a complementary separate-bais Kalman filter," in *Proceedings of the IEEE Virtual Reality Annual International Symposium*, pp. 185–194, 1996.

[10] G. Welch and G. Bishop, "An introduction to the Kalman filter," Tech. Rep. 95-041, Department of Computer Science, University of North Carolina, 2001.

[11] J. T. Cushing, *Philosophical Concepts in Physics*. Cambridge, UK: Cambridge University Press, 1998.

[12] J. A. Farnell and M. Barth, *The Global Positioning System and Inertial Navigation*. New York, USA: McGraw-Hill, 1998.

[13] R. Azuma, B. Hoff, H. Neely, and R. Sarfaty, "A motion-stabilized outdoor augmented reality system," in *Proceedings of IEEE Virtual Reality '99*, pp. 252–259, March 1999.

[14] A. J. Hanson, *Visualizing quaternions*. San Francisco, California, USA: Morgan-Kaufmann/Elsevier, 2006.

[15] J. Vaganay, M. J. Aldon, and A. Fournier, "Mobile robot attitude estimation by fusion of inertial data," in *Proceedings of the International Conference on Robotics and Automation*, pp. 277–282, May 1993.

[16] J. L. Marins, X. Yun, E. R. Bachmann, R. B. McGhee, and M. J. Zyda, "An extended Kalman filter for quaternion-based orientation estimation using MARG sensors," in *Proceedings of the 2001 IEEE/RSJ International Conference on Intelligent Robots and Systems*, 2001.

[17] S. J. Julier and J. K. Uhlmann, "A new extension of the Kalman filter to nonlinear systems," in *Proceedings of AeroSense: The 11th International Symposium on Aerospace/Defence Sensing, Simulation and Control*, 1997.

[18] J. A. Rios and E. White, "Fusion filter algorithm enhancements for a MEMS GPS/IMU," in *National Technical Meeting Proceedings*, 2002.

[19] S. Beeby, G. Ensell, M. Kraft, and N. White, *MEMS Mechanical Sensors*. Norwood, MA: Artech House Inc., 2004.

[20] Q. Ladetto, V. Gabalio, and B. Merminod, "Two different approaches for augmented GPS pedestrian navigation," in *International Symposium on Location Based Services for Cellular Users*, February 2001.

[21] E. R. Bachmann, X. Yun, D. Mckinney, R. B. McGhee, and M. J. Zyda, "Design and implementation of MARG sensors for 3-DOF orientation measurement of rigid bodies," in *Proceedings of the 2003 IEEE International Conference on Robotics and Automation*, September 2003.

[22] Spark Fun Electronics, "Home page," 2006. http://www.sparkfun.com.

[23] Analog Devices Inc., "Home page," 2006. http://www.analog.com.

[24] M. J. Caruso, T. Bratland, C. H. Smith, and R. Schneider, "A new perspective on magnetic field sensing," in *Sensors Expo Proceedings*, pp. 195–213, October 1998.

[25] B. C. Baker, "Circuit layout techniques and tips," tech. rep., Microchip Technology Inc., 2003. http://www.analogzone.com.

[26] H. Zumbahlen, "Using the analog devices active filter design tool," Tech. Rep. AN-649, Analog Devices, Norwood, MA, USA, 2005.

[27] Microchip Technology Inc., *MCP6S28 Data Sheet*, March 2003. http://www.microchip.com/downloads/en/DeviceDoc/21117a.pdf.

[28] Texas Instruments, *ADS8325 Data Sheet*, November 2005. http://www-s.ti.com/sc/ds/ads8325.pdf.

[29] W. Kester, "Which ADC architecture is right for your application," Tech. Rep. Analog Dialogue 39-06, Analog Devices, Norwood, MA, USA, June 2005.

[30] B. Bronk, "Set/Reset pulse circuits for magnetic sensors," Tech. Rep. AN-201, Honeywell Inc., 2002.

[31] Honeywell Inc., USA, *HMC2003 Data Sheet*, June 2003. http://www.ssec.honeywell.com/magnetic/datasheets/hmc2003.pdf.

[32] M. P. Hayes, *Unpublished KiwiSAS-IV Manual*. Acoustic Research Group, Department of Electrical and Computer Engineering, University of Canterbury, August 2006.

[33] A. Persson, "The Coriolis effect — a conflict between common sense and mathematics," *Italian Meteorological Society*, pp. 20–31, 2005.

[34] A. Kelly, *Introduction to Mobile Robots*. Carnegie Mellon University, 1996. http://www.frc.ri.cmu.edu.

[35] H. Moritz, "Geodetic reference system 1980," *Journal of Geodesy*, pp. 388–398, September 1984.

[36] R. E. Bracken, D. V. Smith, and P. J. Brown, "Calibrating a tensor magnetic gradiometer using spin data," Tech. Rep. Scientific Investigations 2005-5045, U.S. Department of the Interior, 2005.

[37] T. Stork, "Electronic compass design using KMZ51 and KMZ52," Tech. Rep. AN00022, Philips Semiconductors, March 2000.

[38] P. Graven and T. Kenny, "Laboratory (and on-orbit) magnetometer calibration without coil facilities or orientation information," in *Proceedings of the Tenth Annual AIAA/USU Small Satellite Conference*, September 1996.

[39] J. L. Crassidis and K. L. Lai, "Real-time attitude-independent three-axis magnetometer calibration," in *Flight Mechanics Symposium*, p. 5, October 2003.

[40] National Geophysical Data Center, "Home page," November 2006. http://www.ngdc.noaa.gov/.

[41] G. T. Haupt, N. J. Kasdin, G. M. Keiser, and B. W. Parkinson, "An optimal recursive iterative algorithm for discrete nonlinear least-squares estimation," *Journal of Guidance, Control, and Dynamics*, May-June 1996.

[42] D. Gebre-Egziabher, G. H. Elkaim, J. D. Powerll, and B. W. Parkinson, "A non-linear two-step estimation algorithm for calibration solid-state strapdown magnetometers," in *Eighth Internation St.Petersburg Conference on Navigation System*, (St.Petersburg, Russia), May 2001.

[43] S. H. Stovall, "Basic inertial navigation," Tech. Rep. NAWCWPNS TM 8128, Naval-Air Warfare Center/Weapons Division, September 1997.

[44] D. Gebre-Egziabher, *Design and Performance Analysis of a Low-cost Aided Dead Reckoning Navigator*. PhD thesis, Department of Aeronautics and Astronautics, Stanford University, USA, February 2004.

[45] A. Kim and M. F. Golnaraghi, "A quaternion-based orientation estimation algorithm using an inertial measurement unit," in *Proceedings of the IEEE Position Location and Navigation Symposium*, pp. 26–29, April 2004.

[46] B. R. Madhukar, R. A. Nayak, J. K. Ray, and M. R. Shenoy, "GPS-DR integration using low cost sensors," in *Proceedings of ION GPS-99*, pp. 537–544, September 1999.

[47] M. J. Yu and S. W. Lee, "A robust extended filter design for SDINS in-flight alignment," *International Journal of Control, Automation, and Systems*, pp. 520–526, December 2003.

[48] E. H. Shin and N. El-Sheimy, "An unscented Kalman filter for in-motion alignment of low-cost IMUs," in *Proceedings of the IEEE Frames Conference*, pp. 273–279, April 2004.

[49] P. S. Maybeck, *Stochastic Models, Estimation, and Control*. New York: Academic Press, Inc., 1982.

[50] A. Kim, Y. K. Peng, and M. F. Golnaraghi, "A sensor fusion algorithm for GPS, strapdown and gyro-free inertial navigation systems," in *Proceedings of the CSME Forum 2004*, June 2004.